ABSTRACT

Title of Document: EXPERIMENTAL STUDY OF BEAM HALO IN INTENSE CHARGED PARTICLE BEAMS.

Hao Zhang, Ph.D., 2014

Directed By: Professor Rami Kishek, IREAP
Professor Patrick O'Shea, Department of ECE

Beam halo is a common phenomenon that occurs in most intense particle accelerators, and refers to collections of particles that stray far away from a well-defined central beam core. Often in high-intensity beams, the space charge force induces halo. Even for low intensity accelerators, the beam halo could occur in the injection section before the particles are accelerated to relativistic speed. The most severe effects from beam halo are emittance growth and beam loss. Emittance growth can cause the degradation of beam quality, and beam losses will impose restrictions on the beam current. Although one can use a larger aperture to compensate this, the overall cost will increase exponentially. In this dissertation, we address the halo phenomenon and formation mechanism in intense charged particle beams. Although most of the experiment and simulation study of halo is based on the University of Maryland Electron Ring, it is applicable to a wide range of accelerators in the same intensity regime.

We first discuss a matching procedure and rotation correction for the beam envelope. The gradients of four quadruples in the injection are independently adjust to match or mismatch the beam. The gradients of two skew quadruples in the injection are independently adjusted to correct the beam rotation. We succeed in matching the UMER beams and find out that the envelope mismatch and beam skewness are the major sources for halo formation in UMER. Halo could be drive out even in very early stage such as in 2 or 3 mismatch oscillations with large mismatch or beam rotation.

We simulate the halo formation in UMER lattice till about 10 mismatch oscillations with higher beam intensity in the frame of two envelope mismatch modes. In experiment, we generate envelope mismatch mode with different mismatch level (parameter) by adjusting the four quadrupoles in the injection. The agreement of the envelope between experiments and simulations is satisfactory for mismatch parameter in the range of 0.8-1.2. Emittance and beam width are obtained from tomography and adaptive optical masking and imaging method separately for comparisons with the simulation as well as the maximum emittance growth predicted by a free energy model and maximum particle radius predicted by a particle-core model. The experiments confirm the predictions from both the simulation and the theory with reasonable agreement.

We also further investigate the adaptive masking method for halo imaging, and apply it for halo diagnostics at JLAB FEL facility, and for imaging of the injected beam at the SLAC SPEAR3 storage ring.

EXPERIMENTAL STUDY OF BEAM HALO IN INTENSE CHARGED PARTICLE BEAMS.

By

Hao Zhang

Dissertation submitted to the Faculty of the Graduate School of the
University of Maryland, College Park, in partial fulfillment
of the requirements for the degree of
Doctor of Philosophy
2014

Advisory Committee:
Professor Rami Kishek, Chair
Professor Patrick O'Shea, Co-Chair
Professor Victor Granatstein
Professor Thomas Antonsen
Professor Adil Hassam, Dean's Representative

Dedication

献给深爱我的父母，张朗，唐复蓉。

永远缅怀我的外婆，李义碧老人。

To my beloved parents, Lang Zhang and Furong Tang.

In memory of my grandma, Yibi Li.

Acknowledgements

I am grateful for the years I have spend in University of Maryland. Along the process to obtain a degree, many people have inspired me with their wisdom, kindness, compassion and creativity. First and foremost is my advisor Professor Rami Kishek, who recruits me and lead me into the accelerator field. During these years, he has motivated me to challenge myself not only in the safe area which he was familiar with but also in the blind spot that we have to explore. I have been influenced deeply by his approach of presenting ideas and manner of thinking about problems, which will benefit for my whole life. I would like also thank my co-advisor Professor Patrick O'Shea, who also executes as Vice President in one of the top public university in the nation, but still shares time with me about the blueprint of my research during these years. His leadership and insight have encouraged me to accomplish this dissertation but also to bigger goal in the future. Dr. Ralph Fiorito served as my research advisor with the diagnostics project. His requirement of pursuing excellence, attitude of hard working and style of carefulness and rigorousness equipped me with full armor for my research. I can't forget the days we work together in an optical table until 3:00 am in the midnight, which would be one of my precious memories in my life.

I would like to cherish the memories of Professor Martin Reiser, who gave his book as gift to me and cared about my research in his last days. I would also thank Dr. Brian Beaudoin, Dr. Santiago Bernal, Dr. Dave Sutter, Dr. Timothy Koeth, Dr. Diktys Stratakis (BNL) and Dr. Chao Wu for their tremendous help in experimental setup, UMER ring maintenance and wonderful suggestions. I would like to thank Dr. Irving

Haber, Dr. David Grote (LBL), Dr. Jean-Luc Vay (LBL) and Dr. Steve Lund (LBL) for providing the Warp code and their wonderful discussion and suggestion on simulation. I would like to thank Dr. Anatoly Shkvarunets, Professor Carsten Welsch (University of Liverpool), Dr. Shukui Zhang (JLAB), Dr. Dave Douglas (JLAB), Dr. Steven Benson (JLAB), Dr. Jeff Corbett (SLAC), Dr. Kai Tian (SLAC), Dr. Alan Fisher (SLAC), Dr. Walter Mok (SLAC), and Dr. Toshiyuki Mitsuhashi (KEK) for their help in optics design, opening their facility and also their useful discussion for the DMD based experiments. Thanks also to Dr. Donald Feldman, Dr. Massimo Cornacchia, Dr. Karen Fiuza, former student Dr. Eric Montgomery, Dr. Jayakar Charles Tobin Thangaraj, Dr. Christos Papadopoulos and my colleagues Dr. Yichao Mo, Dr. Kamal Poor Rezaei, Dr. Blake Riddick, Dr. Zhigang Pan, Eric Voorhies, Will Stem, Kiersten Ruisard who contributed to this dissertation in many ways. Finally, I thank my friends in Grace Fellowship and Chinese Christian Church of Maryland for their spiritual supports and care during these years.

Table of Contents

List of Tables

List of Figures

Chapter 1: Introduction

1.1 General background of beam halo

Beam halo is a common phenomenon in particle beams [1, 2], especially for modern, advanced, accelerators where high beam intensities lead to strong space charge. Although there are many definition of beam halo [3 - 6], there is no well-accepted, rigorous one. The halo is generally understood as a population of particles reaching large transverse radii relative to a more intense, centralized portion of the beam, which is called the “core”. To reach these larger radii, halo particles must possess higher energies than other particles. Hence, a significant fraction of well-formed halos includes particles that are initially in the core, but will be pushed to large radii at a later time because of their higher transverse velocities. Beam halo is associated with emittance growth and thus decrease the beam quality. Here, the term emittance is a common characteristic of beam quality, which is proportional to the phase space volume but dynamically depends on the detailed knowledge of phase space [7]. A serious practical implication of halo is that halo particles travelling far from the center of the beam can hit the beam pipe, producing a number of undesirable effects in addition to the beam loss [8, 9]. For a high energy particle beam, the lost particles contribute to the nuclear activation of the wall material, increasing the radiation background and possibly causing damage to beam line components. Especially for positively charged beams, the lost halo particles can cause secondary electron emission, or knock off desorbed neutrals that then get ionized, contributing to an electron cloud that complicates the beam dynamics [10, 11].

Halo mitigation is difficult. Although larger beam pipes can be used to accommodate halos, the cost of the required larger magnets, radio frequency cavities, etc., can be significant. Moreover, since most halo are actually inside the core with larger velocities, simple particle scrapers that remove particles beyond a certain radius are ineffective unless used in combinations, with phase-space rotations in between [12]. Understanding the causes of halos is crucial, therefore, to guide efforts to eliminate them or mitigate their negative effects.

1.2 Previous theoretical and simulation study of beam halo

A number of theories have been developed, backed by simulations, to describe the formation mechanism of beam halo [13-15]. These studies have shown that there are many factors which can cause halo [16], e.g. intra-beam scattering, collective instabilities, misalignments, magnet errors, noise and resonances associated with both intrinsic incoherent processes and space charge forces. The most successful model in illustrating halo formation is the particle-core model [13, 14], which describes the halo as a parametric resonance between single-particle oscillations, and the collective oscillations of a mismatched core. Under the assumption of a round continuous beam with a uniform spatial density propagating in a uniform beam transport system with azimuthal symmetry and a linear radial focusing force, they describe the beam envelope in Eqn. 1.1(also see it in [7]),

$$\frac{d^2R}{ds^2} + k_0^{\,2}R - \frac{\varepsilon^2}{R^3} - \frac{K}{R} = 0 \qquad (1.1)$$

where R is twice the rms beam radius, k_o is the wavenumber corresponding to the uniform external focusing force, ε is the RMS emittance, and K the generalized

perveance. All these parameters are well defined in Reiser's book [7]. To be emphasized here, $k_0{}^2R$ represents the external focusing force, ε^2/R^3 is a force related to the beam emittance, and K/R is the space charge force. For a perfectly matched beam, these three forces should be balanced, meaning

$$k_0{}^2R = \frac{\varepsilon^2}{R^3} + \frac{K}{R} \tag{1.4}$$

When these forces are not balanced, the beam envelope will be mismatched, as the pink curve shown in Fig. 1.1.

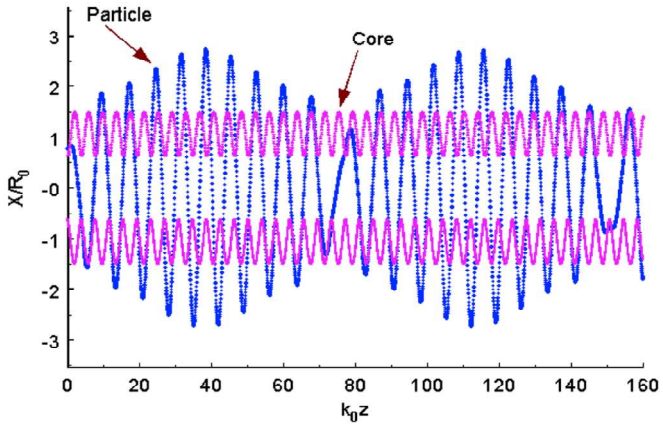

Figure 1.1: Beam envelope oscillations and the trajectory of a single test particle in a mismatched beam.

Even though the space charge force is linear inside a uniform beam, it is nonlinear outside. Thus, a single particle that ventures just outside the edge of the beam will experience this nonlinear force. Furthermore, the single-particle oscillation frequency is modified by the space charge force, and is different for particles wholly contained within the core from that of particles oscillating outside it. It is thus possible for a single particle oscillation to resonate with the core mismatch oscillations and be driven to large

amplitude, as shown by Gluckstern in Ref. [13]. Using particle-core model, Wangler in Ref. [14] showed that there is maximum amplitude of particles in a mismatch beam that depends on the magnitude of the mismatch parameter, which give us a rough idea of beam loss from the halo formation.

Another consequence from beam mismatch is emittance growth, which can be related to the free energy model developed by Reiser [17]. It can predict the conversion of beam free energy from mismatch oscillations into the thermal energy of the beam based on the mismatch strength as well as the tune depression ratio of the beam.

Other researchers have further developed the particle-core model. Qiang [18] extended it to a 3D mismatched anisotropic beam, and Ikegami [19] studied it in a periodic focusing channel. Kishek [15] found that halo can also arise from skew mismatches, i.e. caused by quadrupole rotation errors. The linear coupling between the two transverse directions leads to additional mismatch modes that can resonate with single-particle trajectories.

More recently, Papadopoulos [12] studied the removal methods for beam halo. He found that, even for a hypothetical, ideal, collimator that removes all the halo particles in phase space, the halo can regenerate if the mismatch oscillations that led to the halo are still present. This implies that, it is necessary to have a detailed theoretical understanding of the halo formation mechanism, supported by experimental testing and simulation, rather than a reliance on collimators for halo removal.

1.3 Previous experimental study of beam halo

There have been few experiments dedicated to the systematic study of halo. Most accelerators lack the flexibility to adjust the beam intensity over a wide enough range the effects from space charge, or suitable diagnostics to detect the beam halos. The halo measurement of LEDA (Low Energy Demonstration Accelerator) in Los Alamos National Laboratory (Fig. 1.2) is an exception [8]. The novel transverse beam-profile scanners [20] are used to detect both the beam core and halo profiles over a high dynamic range. A proton beam is injected at 6.7 MeV, peak current of 75 mA and a 1 Hz repetition rate, with a 30 μs pulse length. The beam was matched by adjusting the first four quadrupoles such that the RMS beam sizes are unchanged in the last eight scanner locations. The mismatch parameter μ, defined as the ratio of the RMS size of the initial beam to that of the matched beam is varied by adjusting the first four quadrupoles. The profile and maximum extent of the resulting halo, as well as the growth of the RMS emittance was measured as a function of the mismatch parameter. The results indicated good agreement with predictions from the free energy and the particle-core models.

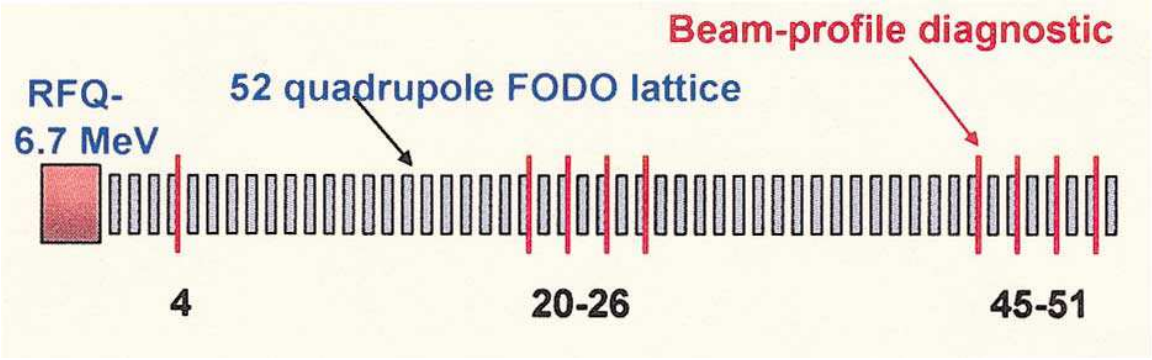

Figure 1.2: Schematic of the beam-halo measurement setup in LEDA [8]

These experiments at LEDA were limited to only about ten mismatch oscillations, and thus examined only the early stage of the mismatch oscillations. Moreover, the tune

depression ratio of the beam is about 0.82-0.95, which is still in the emittance dominated region. Additionally, the LEDA experiments suffered from an initial halo, which complicated the analysis of the results. The LEDA machine has since been dismantled, so continuing those studies requires the use of a different facility.

Similar experiment was carried out recently [21] in IHEP for code validation as well as helping design the Accelerator Driven Subcritical System in China. A Proton beam was injection from a 3.5 MeV radio frequency quadrupole (RFQ) into 28-quadrupole FODO transport channel. They succeed in beam match in x axis and the simulations are fairly successful in reproducing the rms properties of the measured matched beam profile in horizontal projections. Due to lack of beam profile diagnostics in y axis, there are some discrepancies between experiment and simulation for mismatched cases.

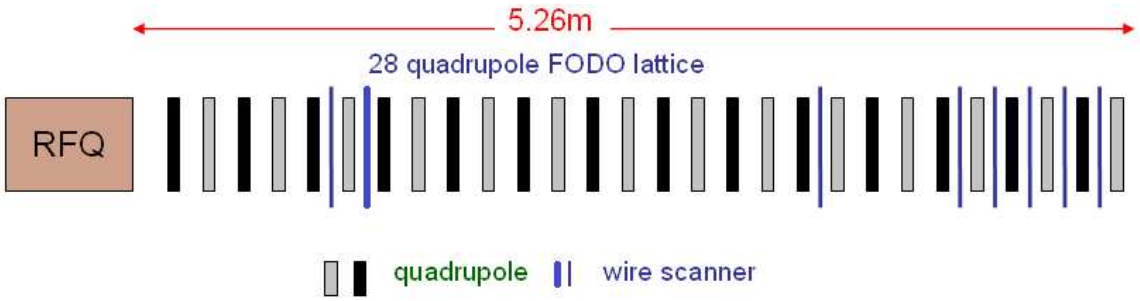

Figure 1.3: Block diagram of the beam-core matching experiment transport line in IHEP

In halo formation study, proton beams are used for most of the experiments. The disadvantage using proton beam as tools for halo study is that the diagnostic are very limited due to the destructive energy of the proton beam. The wire scanner, one of diagnostic used in both cases introduced above, has a reasonable dynamic range but only give us a beam profile in one direction. The tune depression ratio of the beams in University of Maryland electron ring (UMER)[22] is similar to that of most proton beam

accelerator nowadays. Since UMER use low energy electrons, which is not so destructive for most diagnostics, it is an advantage to study the beam halo. This dissertation will focus on the UMER machine and discuss the halo formation phenomenon with simulation and experimental results. A novel diagnostic method to measure halo developed in my master thesis will be further discussed and used for the halo experiment in UMER as well as other experiments in major US national labs.

1.4 Organization of this dissertation

I start in Chapter 2 to introduce the experimental setup in UMER, various diagnostic system and methods, and simulation tools. In Chapter 3, I discuss the procedure for beam match and then perform beam envelope match for three beams with increasing beam currents. In Chapter 4, I discuss two major sources, transverse envelope mismatch and rotational error for halo formation. The latter one is first testified in experiment comparing with the discovery in simulation a couple of years ago. In Chapter 5, the discussion is in frame of mismatch modes. The halo formation is systematically studied with mismatch parameters in two envelope mismatch modes. Experiment results of maximum particles radius and emittance growth for different mismatch strengths are compared with simulation and theory and show a strong support of these theories which can be applied for future design of high intensity and high current accelerators. In Chapter 6, I talked about two side projects of halo related measurement by using the novel adaptive masking method in JLab FEL facility and in SLAC SPEAR3.

Chapter 2: Experimental Setup and Simulation Tools

2.1 Introduction of UMER

UMER is small compact electron storage ring with a low energy (10 keV) but relatively high beam current (~1-100 mA). It is designed to study the physics of electron beams from emittance to space charge dominated ones which can be scaled to higher beam energy with higher mass. Fig. 2.1 shows a schematic of the UMER layout, and Table 2.1 lists its key parameters.

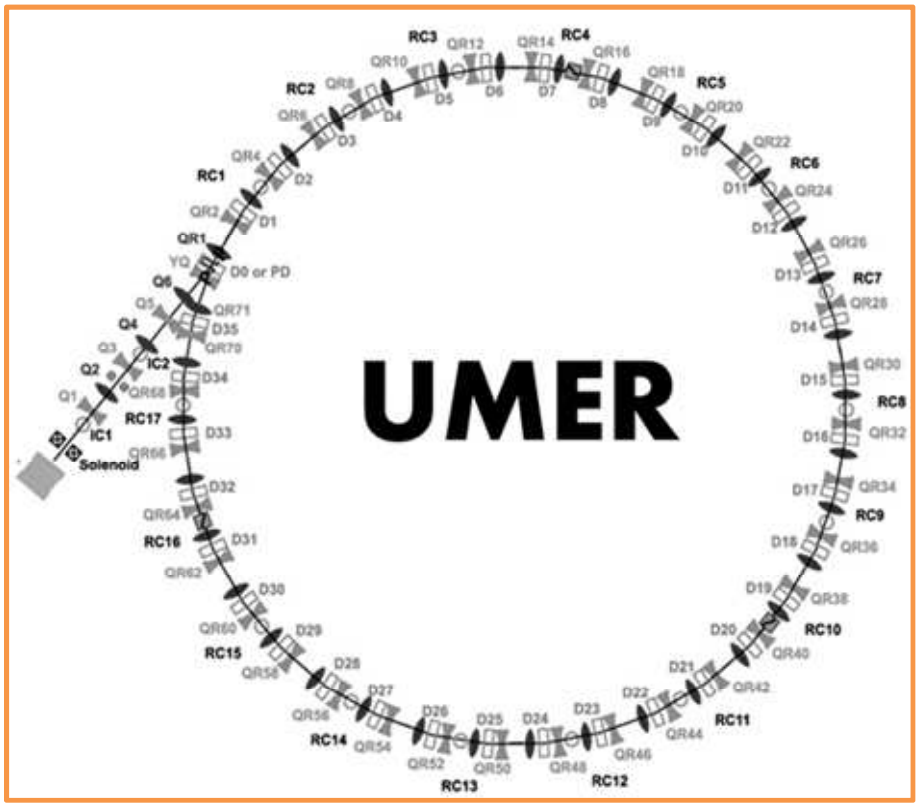

Figure 2.1: Schematic layout of UMER.

Table 2.1: UMER design parameters [23]

Beam Energy	10 keV
$\beta = v / c$	0.2
Pulse Length	20-120 ns
Current	0.5-100 mA
Ring Circumference	11.52 m
Lap Time	197 ns
Pulse Repetition Rate	10-60 Hz
FODO Period	0.32 m
Zero-current Phase Advance	0.760

A key feature of UMER is the ability to vary the beam intensity. The related intensity parameter χ, the ratio between space charge force and external focusing force, ranged from 0 (emittance dominant) to 1 (space charge dominant), can be varied to generate beams which are dominated by the beam emittance to where intense space charge dominates the dynamics. The beam intensity is varied by using different apertures to change the beam current. A mechanically rotatable wheel with a number of apertures is located right after the electron gun exit to do this. The variable beam intensity allows us to study different halo formation mechanisms, including magnet alignment, mismatch, resonance, space charge and so on. Table 2.2 shows a list of aperture size, current, emittance and intensity parameter.

Table 2.2: Parameters of UMER beams [22]

Aperture#	r_0 (mm)	I (mA)	ε (μm)	χ
1	0.25	0.6	7.6	0.275
2	0.875	6	25.5	0.605
3	1.5	21	30.0	0.901
4	2.85	78	86.6	0.968
5	3.2	104	97.3	0.978

The advantages to conduct a halo experiment in UMER are: 1) the beam is only 10 keV, which means nothing to worry about the radiation. 2) the schedule is flexible since it's a university based machine; 3) the intensity parameter could be easily varied to access the halo dynamics in a wide region; 4) as a ring, the duration time of a single pulse is not limited, and a recent success shows UMER can propagate the beam more than 1000 turns which is 11 km [24]; 5) UMER is a pure research machine, so any new diagnostic can be simply implemented.

2.2 Basic Diagnostics in UMER

In UMER, I use imaging method to detect the transverse distribution of the beam. The image source at UMER is a 31.75 mm diameter glass screen, coated with P-43 phosphor (Gd_2O_2S:Tb, with 1.6 μs response time) or fast phosphor (ZnO:Ga, with <3ns response time), which is located in each of the diagnostics chamber as shown in Fig. 2.2.

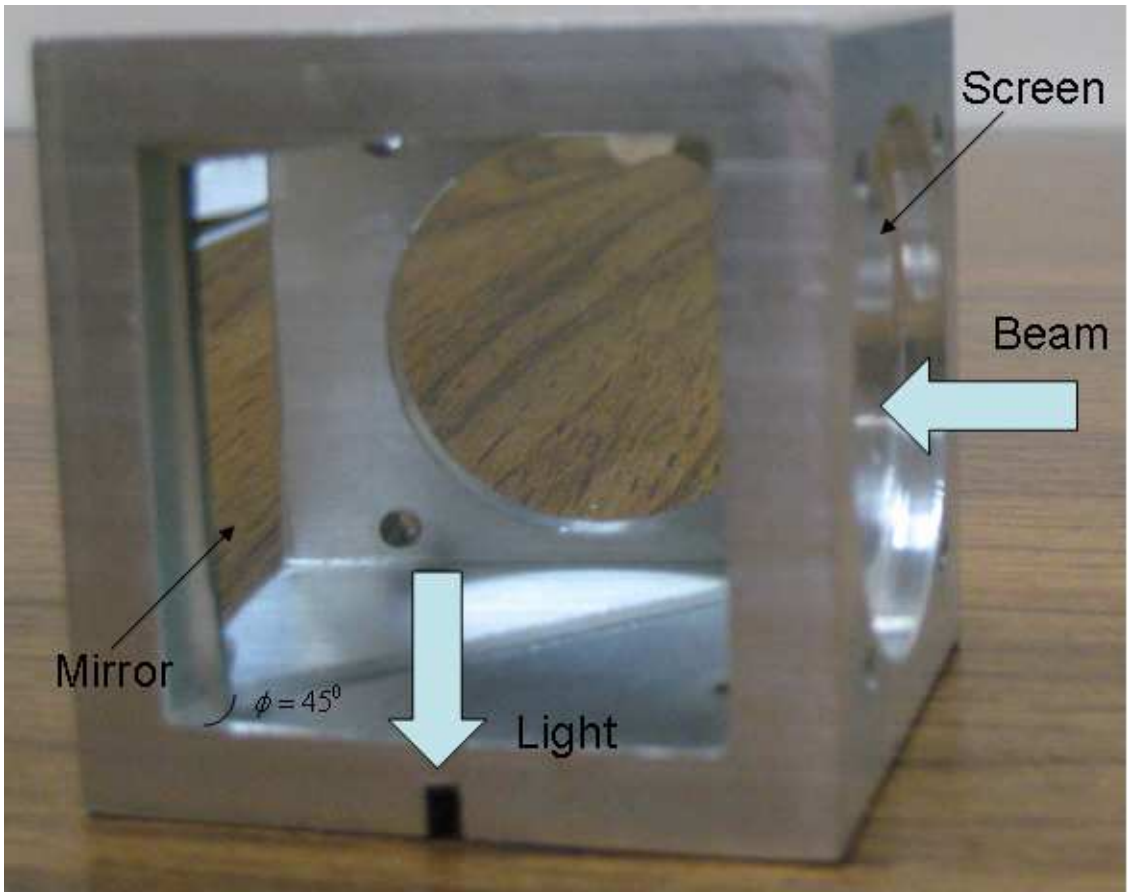

Figure 2.2: Screen assembly in UMER.

Each chamber contains two diagnostics including the screen in the bottom and the button-type BPM in the top. These two diagnostic are interchangeable by a non-magnetic actuator shown in Fig. 2.3. Notice that the BPM is non-intercepted while the screen is not. The slider, which sets on the rail vertically and holds the flange by its horizontal clamp, is powered by high pressure gas instead of the original motor to avoid any magnetic field from the motor. There is a switch by the side to lift the screen up for taking images. The phosphor screen is oriented at 90 degrees with respect to the beam direction. The fluorescent light is directed out of a vacuum system by a front surfaced mirror at 45° angle, and come out from the window.

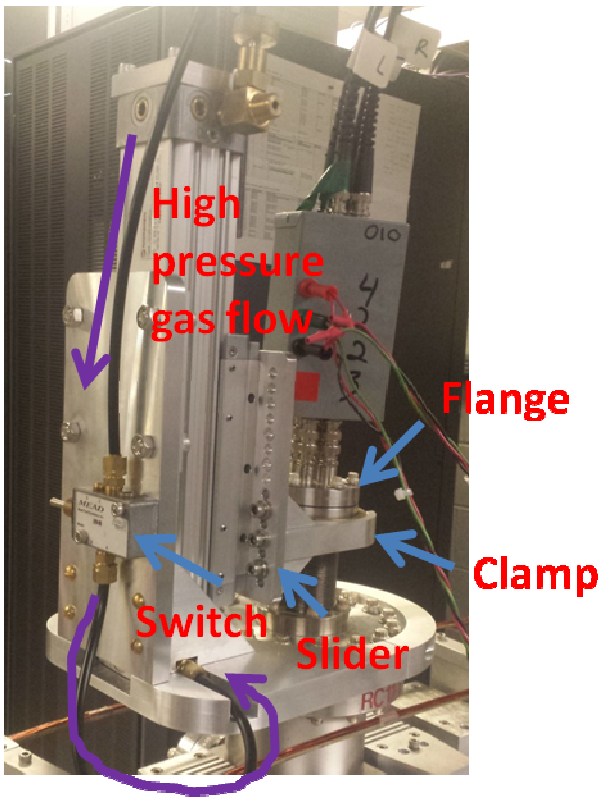

Figure 2.3: Illustration of air pressed actuator.

2.3 Imaging System

In order to control the image taken process for tomography and empirical matching, I designed an imaging system based on Ethernet cameras [25] (GigE Vision Flea3 camera manufactured by Point Gray Research). The camera, which features 12 bit, variable gain and shutter time, and CCD with 768 × 468 pixels, is directly used to image the beam with a build-in 16mm macro lens.

The illustration of the system is shown in Fig. 2.4. The cameras are connected to camera control PC through a gigabyte switcher. The camera control PC can control all the magnets power supply though the main control PC by sending a command line.

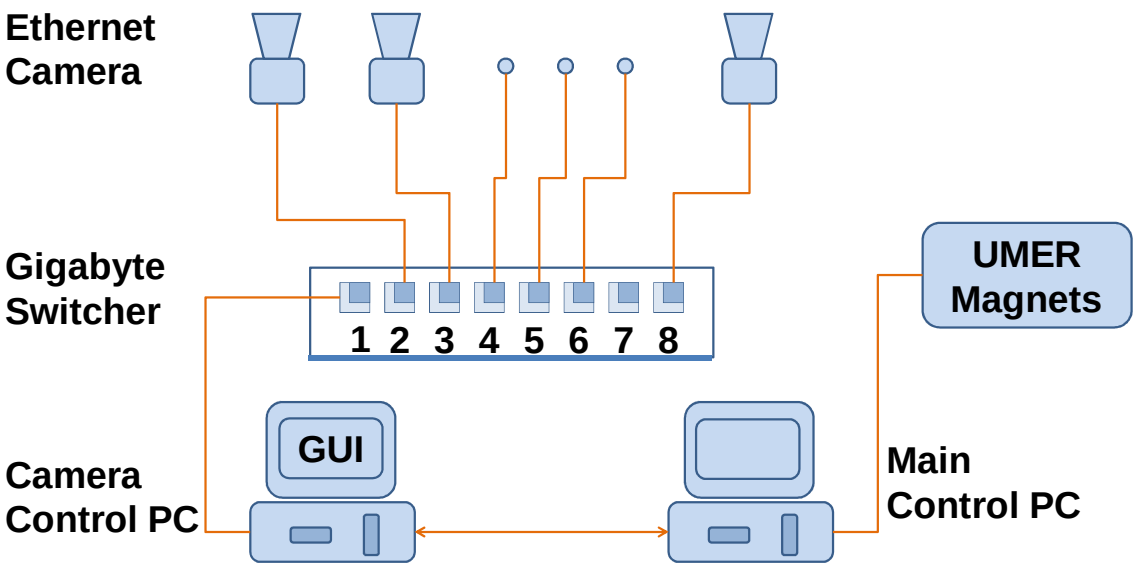

Figure 2.4: Illustration of Imaging System.

The whole system is integrated by a self-wrote Matlab GUI code. The interface of the GUI is shown in Fig. 2.5. It includes a camera control panel, Magnet control panel, image display and calculation panel, and the emittance panel.

In the camera control panel, Camera Select is used to specify which camera to use. Trigger control specifies whether one runs the camera at trigger mode or shutter mode, and which trigger mode one uses (the trigger mode can be referred to the camera manual). Gain and Shutter specifies the camera electronical gain and shutter time, which is to be set appropriately to prevent the saturation of the CCD and obtain enough beam signal from phosphor screen. One can also simply acquire one image by clicking Acquire button or runs the camera in continuous focusing mode by enabling the Focus button. The image obtained will be shown immediately in the display panel. The SaveAs button is used to save an image.

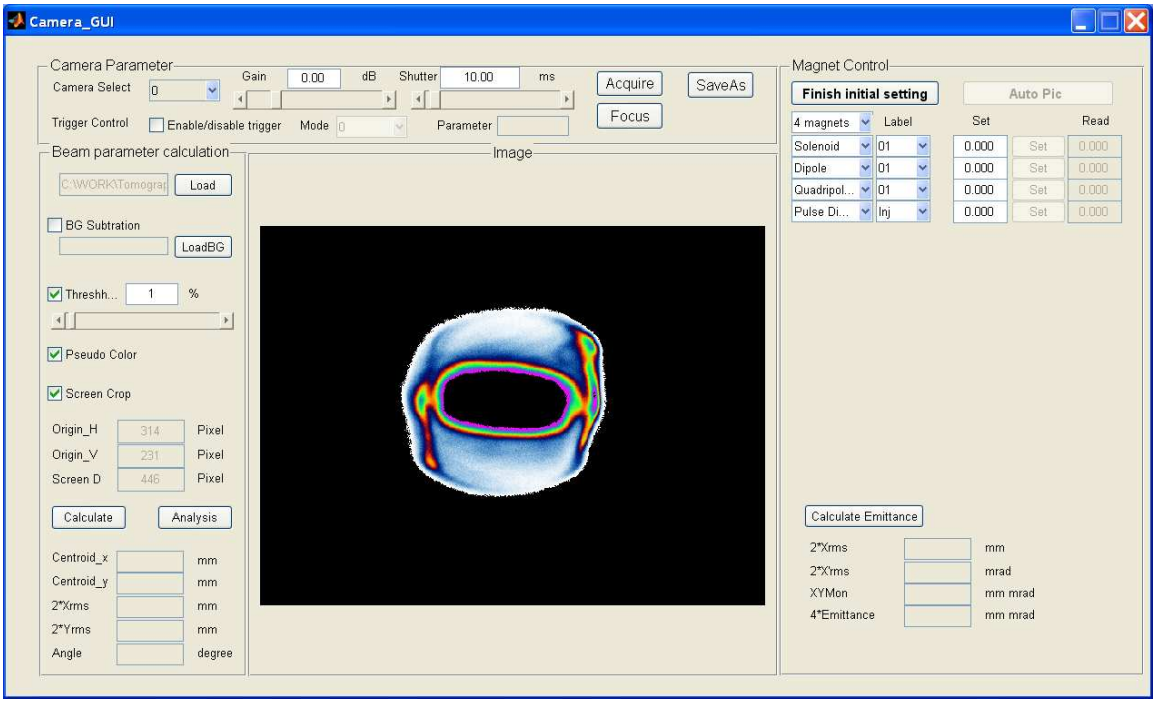

Figure 2.5: Imaging system GUI

The image display and calculation panel is used to control the image display modification such as background subtraction, threshold subtraction, pseudo color and screen crop. Each of these corresponds to a checkbox in the panel. The Screen Crop checkbox is to remove the background outside the round screen illuminated by scattering. In the image, the screen is defined by a circle from calibration, the origin and diameter of which are filled in the edit box manually. The Calculate button calculates the beam centroid, beam size and rotation angle based on the previous modification while the Analysis button is used to do a series of such calculation of similar images. Here, similar means the group of images share the same calibration of the screen location.

The Magnet control panel is used to communicate with the main control computer. One can specify the number and the type of the magnet to be used in one experiment. The type of magnets includes solenoid, regular and skew quadrupole, horizontal and vertical

dipole as well as the pulsed magnets. The current of the power supply for each magnet can be set manually by typing a number in the set box and clicking set button. Alternatively, one can do a currents auto scan by clicking the AutoPic button. In the auto mode, a currents scan file will be required and an image acquiring and saving will be initiated after each set of changes of the magnets currents.

The emittance panel is used for 2D phase space image generated by tomography. It will calculate the beam size, beam divergence, the coupled moments of the two, and the emittance.

In this dissertation, without special notification, the system describe above is the default imaging system.

2.4 Phase space tomography

Similar to the computerized tomography used in medical and industrial applications, a method developed previous in UMER [26, 27] to reconstruct the phase space of the beam though the projections of the 4D beam into the configuration space with different angles as shown in Fig. 2.6. Three or four quadrupoles are used to produce these angles to cover a whole 180 degree range, so that any noise artifact is minimized. The reconstruction process is written in code using MATLAB, detail of which can be referred to [26, 27]. One can calculate the RMS emittance though the reconstructed phase space image and the error is usually below 7% [27].

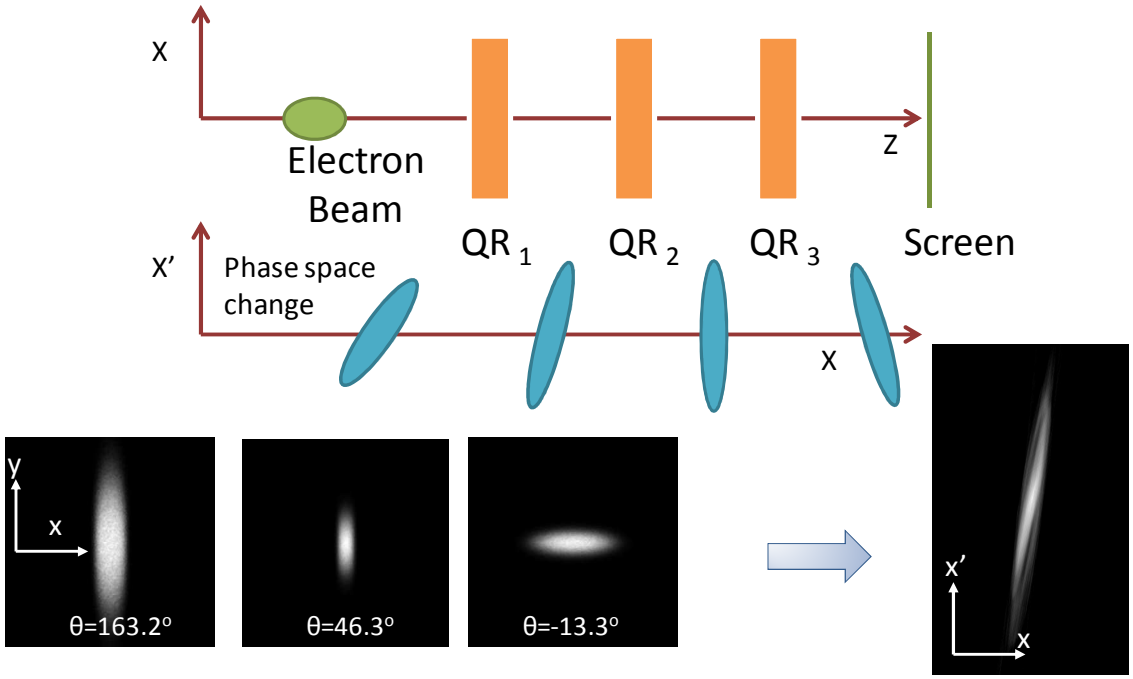

Figure 2.6: illustration of the tomography method to reconstruct the phase space: top shows the diagram of the configuration; middle shows the corresponded phase space change of beam; bottom shows beams in different quadrupoles settings and the reconstructed beam picture in x-x' space

2.5 Adaptive optical mask method for halo measurement

In accelerator related diagnostic, it requires a high dynamic range measurement for beam profile. In my master's thesis [28], I have developed a novel imaging diagnostic using adaptive masking method to measure beam halo with very high dynamic range based on the digital micro-array device (DMD). Based on the properties of DMD, my colleagues and I have designed a flexible imaging system which is easy to employ and apply to image the beam halo in most of the accelerators [29-33]. The essential features of the design are schematically shown in Fig. 2.7.

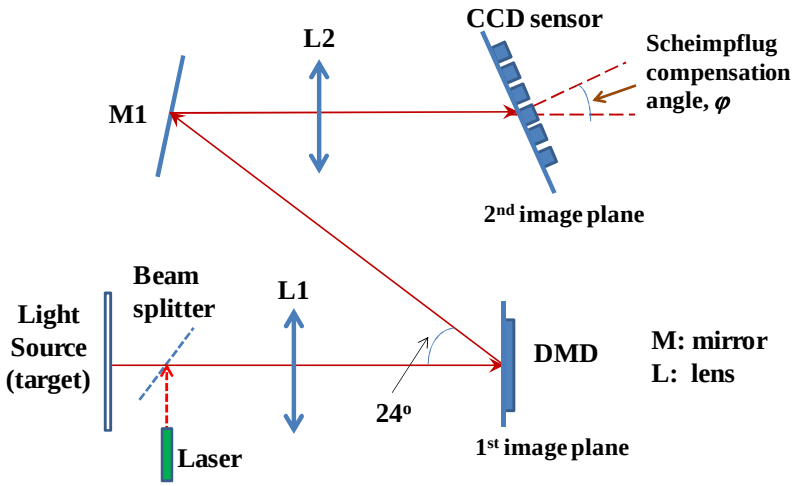

Figure 2.7: Schematic of halo imaging optics using DMD.

The setup shown in Fig. 2.7 can be considered as two optical channels: 1) the source, lens L1 and the DMD surface, which is oriented perpendicular to the optical axis and is the first image plane; and 2) the tilted DMD image plane, considered as a new source, lens L2 and the CCD sensor, which is the second image plane. Note that the DMD in the first channel is perpendicular to the optical axis. This allows us to easily align the entire system will the help of a laser. The DMD is mounted on a combination rotation and 2 axis mirrors mount to facilitate the alignment.

Mirror M1 further facilitates the alignment of the second channel. Two rotational compensations [33] are required to use this system to image the source: 1) the DMD must be rotated about the optical axis; 2) the camera sensor must be rotated in the horizontal plane by 24 degree.

2.5.1 DMD Diffraction Effects

The DMD behaves like a 2D optical grating. If illuminated by a single wavelength laser source, a cross like diffraction pattern similar to that of a rectangular mesh will be

observed. In addition when all the micro-mirrors are rotated by +12° the DMD becomes a blazed grating with the central order reflected in the direction +24° in the horizontal plane with respect to the incident laser beam. When the DMD is rotated by 45° the diffraction pattern also correspondingly rotates. The resulting pattern is shown in Fig. 2.8 (a). Note that the central order has been suppressed so as not to saturate the imager. When a uniform source of *white light* illuminates this "blazed" grating, the light is further dispersed in the horizontal plane producing the Fraunhofer pattern shown in Fig. 2.8 (b). These pictures were obtained by imaging the light diffracted by from the DMD (all pixels 'on') in the focal plane of a 200 mm focal length lens.

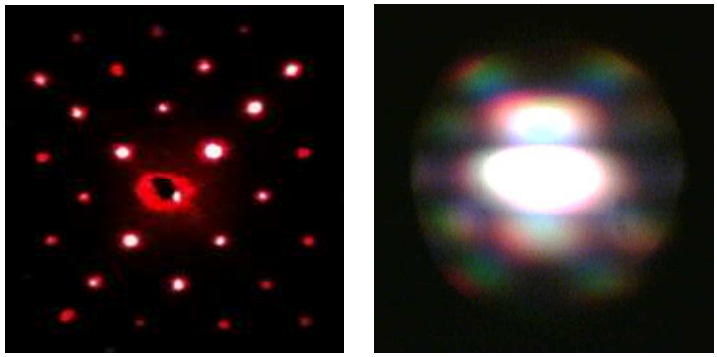

(a) (b)

Figure 2.8: (a) Single wavelength diffraction pattern; and (b) white light diffraction pattern, both formed from a 45^0 rotated DMD with all pixels set at $+12^0$.

Note that for the white light diffraction pattern all the orders are smeared in the horizontal plane. This is due to the effect of both wavelength dispersion and overlapping of the light from the central spot and nearby first order diffraction spots. The latter effect is particularly evident in the central and first orders. The picture further makes it clear that most of the light reflected by the DMD is contained in these two orders.

If the incident light on any grating is non-uniform but has a known distribution, i.e. is an 'object', any order of the light diffracted by the grating can be used to image the

'object'. Any aperture in the optics will filter out higher order diffraction spots which ultimately will reduce the imaging resolution so this must be checked for a given application. However, if the numerical aperture of the second channel optics is sufficient to accept the central two orders, most of the light diffracted by the DMD will be relayed into the second channel. This is indeed the case for our optics. We have traced the rays corresponding to the angles of the central and first order diffraction spots with an optics code to insure that there is no vignetting of these rays through the optics of channel two.

2.5.2 Spatial Resolution

There are several standard methods to measure the spatial resolution of an optical system. We measured the spatial resolution of our optical system by imaging a "knife edge" resolution target. This was constructed from a rectangular piece of, black anodized aluminum foil (Cinefoil) mounted on a white card, onto the DMD. The card is backlit with an adjustable intensity 'white light' source (i.e. an incandescent lamp). In these bench tests we make use of a PIMAX2 camera with a 1024×1024 pixels CCD array. Each pixel of the CCD sensor is $13\ \mu m \times 13\ \mu m$.

To insure that the DMD plane is in good focus on the camera to begin with, we program the DMD to accept a well known test image, i.e. a black and white checkerboard, which is included in the software supplied by the manufacturer to control the DMD. This pattern is ideal for adjusting the focus of the second channel since it originates with a few microns of the surface plane of the DMD chip and has multiple sharp black-white boundaries, i.e. the checkers. Once this source is focused onto the CCD, we turn all pixels to the 'on' state to reflect the resolution target image from the first channel into the

camera light path. We then adjust the focus of the first lens system L1 and L2 to produce the best focus of the resolution target on the camera, without moving lenses L3 or L4. Figure 2.9 shows two views of the resolution target; the left hand side is a full view of the entire target, the right hand side a magnified view of the corner of the black rectangle portion of the target.

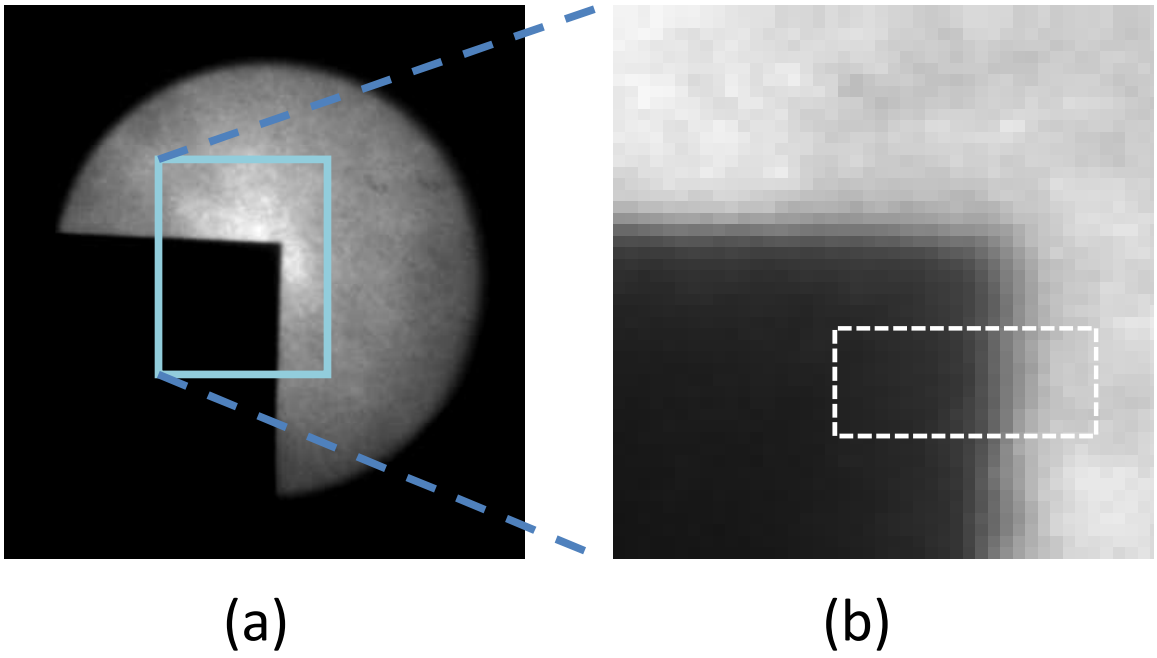

Figure 2.9: (a) Resolution target; left: full view, right: (b) Expanded (× 16) view.

Vertical and horizontal line scans of the corner of the black corner of the target at the pixel level show an 'S' shaped dispersion curve. Figure 2.10 shows a horizontal scan which is averaged over 4 vertical pixels (see the white box shown in Fig. 2.9(b)). To analyze the resolution of the image we assume that the point spread function can be represented by a 2D Gaussian and convolve this function with the source intensity distribution $A(x,y)$. An line scan across the image, e.g. $I(x)$, the brightness along the linear

scan (X direction) normal to the sharp linear boundary (Y direction, at $Y = 0$) is described by the convolution integral:

$$I(x) \propto \iint A(x', y') \exp\left(-\frac{(x - x')^2}{2\sigma_x^{\,2}} - \frac{y'^2}{2\sigma_y^{\,2}} \right) dx'dy' \tag{2.1}$$

where we assume A(x,y) = const. at $X > 0$ and $A(x,y) = 0$ at $X < 0$. A similar expression can be derived for a Y scan. One can easily show that the resulting intensity scans are error functions. Simple fits of the experimental horizontal and vertical scan data to the corresponding error functions and their respective Gaussians functions, which are the derivatives of these functions, are shown in Fig. 2.10 (b). The widths of the horizontal and vertical Gaussians are 3.0 and 2.1 respectively. The width provides as estimate of the resolution of the entire optical system.

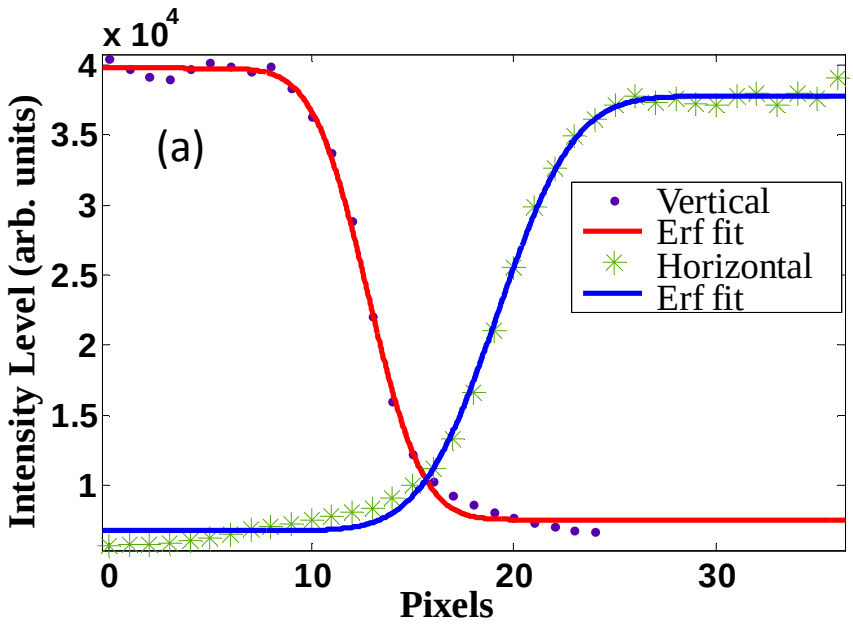

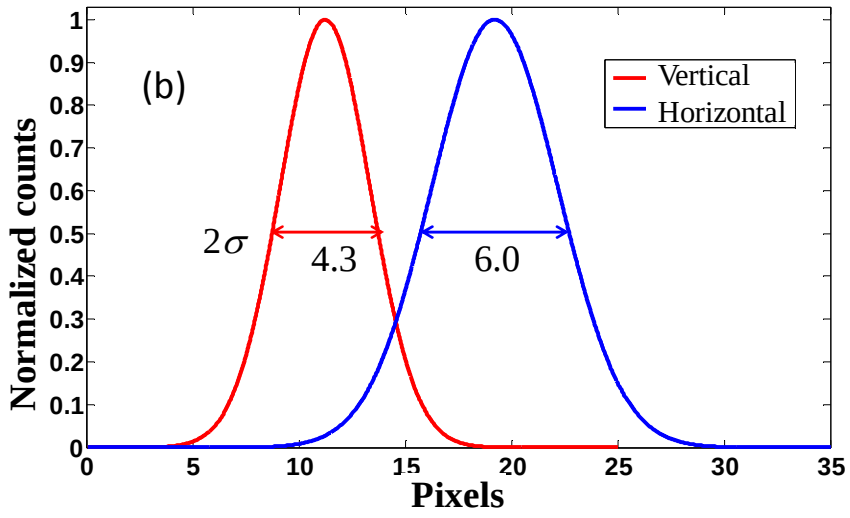

Figure 2.10: (a) Horizontal and vertical scan of resolution target corner shown above in Fig. 2.9 and (b) Related Gaussian functions.

We compare these measured values of the resolution of the DMD optical system, to that of a 'standard' optical system in which the DMD is replaced by a simple mirror. The major difference in the optics when the mirror is used is that Scheimpflug compensation is not required. So for the resolution test with the mirror we rotate the CCD camera back to its initial orientation, i.e. perpendicular to the optical axis of the second optical channel. We then observe the knife edge resolution target and follow same procedure described above to measure the resolution. The measured width of the black-white transition region in both the horizontal and vertical directions is σ ~3 pixels, which is approximately the same value measured for the DMD optical system. This indicates that the optical resolution of the DMD optics is essentially the same as that of the 'standard' mirror system.

2.5.3 Single Pixel Response

We have also measured the single pixel response of the second optical channel. To accomplish this, a uniform white light source beam is directed onto the entire DMD but with only a single micro-mirror activated. The light from this single illuminated pixel is imaged onto the CCD via lenses L3 and L4. Figure 2.11 shows the resulting image (shown as a negative) as well as horizontal and vertical line scans across the image. The scans show that the width of a Gaussian fit to distribution of intensity in both the horizontal and vertical directions is σ ~ 3 pixels, which, interestingly, is the same as the measured optical resolution of the entire optical system. This result means that the DMD does not significantly influence the resolution or PSF of the optics system. Furthermore, since the contribution to the PSF of the second channel is comparable to that of the overall system, the width of the PSF of the first channel must be less than that of the second channel or very close to it.

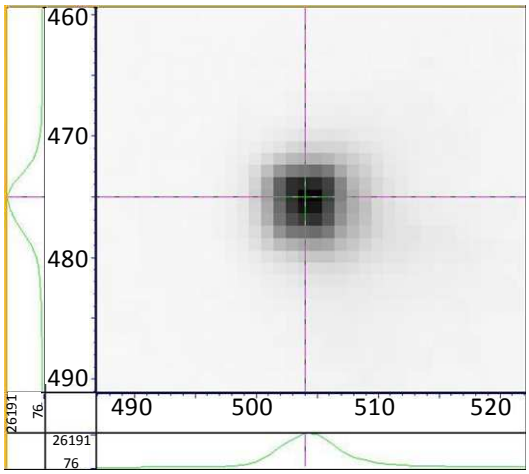

Figure 2.11: Response of a single DMD pixel to uniform white light illumination.

2.5.4 High Dynamic Range Measurement of the point spread function (PSF)

As far as dynamic range of the optical imaging system is concerned, it is only necessary to measure the PSF of the first channel. The reason for this is that the second optical channel merely reimages the first image from the DMD plane with or without a mask in place, with an inherently low dynamic range imaging system.

The optical masking technique we will describe below uses a series of images each of which are taken using a CCD camera with a (DR ~100-1000). Thus the wings of the PSF of second channel below 10^{-2} or 10^{-3} of the peak intensity of any masked or unmasked image of the beam are not visible to the CCD camera. In fact any contamination of the true beam halo due to the wings of the real PSF will be visible in the first channel and affect image on the DMD. This means that if the wings of the PSF exceed the beam halo in first image they will also exceed the beam halo in the distribution, which is reconstructed using the DMD masking method. Similarly, if the wings of PSF are below the true beam halo level, then this will be the case in the reconstructed image as well. Thus, for all intensive purposes it is sufficient to measure the PSF with high dynamic range for the first channel only. In order to do this, we use a wide band (white), 'point like' source with a homogeneous angular distribution, which closely mimics that of the phosphor screen used at UMER. A schematic of measurement system is shown in Fig. 2.12. The source is a white thread illuminated by light produced by a light-emitting diode (LED) that is 4 mm in diameter. The LED light is focused onto the thread by a Nikon camera lens which has focal length f = 28 mm and is oriented so that the normal input aperture of the lens faces the LED. The thread is a very good diffuser and scatters the focused LED light uniformly into a wide angle. We verified this

by imaging the angular distribution with a CCD camera placed in the Fourier plane of the first optical channel which showed a uniform the irradiance across the sensor. The image of the LED on the thread is 0.45 mm in length and 0.15 mm in width, which corresponds to the diameter of the thread. When the light scattered by the thread is focused onto the CCD sensor by the first optical channel (i.e. lenses L1 and L2) the size of geometrical spot is on the CCD sensor is 0.04 × 0.12 mm, or about 1.5 × 4 pixels.

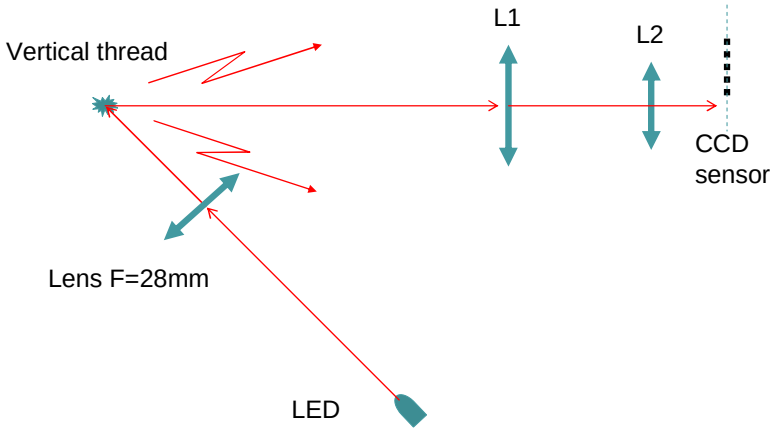

Figure 2.12: Sketch of the experimental setup for PSF measurement of the first optics channel.

We measured the PSF of the first channel by progressively shifting the bright central spot in the image of our source away from the active area of sensor of CCD camera via a mechanical linear actuator and successively applying neutral density filters to attenuate the light to avoid saturating the CCD. By means of this technique we were able to utilize the whole size of the CCD sensor and achieve a dynamic range DR~10^7. The results are shown in Fig. 2.13.

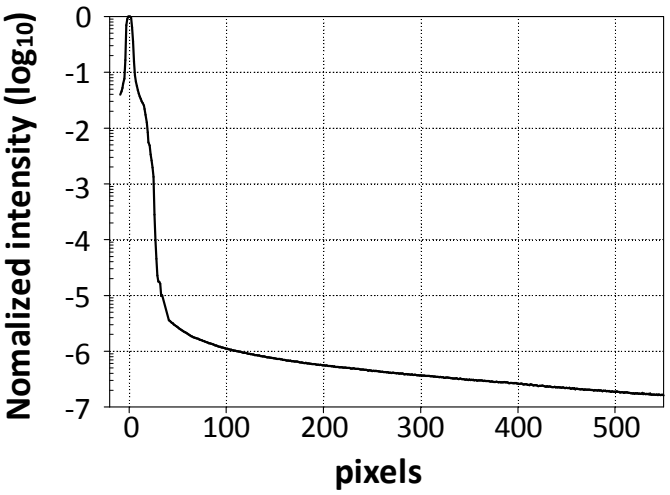

Figure 2.13: Measured PSF of the first optical channel.

We note that the measured PSF has a much wider FWHM than the PSF, calculated from diffraction theory, i.e. the Airy disk. Furthermore, the intensity of the wings of the measured PSF in the interval 100-500 pixels is several orders of magnitude greater than the level calculated from diffraction theory. This is due to the combined effects of scattering, aberration, non-uniformities and diffraction in all the elements in the optical transport. The importance of this measurement will become apparent later when we discuss the dynamic range measurements.

Also, because of the finite size of our source, the measured PSF differs from that of a 'true point source', especially in the region close to the source. However, at large distances from the source the intensity distribution will be close to that of the 'true PSF' because it is not affected by the size of the source at sufficiently large distances, i.e when ratio of distance over the source size is large.

2.6 Simulation tool

2.6.1 Trace3D

TRACE 3-D [34] is an interactive beam-dynamics program that calculates the envelopes of a bunched beam, including linear space-change forces, through a user-defined transport system. In TRACE 3-D, the basic assumption is that all forces are linear or can be linearized. To linearize the space charge, the distribution of the beam should be postulated as uniform in real space. In realistic sense, the beam distribution is never uniform, so the envelope in this code is in RMS sense. Several element-fitting and beam-matching options are available that determine values for the beam-ellipse parameters or for specified transport-system parameters (such as quadrupole gradients) to meet specified objectives. In this dissertation, I use it for beam matching and mismatch mode generation for experiment.

2.5.2 WARP

In UMER, we use a self-consistence PIC code called WARP to simulate the beam behaviors [35]. It allows nonlinear space charge, emittance growth, image charge forces and arbitrary distribution that most matrix codes or tracking codes don't have. It has been successfully benchmarked against UMER experimental data in the past [36]. In the simulation, considering the computing power, we usually use macro particles. Each macro particle represents millions of particles in the realistic sense. The macro particles are advanced in a transverse slice under the impact of external forces and self-consistent self-fields using the leap-frog algorithm. In the code, we calculate the self-filed on a mesh of sufficient resolution to capture the beam potential variations. In our case, it has been

shown to be accurate to use the x-y 2.5 dimension model [37] since the beams in UMER I use is about long enough compared to the pipe diameter and we focus on the transverse dynamic mostly in the longitudinal center of the beam in a short longitudinal distance. For large longitudinal distance, we might need full 3D simulation or keep 2.5D version to compare with the experiment results when the longitudinal confinement is applied e.g. using the longitudinal focusing [38].

2.7 Chapter conclusion

In this Chapter, I introduce the experimental environment of UMER. I discuss several basic diagnostics including the actuator and screen system, the imaging system and tomography method for phase space reconstruction. Followed by my master thesis, I discussed the optical properties of the novel adaptive masking method for halo imaging. Finally, I discuss the simulation tools that will be used later.

Chapter 3: Transverse Matching of Space Charge Dominated Beam

For a space charge dominated beam, transverse envelope match plays an essential role in control of beam loss and halo formation. It is believed that a mismatched beam will drive a parametric resonance that force the particle moving back and forth around the center core and then leaving to large radius. This well-modeled mechanism will speed up other processes forcing the individual particle near the beam edge to create halo. Especially in a ring, integer, half integer or higher order resonance will be amplified by this mechanism, and fasten the process which degrades the beam quality and eventually results in beam loss. Here I present a general way to obtain an envelope match for space charge dominated beams, and tried to eliminate the source for halo generation and beam quality degradation. The ultimate goal is to achieve a halo free beam for further study of the mechanism of different halo formation sources. The organization of this chapter is as follow. We first address an Eddy current problem [39] that we realized and then solved. Then it follows with discussion of the concept of basic envelope match of the space charge dominated beam. After that, envelope matching will be addressed with beams of different space charge levels or intensities.

3.1 Verify Eddy current of pulsed quadrupole and its compensation

YQ and QR1 are special type printed circuit quadrupoles due to its location and functionality that they provide confinement for both injection and recirculation (see Fig. 2.1). The radius from the printed circuit to the center of the quadrupole is more than twice larger than the normal quadrupole used in the ring or injection for the pipe merging.

Accordingly, the current applied to the circuit should be larger to generate the same magnetic confinement. The principle current value for the power supply of YQ and QR1 should be around 4.6 A. Since we don't have a water cooling system for the quadrupoles, there are concerns that YQ and QR1 could be overheated and burn if their currents are DC. Thus YQ and QR1 are pulsed for certain amount of time (~0.2 ms) each injection (60 Hz), and usually good for more than 1000 turn operation of the less space charge beam in UMER. In the past, YQ are usually set to over 6.5 A (instead of ~4.6 A) to allow most of the beam go through. This introduces a big error in the match in the first turn which deviates from the code prediction.

In order to study the difference of current setting, I performed a scan of YQ and QR1. By taking 6mA beam images at the first screen downstream (at RC1), I compared the results in experiment and simulation. Note that, before the comparison in RC1, I found good beam size agreements between experiment data and simulation in both IC1 and IC2 of the injection with different solenoid current values as well as different values of Q1, Q2, and Q3. This indicated a good model of regular quadrupoles and solenoid in UMER. However, the model failed at RC1 when I did a scan of YQ. Fig. 3.1 shows a plot of beam sizes vs. YQ current. From the plots, I found that the curve of $2*Y_{rms}$ from experiment (purple solid line) is stretched and offset from the simulation curve (green dot line).

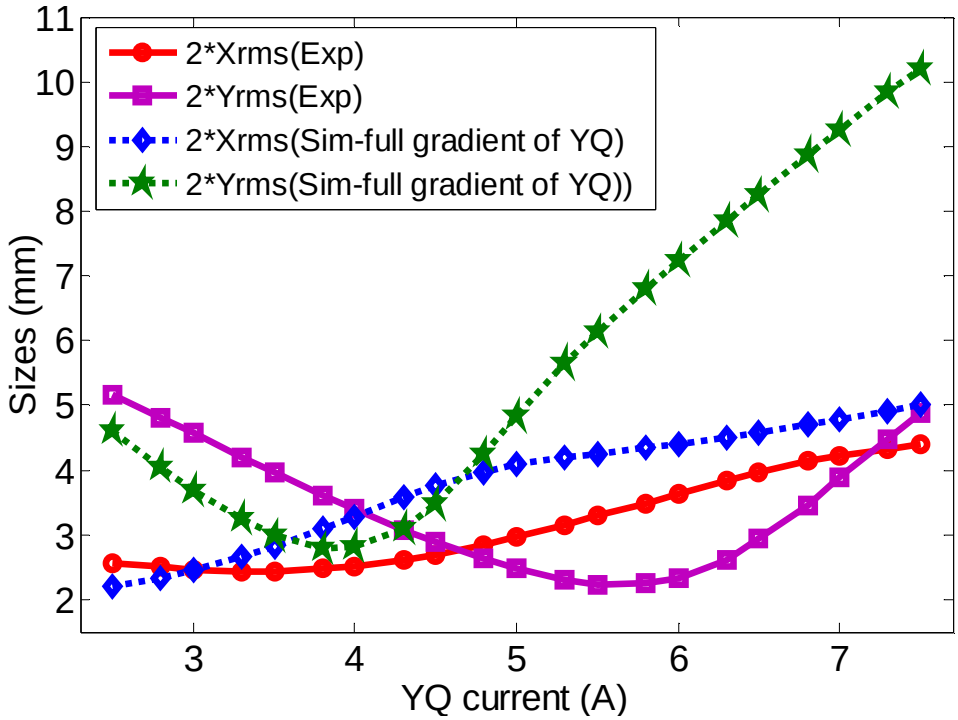

Figure 3.1: Comparison of beam sizes between experiment and simulation before correction.

It is not hard to have a guess that the simulation model for YQ has a bigger peak gradient per ampere than experiment. I compared the difference of two curves, which gave us an empirical value of ~0.67, which I applied to reduce the peak gradient per ampere for YQ in simulation to match with experiment. After this modification, the comparison result is shown in figure 3.2. It is getting close although not perfect, and this could be due to the same error by QR1.

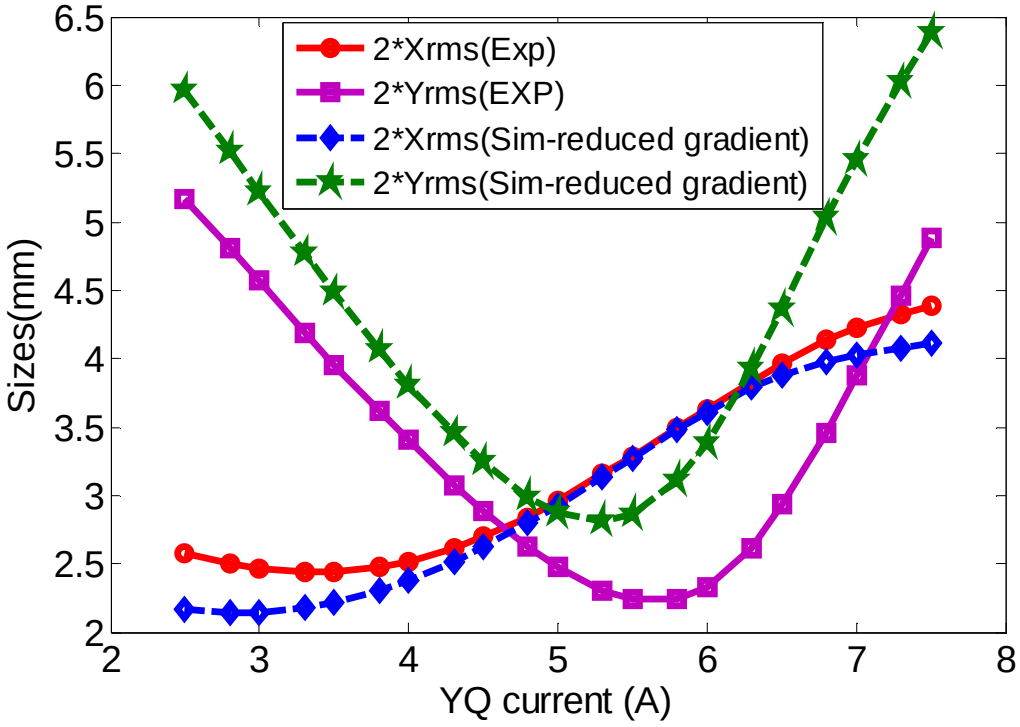

Figure 3.2: Comparison of beam sizes between experiment and simulation with peak gradient per ampere for YQ model lowered by 0.67

From the previous experience, if we set YQ as 7.3 A, the beam is good for several turn but lost very quick. At the meantime, if we set YQ as about 4.6 A, the value from code for beam matching, the beam is lost first turn but finally the loss is much less than previous one. This phenomenon indicates that the YQ and QR1 strengths might be changed during each time the beam go through Y-section. If we consider that YQ and QR1 are pulsed, it is straightforward that there is Eddy currents in both quadrupoles. Assuming the beam is injected into Y-section too soon, before the Eddy currents in YQ and QR1 have fully stabilized, the peak field will be weaker; this can only be partially compensated by increasing the YQ current (e.g. set YQ current 7.3 A, the actual value is about 4.6A for first turn). As the transients die down, the fields inside YQ will continue

to increase, mismatching and kicking the recirculating beam during each turn. This can explain the 1%/turn beam loss seen during the first 20-30 turns. In other words, an YQ current of 7.3 A is initially seen as 5 A. As the Eddy currents die down, the field inside keeps increasing, sweeping the beam towards a wall downstream. Thus, by increasing the width of these pulses and pre-pulsing them earlier, we should be able to operate YQ, QR1 at currents of 4.6-4.8A and obtain good transport and matching.

Following this assumption, we will test the effect of different pre-pulse of YQ and QR1 on beam dynamics. In order to do that, the TTL triggers to YQ and QR1 were separated so that both could be independently delayed while the other remained fixed.

We first test the different pre-pulse for YQ. This measurement was performed using the PIMAX-II camera located at RC1 to image the beam on the 1st turn. The injection pulsed dipole, gun trigger and camera trigger remained fixed while the overall YQ pulse delay was adjusted such that it sampled different regions of the pulse in time. Fig. 3.3 below illustrates the concept.

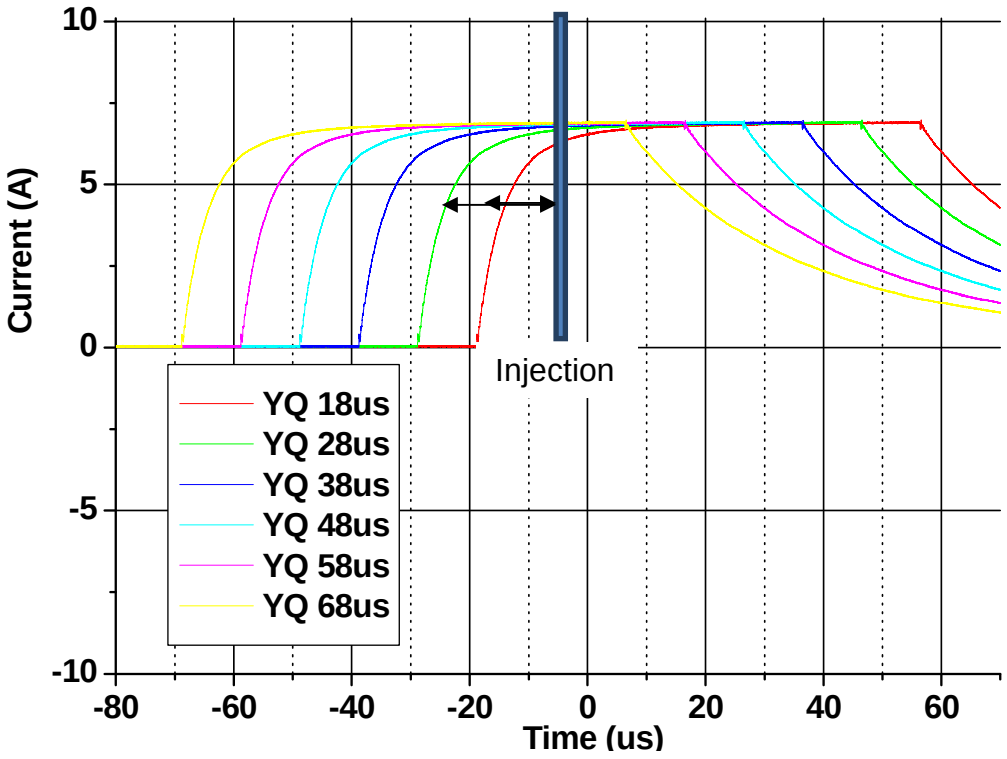

Figure 3.3: YQ current profiles at different injection points. The injection pulse from the pulse dipole is illustrated as the rectangular box at time 0s. The horizontal axis is time and the vertical axis is current.

The YQ pulse delay was shifted in 10 μs steps, beginning with an 18 μs pre-pulse (pre-pulse is the period of time beginning from the turn on of the YQ pulse to the turn on of the injection dipole pulser). Screen images are illustrated below in Fig. 3.4 for the 6mA beam.

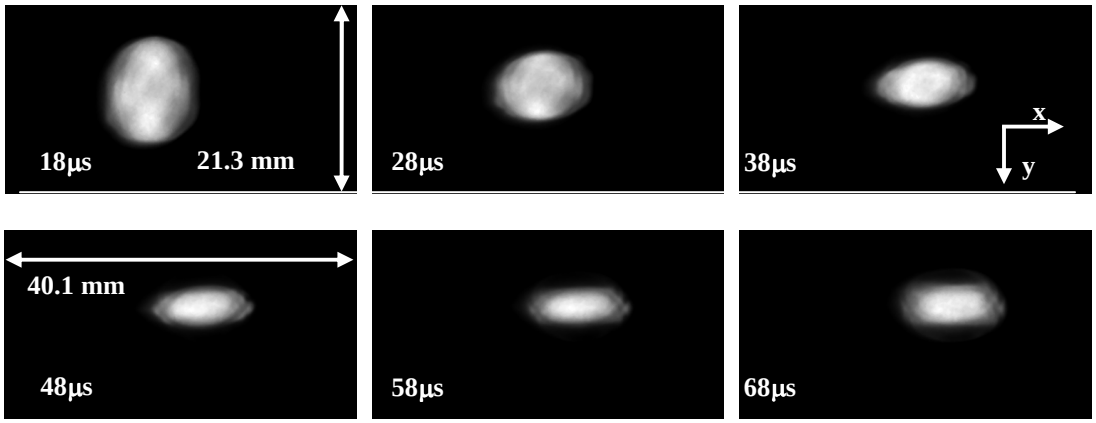

Figure 3.4: Screen images at RC1, measured at different injection points of the YQ pulse for the 6mA beam (as shown in Fig. 3.3).

The x and y centroids as well as the rms beam sizes, obtained from these images, are illustrated in Fig. 3.5 below.

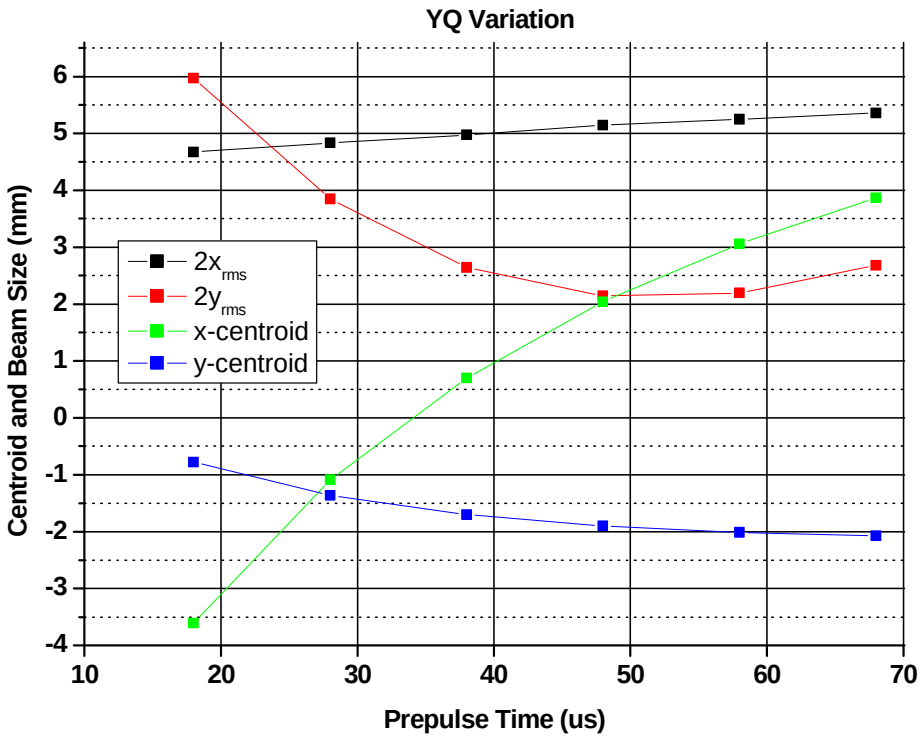

Figure 3.5: X, Y centroids and beam sizes from screen images, measured at different injection points of the YQ pulse for the 6mA beam (as shown in Fig. 3.3). The horizontal axis is the prepulse time and the vertical axis is the x, y centroid or beam size.

The x-centroid and vertical beam size changes substantially over the limited pre-pulse time explored in this experiment. The original machine parameters set a pre-pulse of 38 us, but as seen in Fig. 3.4 and 3.5; both are still changing beyond that period. Vertically, the beam reduces in size overall by 64% at the waste and horizontally, the centroid drifts by 7.5 mm over 50 us, and continues to drift but at a slower and slower rate.

Then we test QR1 with different pre-pulse. This measurement was also performed using the PIMAX-II camera located at RC1 to image the beam on the 1st turn. Once again, the injection pulsed dipole, gun trigger and camera trigger remained fixed while the overall QR1 pulse delay was adjusted such that it sampled different regions of the pulse in time. The QR1 pulse delay was shifted in 10 us steps, beginning with an 18 us prepulse. Screen images are illustrated below in Fig. 3.6.

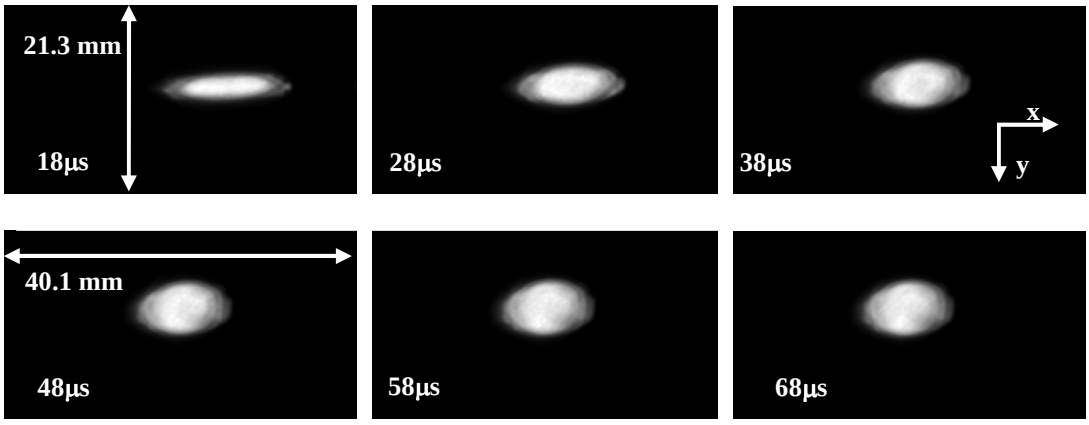

Figure 3.6: Screen images at RC1, measured at different injection points of the QR1 pulse for the 6mA beam (as shown in Fig. 3.3).

The x and y centroids as well as the rms beam sizes, obtained from these images, are illustrated in Fig. 3.7.

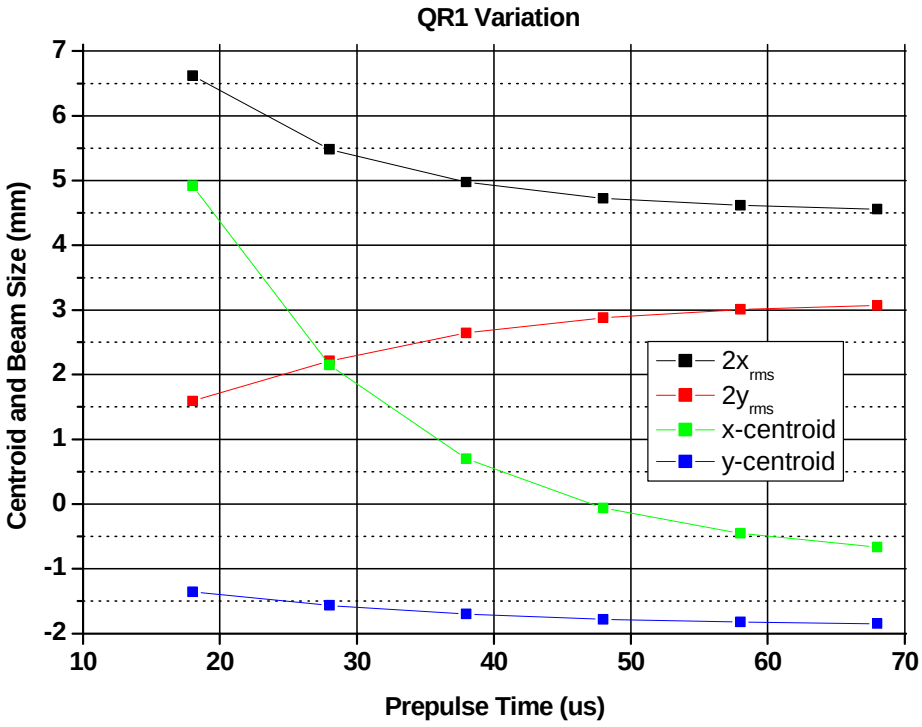

Figure 3.7: X, Y centroids and beam sizes from screen images, measured at different injection points of the QR1 pulse for the 6mA beam (as shown in Fig. 3.3). The horizontal axis is the prepulse time and the vertical axis is the x, y centroid or beam size.

For QR1, the centroid and beam size settled down sooner than YQ, as this magnet sits above a reducer and does not sit above a metal block that houses the injection and recirculation beam pipes as YQ does.

We then lengthen the YQ and QR1 pulses close to the existing limits of the power supplies. Beam current each turn were then captured for various injection cases, where the delay of injection pulse and YQ current was varied. This experiment was performed by capturing beam current traces from the wall current monitor at RC10, beginning with the nominal operating case using a matched setting calculated from code. The QR1 pulse was fixed in amplitude for all cases presented below, but the pre-pulse time was varied along with YQ amplitude. Figs. 3.8 a-b and 3.9 a-b below illustrates the results.

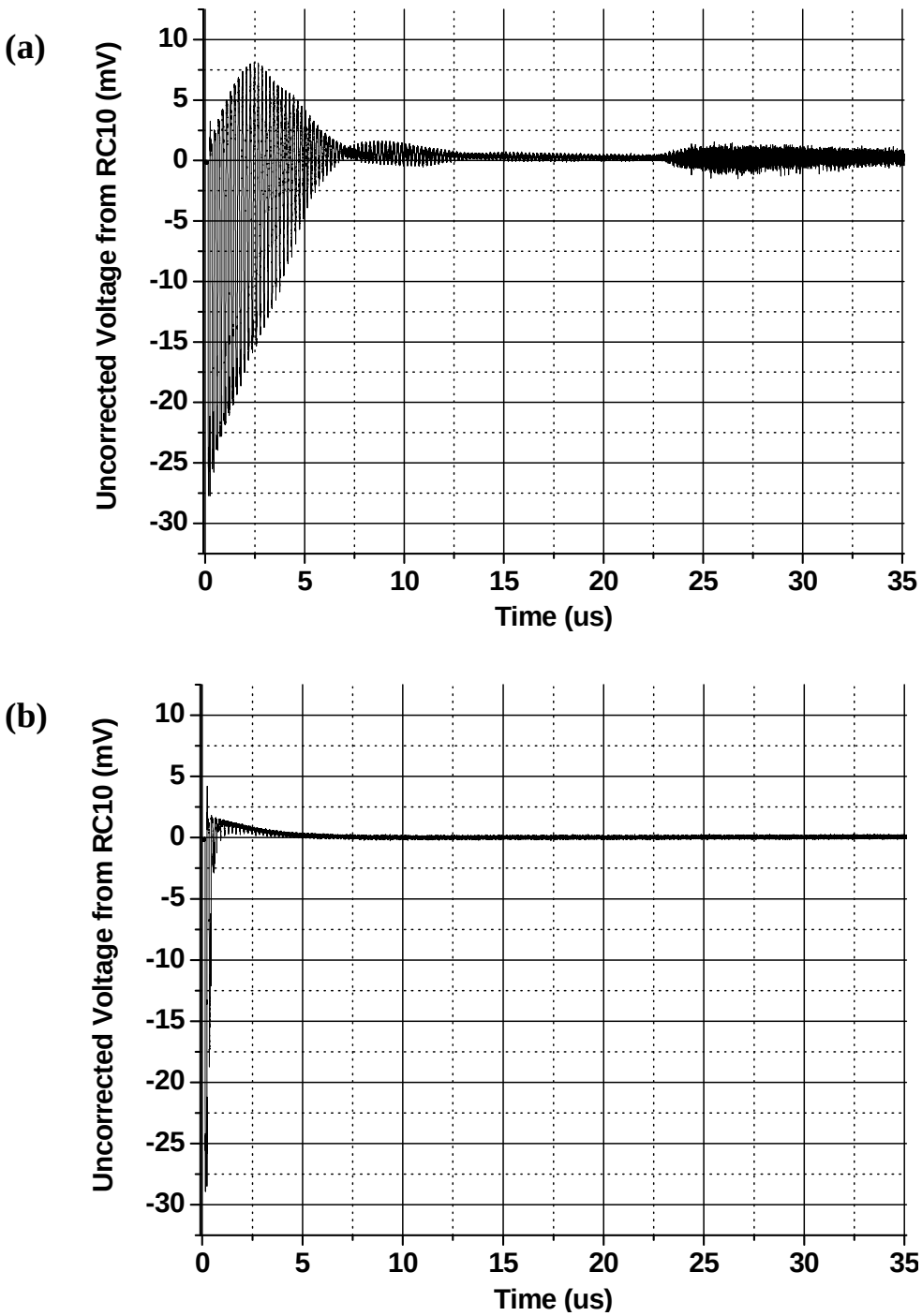

Figure 3.8: Beam current measured at the RC10 wall current monitor, (a) -38 μs pre-pulse with an YQ current of 6.51A; (b) 208 μs pre-pulse with an YQ current of 6.51A. The horizontal axis is time and the vertical axis is the uncorrected voltage from the oscilloscope.

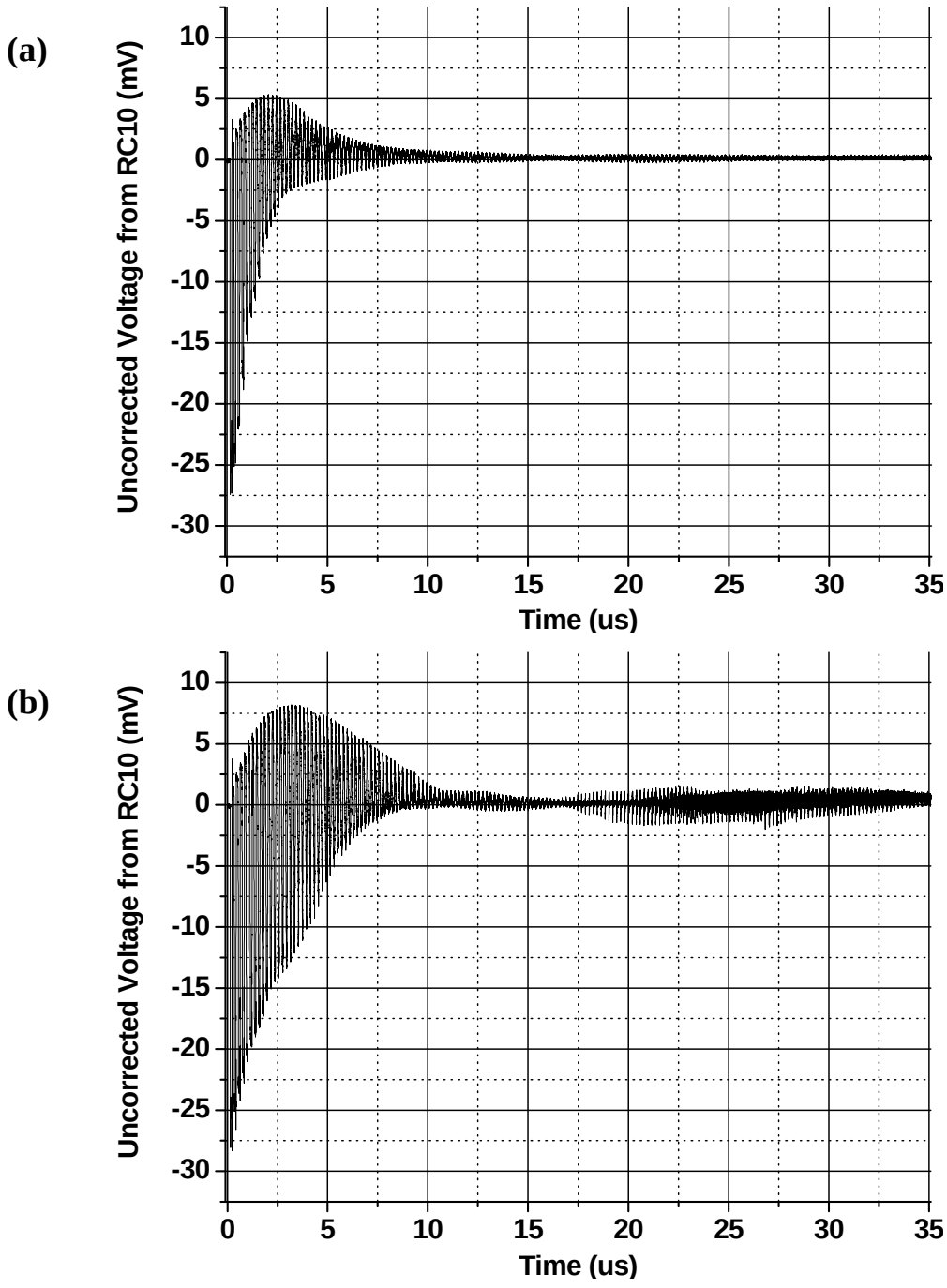

Figure 3.9: Beam current measured at the RC10 wall current monitor. (a) -38 μs pre-pulse with an YQ current of 5.34 A, (b) -208 μs pre-pulse with an YQ current of 5.34 A. The horizontal axis is time and the vertical axis is the uncorrected voltage from the oscilloscope.

When we operate the magnets with the original 38 μs pre-pulse, with YQ and QR1 at a current of 6.51A and 5.34A respectively, we obtain many turns, as shown in Fig. 3.8a. If we extend the prepulse to 208 μs (as shown in Fig. 3.8b), then we lose those turns. If we then reduced the strength of the YQ magnet to 5.34A (as shown in Fig. 3.9b), we obtain multiple turns again, indicating that the transients are settling down and were approaching the actual effective strength of the magnet.

Finally, the settings that are being used currently have a pre-pulse of 258 μs. We are able to run YQ and QR1 at values of 4.638 A and 4.754 A, respectively and obtain multiple turns as shown in Fig. 3.10.

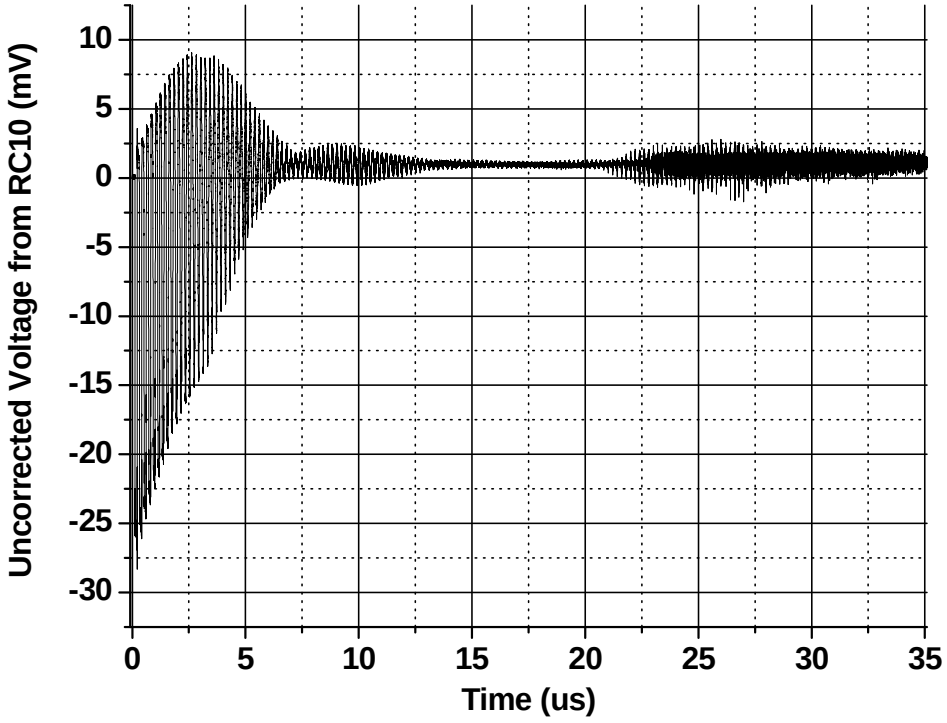

Fig. 3.10: Beam current measured at the RC10 wall current monitor with a 258 μs pre-pulse and YQ current of 4.638A and QR1 of 4.754A. The horizontal axis is time and the vertical axis is the uncorrected voltage from the oscilloscope.

3.2 General concept of envelope match for UMER beam

As can be seen for UMER configuration, the envelope match includes three sections: injection, Y section and ring section.

There are 35 FODO cells in the ring section. Each cell is 32 cm long, with focusing and defocusing quadrupoles located in 8 cm and 24 cm, and dipole in 16 cm related to the start of each cell.(Note that the focusing or defocusing here means for x-direction, and they are opposite for y direction, similarly hereinafter.) The dipole bends the ideal path of the electron beam by 10^0 (see Fig. 2.1). In our model, we ignore the dispersion by assume there is no energy spread. By this simplification, we can ignore the dipole component in the ring. However, if considering the contribution of the edge focusing from dipole, we should modify the calculation model by adding a small focusing quadrupole both in X and Y direction in each cell as shown in Fig. 3.11. Notice that there is a small difference in the focusing strength by dipole will result in the slightly asymmetry of the envelope in horizontal and vertical axes.

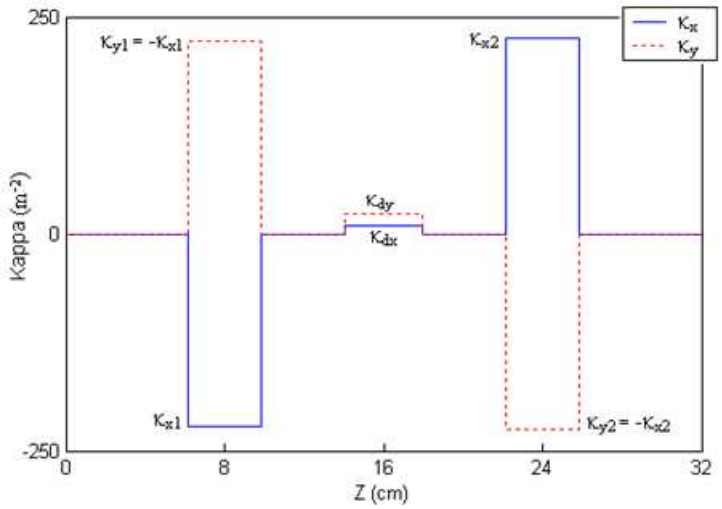

Figure 3.11: Diagram of UMER FODO lattice in one period

Y section is a special UMER type FODO. The dipole is pulsed for both injection and recirculation. The radius of the pipe in Y section is larger than in the ring, to allow pipe merging and a bigger acceptance. As a result, the quadrupole YQ and QR1 is bigger than normal quadrupole in UMER and need more current to create the same field as in the ring which will brings more heat. For overheat issue from that high current, YQ and QR1 are pulsed in order to reduce heat as discussed in Section 3.1. Moreover, YQ provides focusing for both injection and recirculation, each with its pipe coming in with an angle and an offset in x direction, which actually complicate the match geometrically.

In a FODO focus system, envelope match indicates the beam envelope and slope have a period the same as the FODO cell period (see Eqn. 3.1). Practically, It simply means the two pair of parameters (both in x and y) are identical when entering and exiting the FODO or at the mid-plane of two adjacent cells. When the quadrupoles' strengths are fixed, for electron beams in UMER with certain current without considering transverse emittance growth, the match condition (the envelope size and slope) in the beginning of each FODO is determined. It can be directly derived from the envelope equations (see Eqn.3.2) with the periodic boundary condition as shown in Eqn. 3.1.

$$\begin{aligned} X(s+S) &= X(s), Y(s+S) = Y(s) \\ X'(s+S) &= X'(s), Y'(s+S) = Y'(s) \end{aligned} \tag{3.1}$$

$$X'' + k(s)^2 X + \frac{K(I)}{X} + \frac{\varepsilon^2}{X^3} = 0 \tag{3.2}$$

where s is ideal beam path coordinate, S is the period of the lattice, X, Y, X',Y' represent the transverse beam RMS sizes and slopes, K is the generalized perveance which depends

on beam current I, ε is the effective emittance and k is the field strength which depends on the lattice setting.

The injection is designed to match the initial beam parameter from aperture to the required match condition determined by the ring FODOs. Fig. 3.12 shows a diagram of the whole injection, Y-section and partial ring in UMER, where the SD, Q, PD, YQ, QR represent steering dipole, quadrupole, pulsed dipole, Y-shape quadrupole and ring quadrupole respectively. Note in Eqn. 3.2, k^2 is also dependent on quadrupole currents. From a known initial size and slope from the aperture, through the whole injection to obtain an envelope match condition before entering the ring, we have six quadrupoles and one solenoid to vary. Since there are only four constraints, the envelope size and slope in both x and y direction, it is enough to use only four quadrupoles to satisfy them. We usually fix the solenoid field. Q1 is the quadrupole close to the solenoid, which will separate the beam from radial symmetry to asymmetry. To avoid the effect from unbalanced image charge forces from too much asymmetry between horizontal and vertical axes and reduce the overlap of the fringe field between solenoid and Q1, we fix Q1 with a small value with respect to the ring quadrupole. Under all these considerations, the four quadrupoles used to optimize the matching solution in the injection are Q2-Q6. We usually only scan 4 of them, but we also add some flexibility when the solution cause too much asymmetry in the injection which could introduce a nonlinearity to the beam distribution.

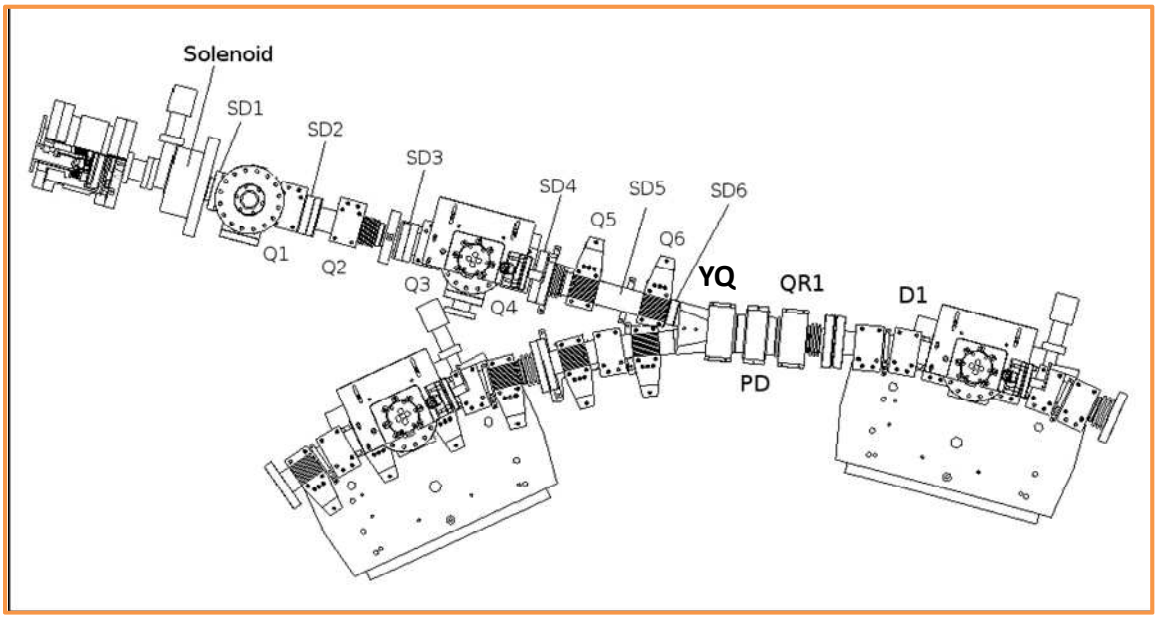

Figure 3.11: Magnet components in UMER injection for matching.

3.3 Simulation code used for envelope matching

I used a tracking code Trace3D to get a match solution. Trace3D assumes linear field and no emittance growth, and have variety types of matching procedure, which is suitable for our beam experiment to get a rough match solution. Here, I use the emittance value from solenoid tomography result to replace the emittance in the ring with the assumption of no emittance growth. This is well enough since I only use the code for a rough condition. Later results will show that when beam current increase, nonlinear force will become more and more obvious, and the linear assumption of Trace3D is no longer that valid. Thus, the solution from the Trace3D will be less accurate. However, the solution will still be a starting point to start with when I discuss the empirical method later.

For beam match in Trace3D, I start with the ring section. From the start to the end of each FODO cell, I can use Type 1 match procedure in Trace3D to get a solution of Twiss parameters which give a match solution inside the ring. As indicated by envelope equation, this solution is determined by the assumed emittance and the predefined lattice setting, specially the ring quadrupole strength. In UMER, the ring quadrupoles are setting to 1.826A with positive and negative alternating. In this way, the tune will be 6.694 away from the integer and half integer resonances. This quadrupole setting is not a necessary requirement, and be varied to any value which will give a new lattice and result in new matching Twiss parameters. For example, UMER could work at 2.220A, 2.068A, 1.518A for ring quadrupole, which give a tune about 7.630, 2.068, and 1.518 respectively. Note that, Twiss parameter is used in Trace3D or other accelerator field generally instead of beam size and slope which can easily interchange to each other through Eqn. 3.3.

$$\begin{aligned} \beta_{x(y)} &= X(Y)rms^2 / \varepsilon \\ \gamma_{x(y)} &= X'(Y')rms^2 / \varepsilon \\ \beta_{x(y)}\gamma_{x(y)} &= 1 + \alpha_{x(y)}{}^2 \end{aligned} \tag{3.3}$$

After I got the matched Twiss parameters for ring section, particularly the initial parameters in the beginning, we need to use the same Twiss parameters to determine the quadrupole settings for Y-section, which will allow the beam have a multiple turn match. Since one matched the beam for four independent Twiss parameters, α_x, α_y, β_x, and β_y, typically one needs four quadrupoles to do this job as the same as the discussion in the injection section. Therefore, I include QR71 and QR2 into this section and use Type 8 matching procedure in Trace3D to find the solution for QR71, YQ, QR1 and QR2.

Next step is to find appropriate injection quadrupole settings with the YQ and QR1 strength determined from multiple turn requirements and a matching condition from the ring lattice requirement. The components here will be solenoid, Q1-Q6, YQ, PD and QR1. The lattice starts from the aperture and ends with the entrance of a regular FODO cell. I set YQ and QR1 value from previous Y-section match, and input the final Twiss parameters as the matched initial Twiss parameters in the ring section. I also set the initial Twiss parameter for the injector as the ones I got from Solenoid Tomography. Using a Type 8 matching procedure in Trace3D, I will finally get a quadrupole setting of Q2-Q5.

3.4 Empirical method using response matrix

In practice, many factors, such as beam initial properties, lattices imperfection, vacuum condition and etc., will affect calculations and simulations, and make them deviate from experiments. The magnets strength obtained though calculation and simulation does not necessarily yield a good matching condition as showed previously. A further empirical method [40] will be used to achieve the final match. Here, I first assume the mismatch is small (linear approximation), so that a matrix implementation could be applied. Followed the previous discussion, I use the quadrupoles Q2 – Q5 for online adjustment and the matrix form is as follows:

$$\begin{pmatrix} X_i \\ Y_i \end{pmatrix}_{I_2,I_3,I_4,I_5} = \begin{pmatrix} X_m \\ Y_m \end{pmatrix} + \begin{pmatrix} R_{xi2} & R_{xi3} & R_{xi4} & R_{xi5} \\ R_{yi2} & R_{yi3} & R_{yi4} & R_{yi5} \end{pmatrix} \begin{pmatrix} \Delta I_2 \\ \Delta I_3 \\ \Delta I_4 \\ \Delta I_5 \end{pmatrix} \tag{3.4}$$

Where

X_i and Y_i are the 2×rms transverse beam sizes in the i's screen, which is measured with

current magnet strength setting of I_2, I_3, I_4, I_5. X_m and Y_m is the matched beam size on each screen. ΔI is the magnet strength change from current setting to a better setting to minimize the mismatch. R_{wij} is the beam size response in i's screen when changing quadrupole j (w can be x or y), defined as

$$R_{w_i j} = \frac{\partial W_i}{\partial I_j} \tag{3.2}$$

and can be measured by perturbing the current quadrupole strength and observing the beam size in each screen. The full matrix form can be rewritten and extended as

$$\underbrace{\begin{pmatrix} X_1 \\ Y_1 \\ X_2 \\ Y_2 \\ \cdots \\ X_n \\ Y_n \end{pmatrix}}_{E} = \underbrace{\begin{pmatrix} R_{x11} & R_{x12} & R_{x13} & R_{x14} & 1 & 0 \\ R_{y11} & R_{y12} & R_{y13} & R_{y14} & 0 & 1 \\ R_{x21} & R_{x22} & R_{x23} & R_{x24} & 1 & 0 \\ R_{y21} & R_{y22} & R_{y23} & R_{y24} & 0 & 1 \\ \cdots & \cdots & \cdots & \cdots & \cdots & \cdots \\ R_{xn1} & R_{xn2} & R_{xn3} & R_{xn4} & 1 & 0 \\ R_{yn1} & R_{yn2} & R_{yn3} & R_{yn4} & 0 & 1 \end{pmatrix}}_{R} \cdot \underbrace{\begin{pmatrix} \Delta I_1 \\ \Delta I_2 \\ \Delta I_3 \\ \Delta I_4 \\ X_m \\ Y_m \end{pmatrix}}_{\Delta} \tag{3.3}$$

or simplified as

$$E = R\Delta \tag{3.4}$$

This is standard linear equations, and the optimal solution can be obtained in a least square sense, i.e. $\Delta = (R^{\mathrm{T}}R)^{-1}R^{\mathrm{T}}E$. A better injection setting is given by I_1- ΔI_1, I_2- ΔI_2, I_3- ΔI_3, I_4- ΔI_4. Details for this method can be referred to [40].

I test this method with the simulations in Warp by scanning the quadrupoles Q2-Q5, and monitoring the envelope change in periodic point, e.g. the screen position in the ring. Fig. 3.13 shows the comparison of before empirical correction (red star points) and the one after the empirical correction (blue circle point). There is an obvious improvement since the deviation of the beam sizes is much smaller after the empirical correction both in X and Y directions. In real experiment, one might need several implementations of this method to let the solution converge.

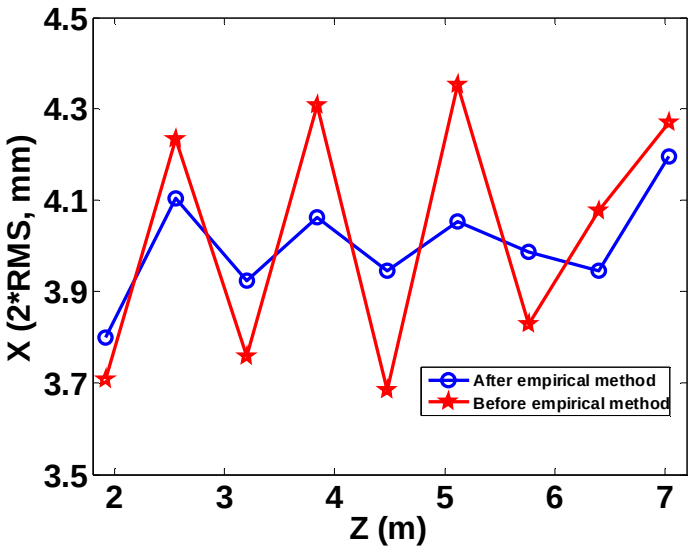

(a)

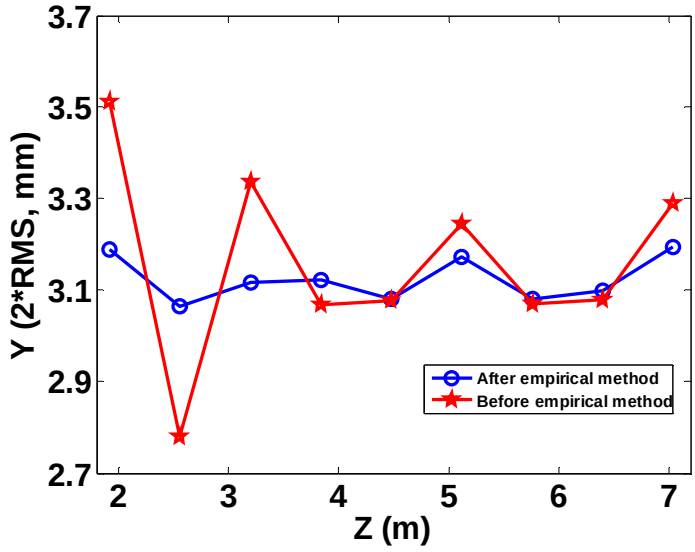

(b)

Figure 3.13: Simulated beam sizes in screen location before and after empirical method: (a) $2*X_{rms}$ (b)$2*Y_{rms}$

3.5 Correction for Skewness

Due to fringe field of solenoid and rotation error of injection quadrupoles, there will be a beam rotation complicating beam match. Here I use two skew quadrupoles in Q3 and Q6 to correct this rotation. The skew quadrupole is a type of UMER quadrupole with a normal pair of printed-circuits [40] and a 45-degree rotated pair as in Fig. 3.14. Each pair is powered by different current supplies, so the normal and skew components can be independently adjust. By scanning the skew quadrupoles and comparing the rotation angle of beam images in each chamber, one can minimize the rotation in least square sense similarly to the empirical matching.

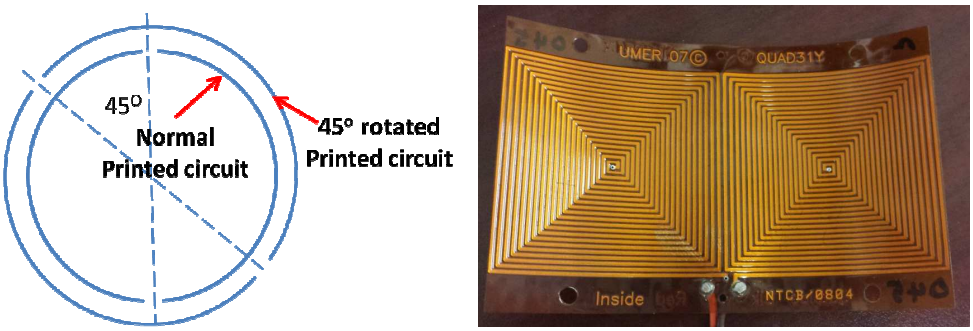

Figure 3.14: schematic diagram of (a) skew quadrupole and (b) piece of printed circuit.

Next sections, I will use these basics to discuss three specific matching cases of UMER beams.

3.6 Transverse beam matching for 6mA beam

As indicated by the name, the beam current for this case is 5.96 mA close to 6 mA. The initial conditions are obtained from the beam phase space plot which is reconstructed from solenoid tomography. The reconstructed plot in x direction is shown in Fig. 3.15. For symmetry of two transverse directions at aperture and through solenoid, I found an initial condition listed in Table 3.1.

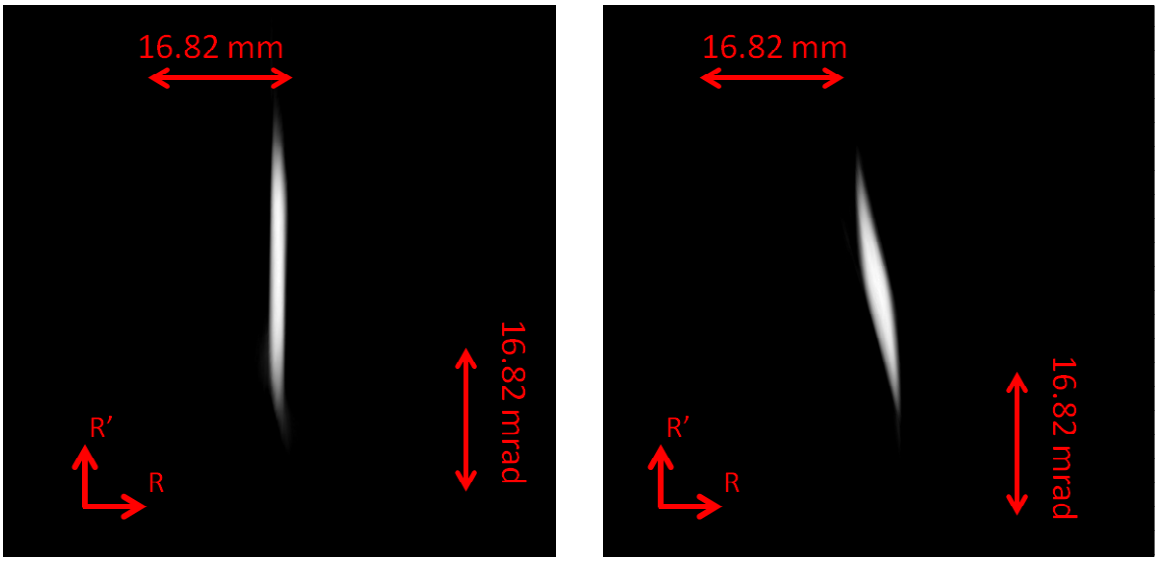

Figure 3.15: R-R' phase space plot of 6mA beam in aperture (a) and IC1 (b)

Table 3.1: Initial parameters of 6 mA beam

Initial envelope values	X (mm)	X' (mrad)	Y(mm)	Y'(mrad)	Emittance(um rad)
At aperture	0.88	-16.20	0.88	-16.20	13.0
At IC1	2.52	-7.09	2.52	-7.09	13.0

For ordinary operation setting, the ring quadrupoles is fixed to 1.826 A, which corresponding to a hard edge model of 659.0 G/m in strength, 4.475 cm in effective length. This results in a tune of 6.694. Using this hard edge model in trace3D, I found an envelope match solution in the ring listed in Table 3.2.

Table 3.2: Envelopes and slopes in 3 location for a matched 6 mA beam from Trace3D

Parameter	Mid-plane of ring dipoles	Mid-plane of BPMs	Screen
X (mm)	3.14	3.13	3.49
X’ (mrad)	11.78	11.88	12.86
Y (mm)	3.04	3.01	2.69
Y’ (mrad)	-11.87	-11.44	-10.38

The hard edge models used for quadruples in Y section are listed in Table 3.3. Using the match Parameter, I first obtain the setting for YQ and QR1 for recirculation using the match solver in Trace3D, which is 4.646 A and 4.735 A.

Table 3.3: Hard edge model of UMER quadrupole [41]

Quadrupole type	Effective lenghth (cm)	Peak Gradient per A (G/cm/A)	Hard edge factor	Average Gradient per A (G/cm/A)
Injection	4.475	3.609	0.8354	3.015
YQ	5.833	1.110	0.8557	0.950
QR1	5.999	1.010	0.8965	0.905
Ring	4.475	3.609	0.8354	3.015

I input the initials and match solution into trace3D code, and use its match module to get the current settings for injection quadrupoles. I use the same lattice as discussed in previous section. I obtain a current setting for matching shown in Table 3.4. The beam envelope from aperture to the second FODO is plotted in Fig. 3.16.

Table 3.4: Magnets location and matching solution for 6mA from Trace3D

Magnet	Sol	Q1	Q2	Q3	Q4	Q5	Q6
Position (cm)	17.13	40.53	53.73	72.73	92.33	106.63	122.63
Gradient (G/cm)	98.13	3.93	6.98	6.64	6.29	6.56	6.67
Current (A)	5.500	1.090	1.935	1.842	1.742	1.819	1.849

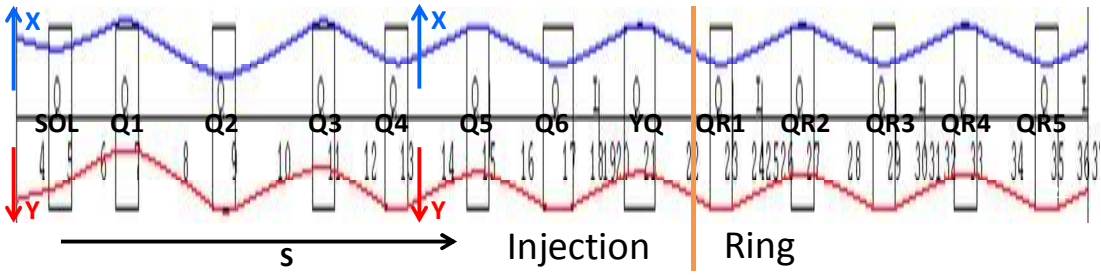

Figure 3.16: Envelope in injector for a match solution from Trace3D simulation.

In Fig. 3.17, I compare the beam images in each chamber before and after I solve the Eddy current problem. Both setting is from a solution of Trace3D. Since the field in YQ and QR1 is not built up thoroughly, there will be a huge mismatch caused by the field error. In both raw (a) of Fig. 3.17 and the plot in Fig. 3.18, one can see the oscillation of the beam sizes, which latter will be a source of halo formation and cause beam loss. From row (b), the beam still experience a small mismatch, and an empirical match and rotation correction will be performed later.

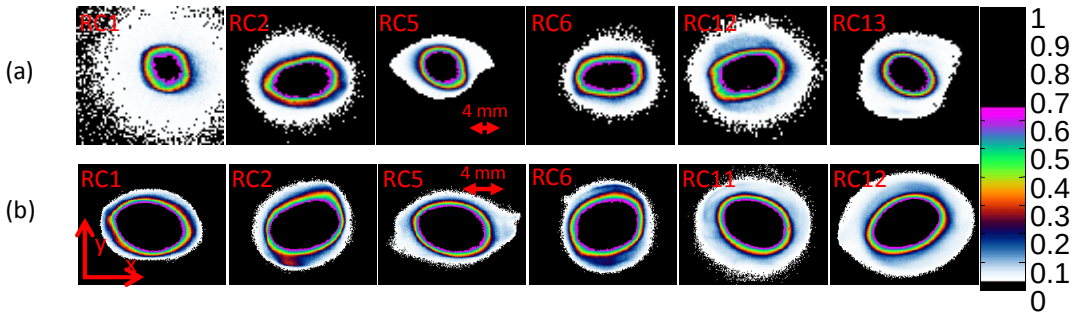

Figure 3.17: Comparison of beam (a) before and (b) after compensate Eddy current in experiment.

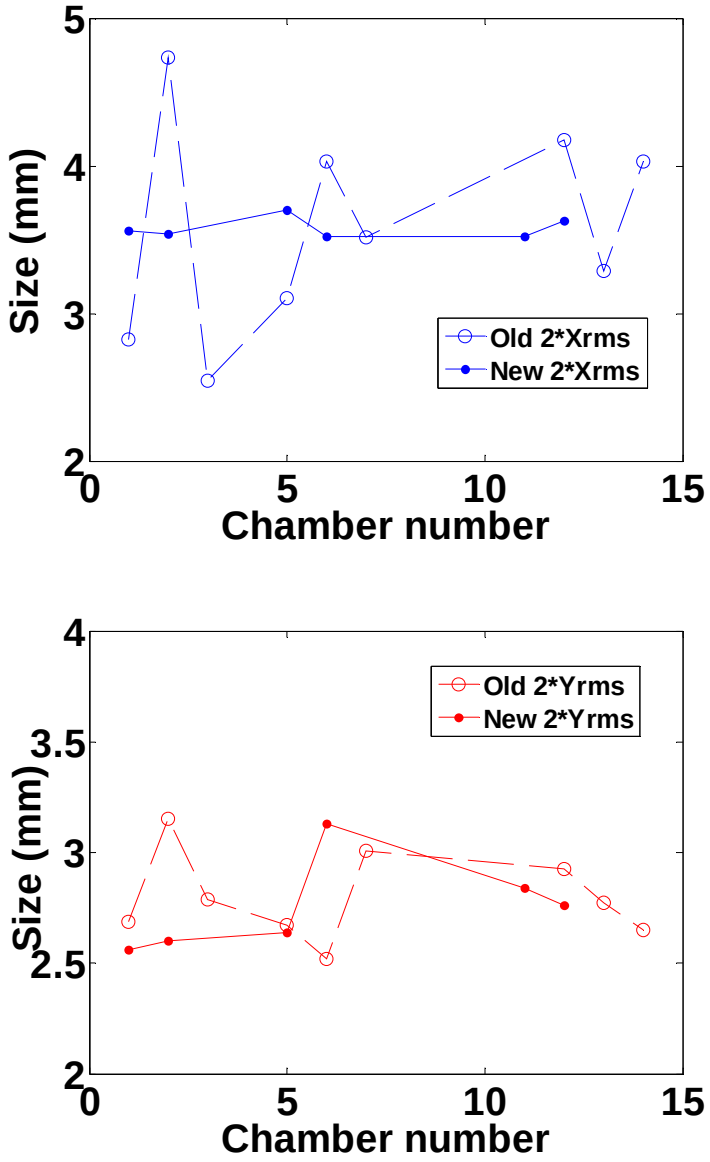

Figure 3.18: Comparison of beam sizes in each chamber before after beam match in experiment: x axis (upper); y axis (lower).

In practice, many factors, such as beam initial properties, lattices imperfection, vacuum condition and etc., will affect calculations and simulations, and make them deviate from experiments. I input the setting from Trace3D into experiment, and the result is shown in row (b) of Fig. 17 as well as row (a) of Fig. 19. Here, the beam is close to match, but not the perfect. I use empirical method to adjust the match, and then find a matched beam showed in the row (b) of Fig. 19. The final setting for Q2 – Q5 is 1.992 A, 1.785 A, 1.858 A, and 1.940 A. Comparing these two cases, I conclude that I get a more regular shape beam and the size difference is greatly reduced. The average size of beam in each chamber are 3.45 in x axis and 2.62 in y axis, which is very close to what I expect in Trace3D, 3.49 mm in x and 2.69 mm in y. The standard derivation of the beam sizes after empirical matching are 0.17 mm and 0.14 mm for x and y axis repeatedly. In general, by performing this beam envelope matching, the beam loss is reduced and the beam can propagate more turns without any loss.

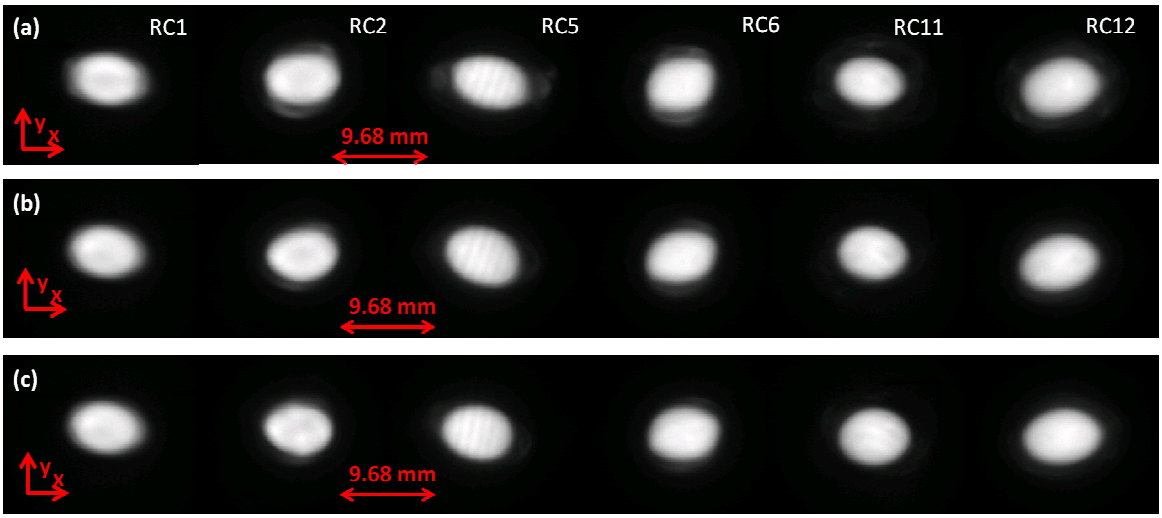

Figure 3.19: Beam images for 6 mA beam in each chamber for (a) solution from Trace3D, (b) after empirical match, (c)after empirical match and rotation correction.

Table 3.5: Beam sizes of 6mA for 3 cases in Fig. 3.19

Chamber (mm)	RC1	RC2	RC5	RC6	RC11	RC12
2*X_{rms} (Trace3D solution)	3.48	3.70	3.65	3.33	3.18	3.70
2*X_{rms}(Empirical match)	3.41	3.46	3.54	3.43	3.17	3.67
2*Y_{rms} (Trace3D solution)	2.46	2.73	2.55	2.96	2.35	2.76
2*Y_{rms}(Empirical match)	2.43	2.54	2.63	2.70	2.64	2.55

When viewing case after empirical matching, I notice that the beam have a rotation angle in different chamber, the data can be found in Table 3.5. I first suspect this angle could come from following sources: 1) imperfection of ring quadrupole such as rotation error, 2) the residual magnetic field from induction cell in RC4 and wall current

monitor in RC10, 3) asymmetry in YQ, and 4) the skewness of injection. I did a leveling of all quadrupoles in the ring and a demagnetization of induction cell and wall current monitor to reduce the rotation from source 1 and 2. I insert a new skew quadrupole in Q3 in the injection to correct the rotation in the injection and YQ since I found one previously installed skew quadrupole in Q6 is not enough to correct this rotation angle. The corrected beam images are shown in row (c) of Fig. 3.19 and the derivation of rotation angles (also see Table 3.6) is reduced from 15.0 degree to 6.9 degree.

Table 3.6: Rotation angle of the near match case for 6mA

Chamber	RC1	RC2	RC5	RC6	RC11	RC12
Rotation (degree)	8.63	-8.04	21.5	-16.8	8.85	-12.8
After correction(degree)	0.8	6.7	11.3	-6.7	0.0	-5.5

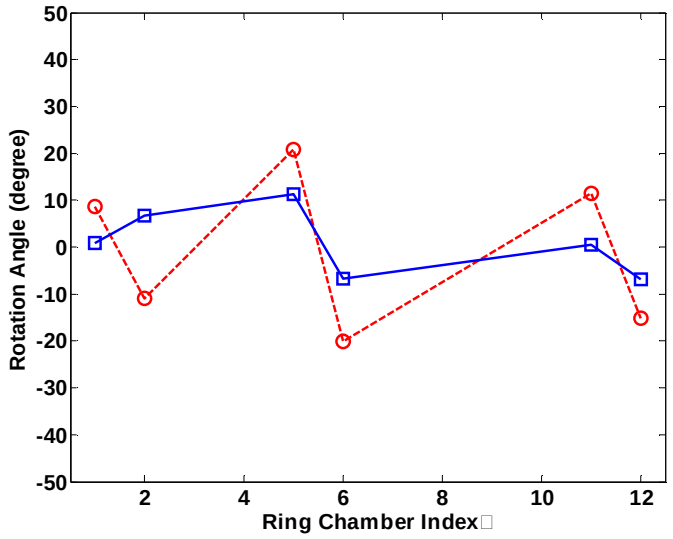

Figure 3.20: Comparison of rotation angle (red) before and (blue) after rotation correction.

I list the matched beam sizes, rotation angle and their average compared with the prediction from Trace3D in Table 3.7. The comparisons of beam sizes for the three cases are plotted in Fig. 3.21 and Fig. 3. 22.

Table 3.7: Match beam parameters in each chamber and their statistics for 6mA beam

Chamber	RC1	RC2	RC5	RC6	RC11	RC12	Ave.	Std.	Trace3D
$2*X_{rms}$(mm)	3.42	3.35	3.39	3.5	3.32	3.41	3.40	0.06	3.49
$2*Y_{rms}$(mm)	2.43	2.54	2.63	2.7	2.66	2.39	2.56	0.13	2.69
Angle(^{o})	0.824	6.71	11.3	-6.7	-0.0	-5.5	1.0	6.9	0.00

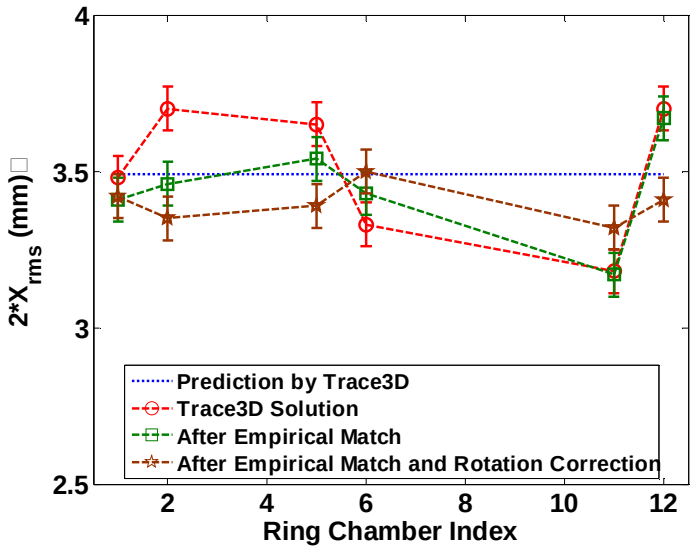

Figure 3.21: Plot of $2*X_{rms}$ of 6 mA beam in each chamber with 3 cases in Fig. 3.19 compared with Trace3D prediction.

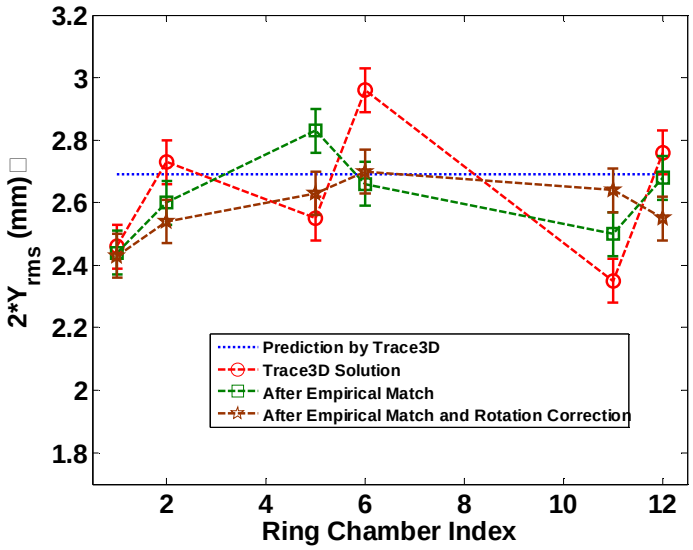

Figure 3.22: Plot of 2*X_{rms} of 6 mA beam in each chamber with 3 cases in Fig. 3.19 compared with Trace3D prediction

Then I use tomography to reconstruct the beam phase space in x-x'. Since there will be four ring quadrupole involved for the phase space tomography in each screen, if one want to get phase space plot for RC1, he need to use QR1, which is not well modeled and might bring ambiguity to the reconstruction process. Therefore, I will not present any phase space plot in RC1. The phase space of other 5 chamber is shown in Fig. 23. Comparing the phase space images proceeding from RC2 to RC12, one can see there is minimum halo and the shape of beam in x-x' space is only slightly changed in these periodic locations. The beam mostly keeps a uniform distribution as indicated by the theory of space charge dominated beam.

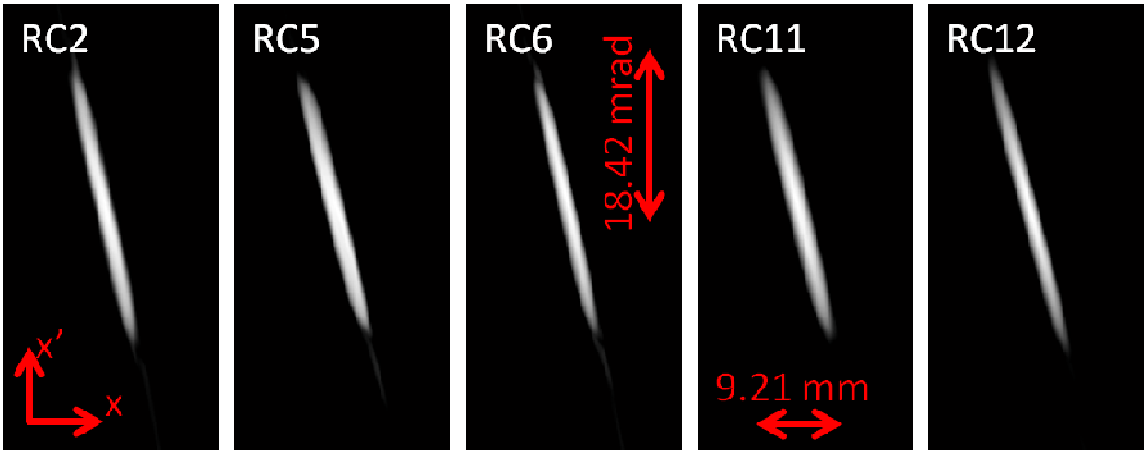

Figure 3.23: Phase space plot (x-x') of matched beam in screen RC2-RC5.

The data are analyzed in a way that one can take a threshold to filter out the artifact that is introduced by the reconstruct algorithm. The threshold is chosen to match the beam sizes from phase space with previous results I measured from configuration space of the beam images in all the chambers. The results are listed in Table 3.8. The average and standard derivation of $2*X'_{rms}$ is 13.54 mrad and 1.03 mrad, and those of the effective emittance in x direction is 13.74 μm and 0.87 μm, which is in the range of the prediction of a matched beam from Trace3D simulation. In this sense, I obtain the match of the 6 mA beam for the first turn. One can see that the beam still experience a small emittance growth which might due to other non-perfection in the ring.

Table 3.8: Phase space measurement of beam parameters for 6mA beam

	Trace3D	RC2	RC5	RC6	RC11	RC12
$2*X_{rms}$ (mm)	3.49	3.35	3.39	3.50	3.32	3.41
$2*X'_{rms}$ (mm)	12.86	14.60	13.00	15.10	12.8	12.9
Effective emittance (μm)	13.00	13.90	12.91	13.42	13.893	15.29

3.7 Transverse beam matching for 21mA beam and 80 mA

Followed by the discussion of 6mA beam, it is naturally to look at a beam with higher currents or higher space charge effects. The next apertures I use here are the 21 mA beam and 80 mA. Again, I start with the initial condition I got from the solenoid tomography shown in Fig. 3. 24 (21mA) and Fig. 3.25 (80 mA), and the parameters are listed in table 3.9.

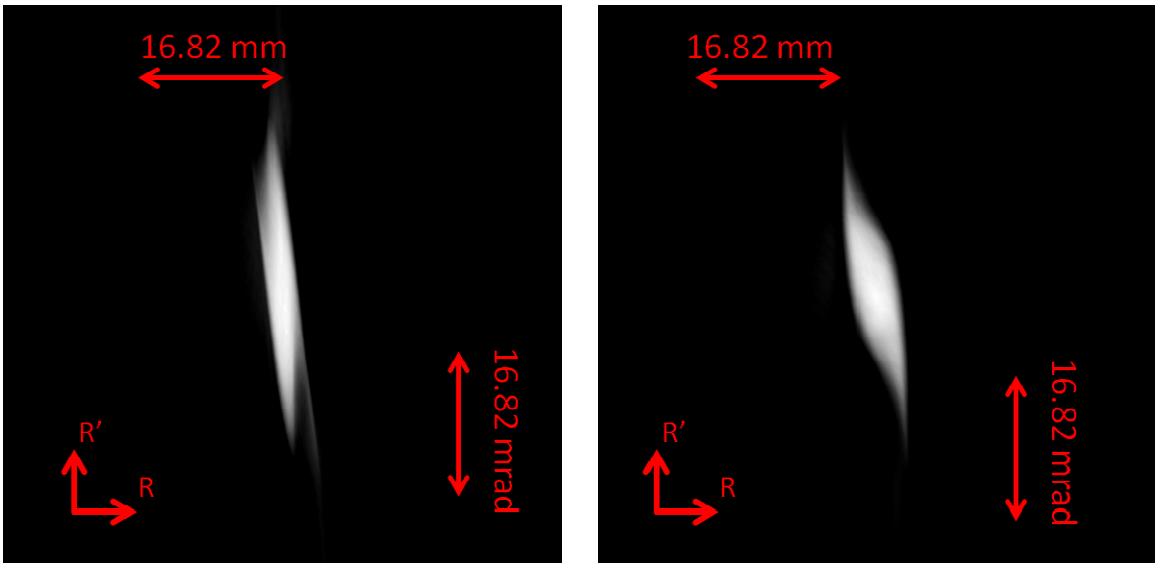

Figure 3.24: x-x' phase space plot of 21 mA beam in aperture (a) and IC1 (b)

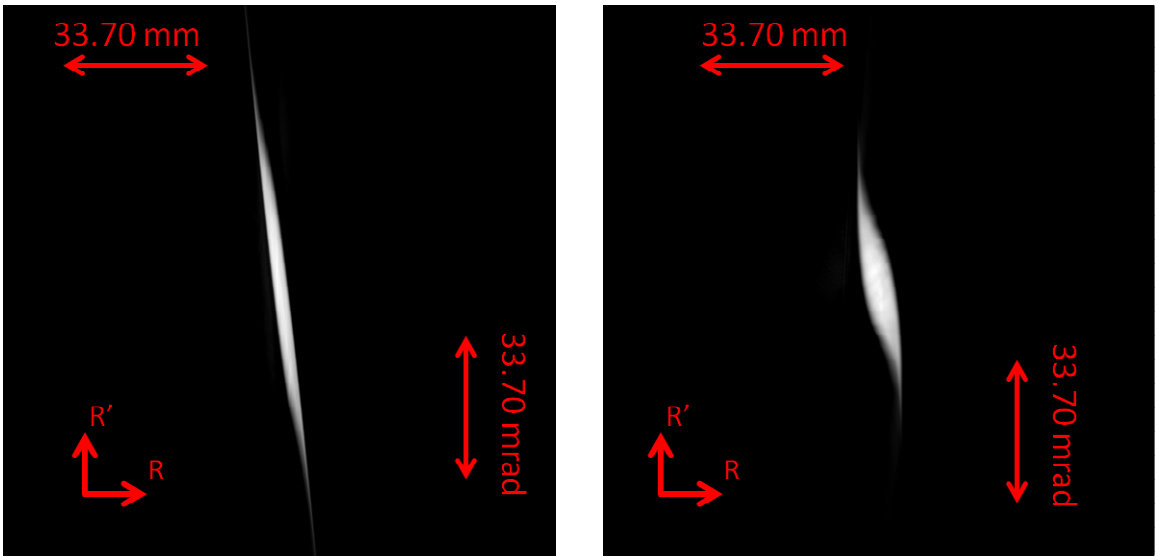

Figure 3.25: x-x' phase space plot of 80 mA beam in aperture (a) and IC1 (b)

Table 3.9: Initial parameters for 21mA and 80 mA beams

Initial envelope values		X (mm)	X' (mrad)	Y(mm)	Y'(mrad)	Emittance(μm)
At aperture	21 mA	2.30	-15.90	2.30	-15.90	29.47
	80 mA	5.50	-40.10	5.50	-40.10	72.42
At IC1	21 mA	3.64	-11.50	3.64	-11.50	29.49
	80 mA	5.37	-21.30	5.37	-21.30	72.73

Trace3D gives the match parameters for both beam in three location of the ring including the mid-plane if ring dipoles, mid-plane of BPMs and the screen, which I listed in Table 3.10. Later, the parameters in screen will be used most.

Table 3.10: Envelopes and slopes in 3 locations for a matched 21 mA and 80 mA beams from Trace3D

Parameter	Mid-plane of ring dipoles		Mid-plane of BPMs		Screen	
	21 mA	80 mA	21 mA	80 mA	21 mA	80 mA
X (mm)	5.62	10.60	5.61	10.57	6.23	11.75
X' (mrad)	20.88	39.21	-21.06	-39.55	-22.85	-42.94
Y (mm)	5.40	10.12	5.33	10.01	4.79	8.98
Y' (mrad)	-20.87	38.94	20.09	37.48	18.23	34.02

Based on the initial parameters from Table 3.10 and matched condition from Table 3.9, I use the fitting module of Trace3D to obtain a match solution for the injection, which is shown in Table 3.11. Notice that the setting for YQ and QR1 are slightly different in both cases comparing with 6 mA beam, which I listed in Table 3.12.

Table 3.11: Magnet location and matching solution for 21mA and 80 mA beams from Trace3D

Magnet		Sol	Q1	Q2	Q3	Q4	Q5	Q6
Position (cm)		17.13	40.53	53.73	72.73	92.33	106.63	122.63
21 mA	Gradient (G/cm)	98.10	3.93	7.17	7.51	6.97	5.43	4.51
	Current (A)	5.5	1.090	1.990	2.075	1.934	1.507	1.251
80 mA	Gradient (G/cm)	103.42	4.33	9.01	7.61	6.94	6.06	6.86
	Current (A)	5.8	1.200	2.499	2.108	1.923	1.680	1.900

Table 3.12: YQ and QR1 settings for 21 mA and 80 mA beams

Magnet	YQ	QR1
21 mA	4.643	4.732
80 mA	4.600	4.700

I apply this solution of 21 mA beam in experiment, and the beam images in all the chambers are shown in row (a) of Fig. 3.26. One can see that, with large beam current or higher intensity, there will be nonlinear effect because of space charge. Moreover, since the high current beam have a larger beam size the image charge from the pipe will also bring nonlinearity to the beam when there is a large asymmetry. As a result, the linear space charge model in Trace3D might not be accurate and the experiment will deviate from the prediction from Trace3D more.

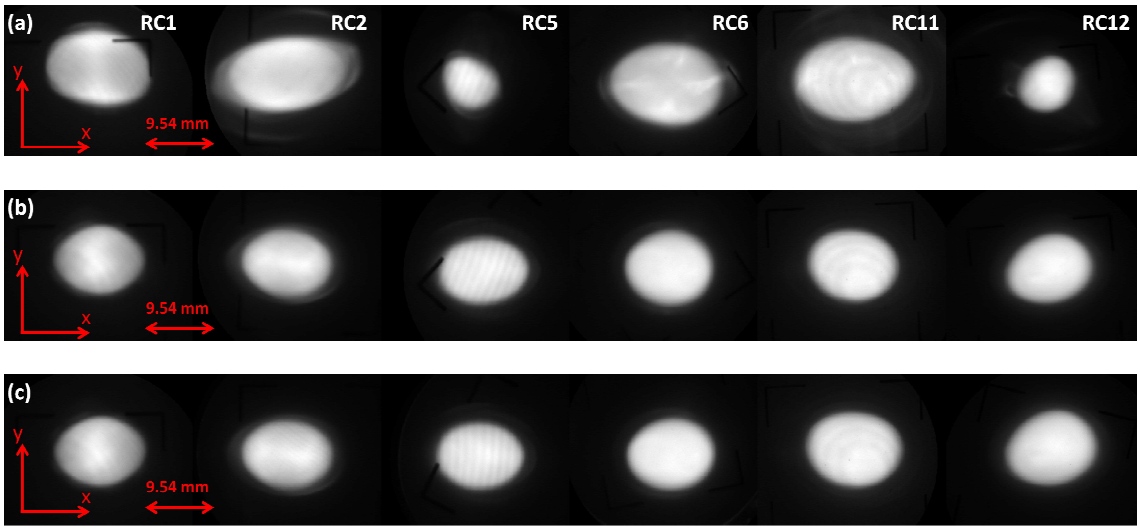

Figure 3.26: Beam images for 21 mA beam in each chamber for (a) solution from Trace3D, (b) after empirical match and (c) after empirical match and rotation correction.

However, the empirical method is still valid. Following the procedure, I perform the empirical match with Q3-Q6 for 21 mA, so that the updated current setting for them will be modified. The result of current setting for Q3-Q6 is shown in Table 3.13. The beam images after empirical matching are shown in row (b) of Fig. 3.26. The row (c) of Fig. 3.26 shows a group of images after a rotation correction as before.

Table 3.13: Magnet settings after empirical match

Magnet	Q3	Q4	Q5	Q6
21 mA	1.690	1.560	1.750	1.670

I list the matched beam sizes, rotation angle and their average for 21 mA beam compared with the prediction from Trace3D in Table 3.13. The comparisons of beam sizes for the three cases are plotted in Fig. 3.27 and Fig. 3. 28. The comparison of rotation angle for latter two cases is plotted in Fig. 3.29 as well.

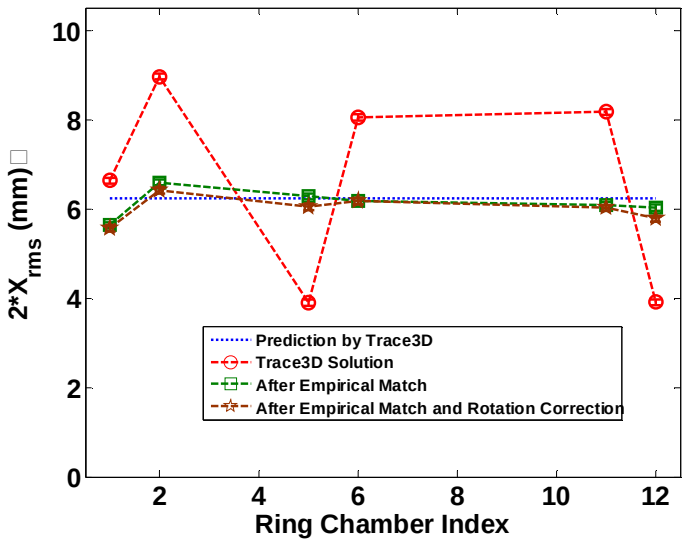

Figure 3.27: Plot of $2*X_{rms}$ of 21 mA beam in each chamber with 3 cases in Fig. 3.26 compared with Trace3D prediction

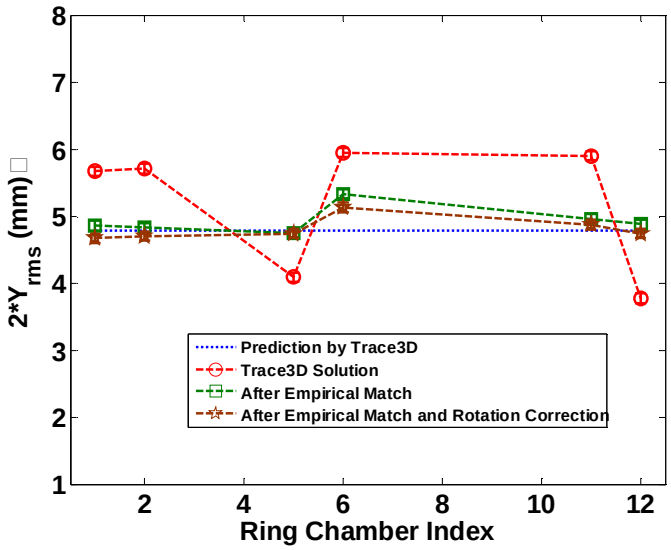

Figure 3.28: Plot of $2*Y_{rms}$ of 21 mA beam in each chamber with 3 cases in Fig. 3.26 compared with Trace3D prediction

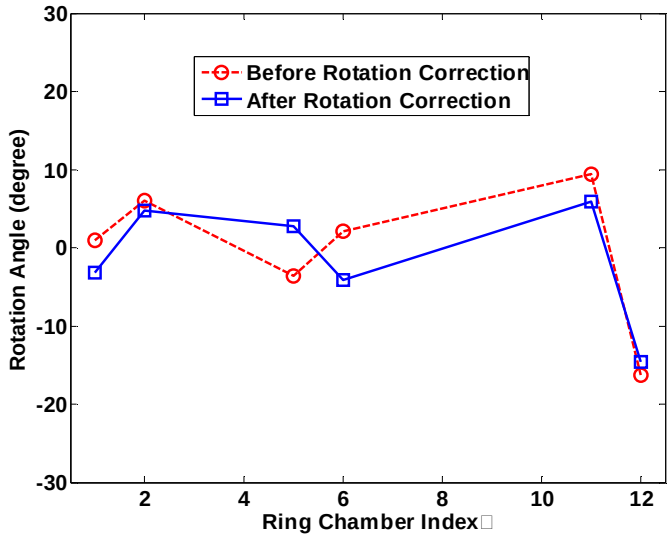

Figure 3.29: Comparison of rotation angle (red) before and (blue) after rotation correction.

Table 3.13: Match beam parameters in each chamber and their statistics (21mA)

Chamber	RC1	RC2	RC5	RC6	RC11	RC12	STD.	Ave.	Trace3D
$2*X_{rms}$(mm)	5.56	6.42	6.05	6.18	6.02	5.78	0.30	6.00	6.23
$2*Y_{rms}$(mm)	4.67	4.7	4.74	5.13	4.87	4.74	0.17	4.81	4.79
Angle(^{o})	-3.2	4.7	2.7	-4.1	5.9	-14.6	-1.42	-1.42	0.00

For even higher current, e.g. 80 mA beam, the beam match is not that simple. First, for such a higher current, the space charge will be much severer than previous two cases. The match solution from Trace3D will be less accuracy or even useless. Second, the beam is large, and the average rms size is about 10 mm, which is about half of the beam pipe. If one does not have a good steering solution or lack of steering dipoles, when he starts from a coarse empirical match, he will expect the beam loss which might affect the efficiency of the method. That usually means a tedious job of several round of empirical match. Third, even after I overcome the beam loss problems, I still face an image force issue because of the betatron motion and envelope oscillation. Last, notice the screen radius is only 15.875 mm, which is less than 1.5 times of x rms size of the beam predicted by Trace3D, how to choose a scan range to do the empirical match is also challenging.

Since there is no good steering solution for this beam, I need to fine adjust the horizontal or vertical dipoles to allow most of the beam come through. Then, instead of a coarse empirical match, I adjust the injection from the Trace3D manually and check the images screen by screen until they are close to the predicted sizes. Finally, a fine empirical match is performed by scan the injection quadrupole Q2-Q5 in a small range about 0.03 A per step for 7 steps each quadrupole. In this way, the beam can be confined

in the screen and beam loss will be ignored. The best match of 80 mA beam I can achieve for the first turn is shown in Fig. 3.30. The beam is very bright for this case so that the fiducial mark can be seen very easily. Since the fiducial mark is transparent plastic foil set behind the screen, there might be gaps between them to form the diffraction pattern shown as the ring structure on the beam. As one can see, the beam is mostly occupied the whole screen, and a clear indication of image force is the irregular shape of the beam even though the RMS size is matched. The matched size is listed in Table 3.14.

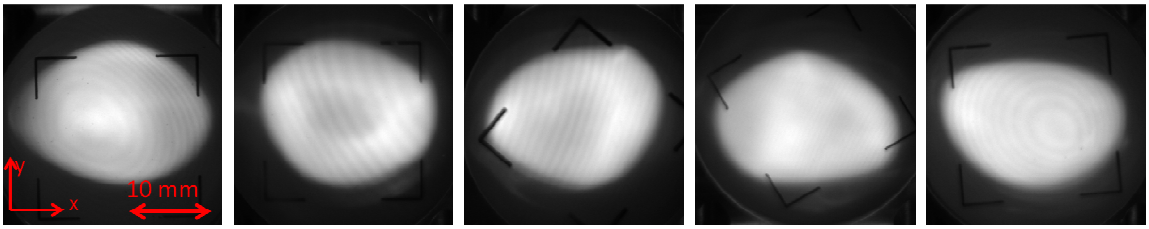

Figure 3.30: Matched beam images in screens for 80 mA beam

Table 3.14: Match beam parameters in each chamber and their statistics (80mA)

Chamber	RC1	RC2	RC5	RC6	RC11	STD.	Ave.	Trace3D
2*Xrms(mm)	10.5	11.1	10.9	11.2	11.4	0.34	11.02	11.75
2*Yrms(mm)	8.46	8.58	8.48	8.31	8.05	0.21	8.38	8.98
Angle(o)	2.7	9.0	-12.1	4.6	8.2	8.6	2.5	0.0

3.8 Chapter conclusion

In this chapter, I start with the discussion of envelope match in space charge dominated beam. Then I solve an Eddy current problem of pulsed magnets which puzzled us for years to obtain a beam match. By using Trace3D as a match tool, I can find a

coarse match solution of the beam in RMS sense. Empirical method allows us do a fine adjustment of that match solution. Later, rotation correction avoids the possibility of halo formation from beam rotation. I apply this method to three of UMER beams with different space charge level, and I find a good match for these cases. The halo is greatly reduced, which allow us to continue with the follow mismatch experiment to study the mechanism of halo formation.

Chapter 4: Major sources for halo formation in UMER

4. 1 Mismatch and halo formation

From the matched 6 mA beam (before I correct the beam rotation) described in chapter 3, I mismatch the beam simple by reduce one of the quadrupole in the injection, e.g., Q5 by 20%, which is a huge error in realistic sense. I compared the beam images between matched and mismatched case in row (a) and row (b) of Fig. 4.1. These images are taken with the Ethernet cameras (GigE Vision Flea3) with gain -5.5 and shutter time 0.3 ms. Here I use a special pseudo-color, which is from low value (black) to medium value (color) and then to high value (black again). In this way, I can show the halos more clear since the quasi-uniform core is not that interesting.

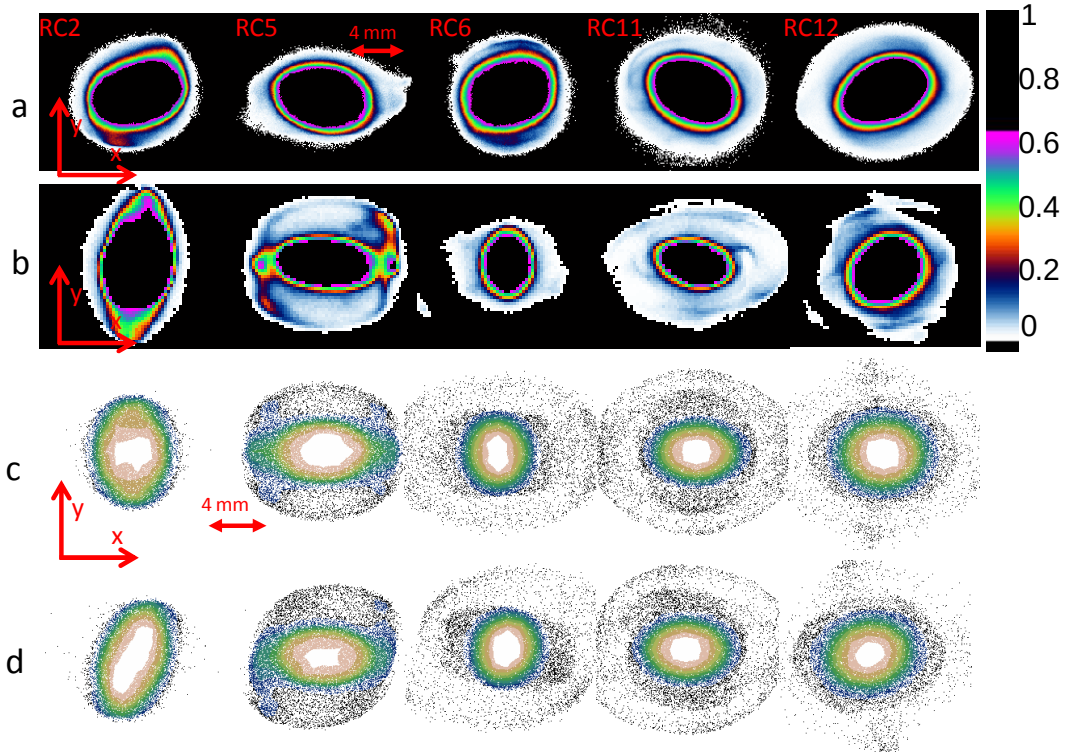

Figure 4.1: Images of 6mA beam in RC2, 5, 11 and 12: (a) matched beam, (b) mismatched beam, (c) simulation of mismatched beam without lattice rotation, and (d) simulation of mismatched beam with lattice rotation. Note the mismatch is generated by reduce one of the injection quadrupole (Q5).

Since the matched beam is not rotation corrected, one can see there is a wobbling of the 'matched' beam, which could also be a source for halo which I will discuss later. From the mismatch beam, the wobbling is also obvious such as the tilted image in RC2, an asymmetry outer ring structure in RC5, and two rotated poles in RC6. When comparing two cases, one can pay attention to the process of halo formation. In the early stage such as in RC2, although I see a bigger mismatch in the y axis than in the x axis, there is no obvious halo and the beam look still quasi-uniform. It can also be seen from the x and y profile in Fig. 4.2 and Fig. 4.3. In the log scale plot, the edge falls off smoothly in x and y axis for both cases, which indicate no halo in this early stage.

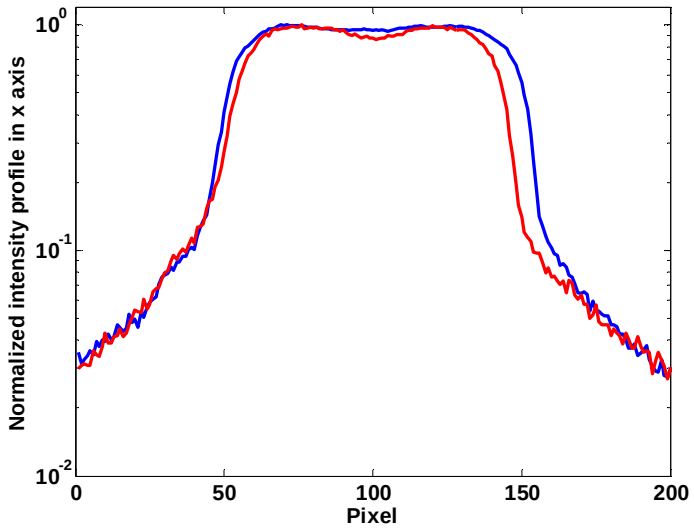

Figure 4.2: Normalized beam profile in x axis of matched (blue) and mismatched (red) 6 mA beam at RC1

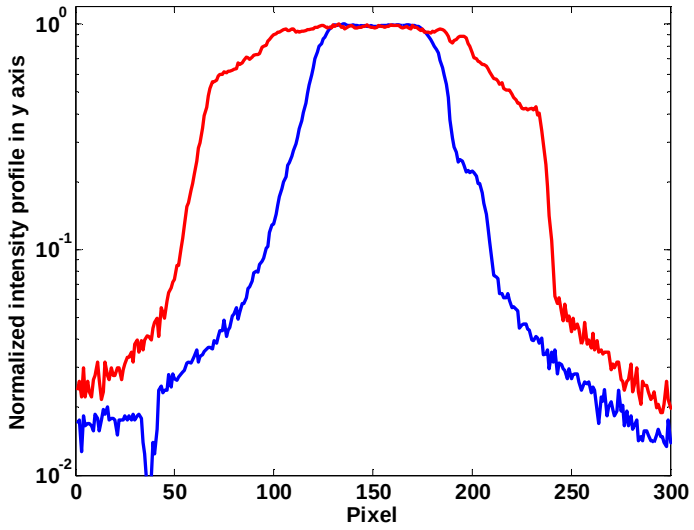

Figure 4.3: Normalized beam profile in y axis of matched (blue) and mismatched (red) 6 mA beam at RC1

When the beam propagates to RC11, after 5 mismatch oscillation (with period λ_m about 1.1 m for breathing mode or 1.3 m for quadrupole mode), there are much more halo generated from mismatched case than the 'matched' case. The profile in x and y axis from central point is shown in Fig. 4.4 and Fig. 4.5. Compared with the smooth tail of the match case, the mismatched one has a second peak or even a third peak outside the beam core edge. This is strong indication of halo formation from the envelope mismatch instead of beam rotation because both cases are suffered from the beam rotation. If looking at the halo structure of the images in RC11 and RC12, the matched beam has a quasi-uniform tail; while the mismatched beam have a more irregular shape of beam halo.

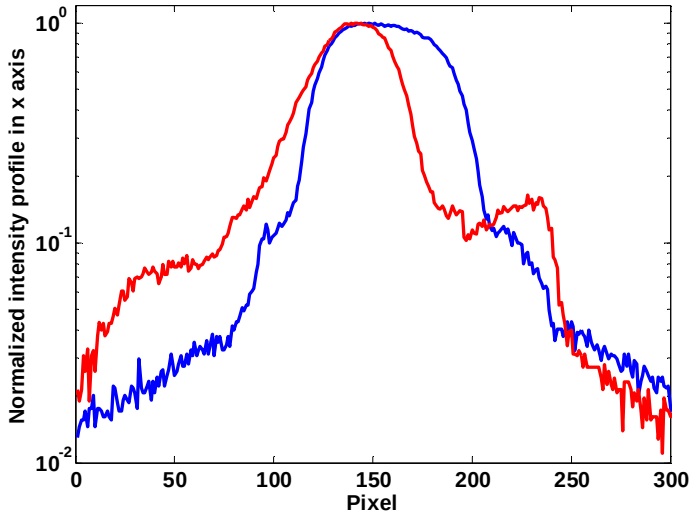

Figure 4.4: Normalized beam profile in x axis of matched (blue) and mismatched (red) 6 mA beam at RC11

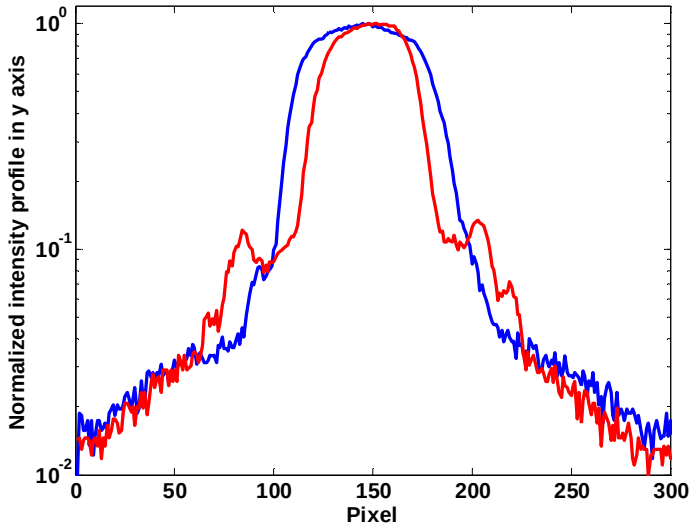

Figure 4.5: Normalized beam profile in y axis of matched (blue) and mismatched (red) 6 mA beam at RC11

In WARP (PIC code) simulation, I see the similar behaviours too. In the simulation, I include the injection, Y-section and ring section. I use 40000 macro particles to simulation the beam. The grids is set to 256×256. Rows (c) and (d) in Fig. 4.1 are simulation from WARP (PIC code). Both of them have the same setting of the mismatched case as in the experiment but without any rotation of the beam. The difference of these two simulations is I set the quadrupole in the ring with a rotation of 10 degree for the latter one to approximately replace the injected beam angle. One can see that although the simulation don't match the experiment perfectly, the characteristic behaviour of beam is reserved in simulation, such as the hot spot structure in RC5, several layers in RC11, and poles structure in RC12. Moreover, when the lattice is rotated, the symmetry is broken. In RC5, two of the hot spot rotate into core and the poles in RC12 not sit in up and down but rotated with an angle just as in the experiment.

I also compare the phase space x-x' plots in the same chambers in Fig. 4.6 from phase space tomography. From the configuration space in Fig. 4.1, it is clear that there are large amount of halo generated due to mismatch. Here, I address three points. First, we don't have a perfect match beam because there is no rotation correction for this matched beam (this is done before I install the new skew quadrupole) and there are halos generated from the rotation, which can be seen from the phase space plot in row (a). Second, from the mismatch beam that I intentionally generate, the beam core first goes through large amplitude oscillation, which can be seen from the slope of the phase space plot from RC2, RC5 and RC6. Third, the associate free energy is transferred to halo particles later and the oscillation amplitude of the core is then reduced.

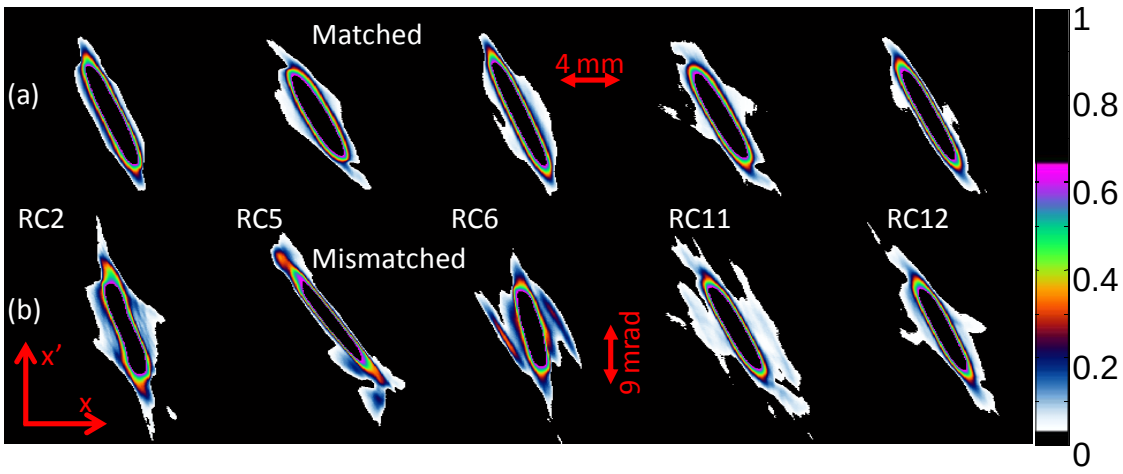

Figure 4.6: Comparison of reconstructed phase space of (a) matched and (b) mismatched 6mA beam

4.2 Injection Quadrupole scan

In order to see the halo clearly, I intentionally increase the camera gain from -5.5 to 0 and shutter time from 0.3 ms to 1 ms. The view point is set at RC12 (about 6 mismatch periods) to allow the halo particle to be exited by mismatch. In this sitting, the beam core region reach beyond the CCD maximum readout and cause saturation of the pixels, and the intensity of beam halo increase dramatically in order for us to have a better view. The drawback for saturating the camera is the blooming and potential damage of the CCD. Based on the matched setting for 6 mA and 21 mA beam, I scan injection quadrupole Q4 and Q5 by steps of 0.1 A. The images are presented in Figs. 4.7-4.10, and the special pseudo-color is also applied here to emphasize the halo outside the beam core.

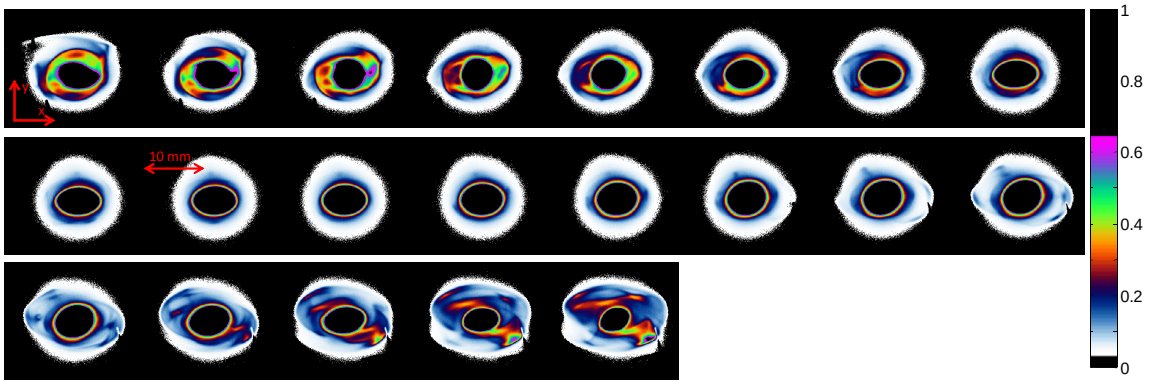

Figure 4.7: Images of 6 mA beam with injection quadrupole Q4 scan.

In Fig. 4.7, I first scan the injection quadrupole Q4 from 0.858 to 2.858 with a step of 0.1 A. As I increase the quadrupole strength, the halo region is first reduced till the beam match at 11th image and then begins to increase. The intensity of the halo is experiencing the same process. At the same time, the beam core goes through the opposite process. It increase first until beam match and then decreased. Notice that, for the first 5 images and last 3 images, there are small beam current losses monitored by an upstream beam current monitor. Even for the case where there is no beam loss, it might still face image forces from beam pipe either due to large asymmetry of beam shape in the injection or due to a non-perfect steering in the ring. Note that the halo distribution is again not regular for small or large Q4 current, again indicating an image force from the conducting pipe.

Similar behaviors can be also observed through Q5 scan. The scan range is from 0.84 A to 2.84 A with a 0.1 A step. The images of Q5 scan are shown in Fig. 4.9.

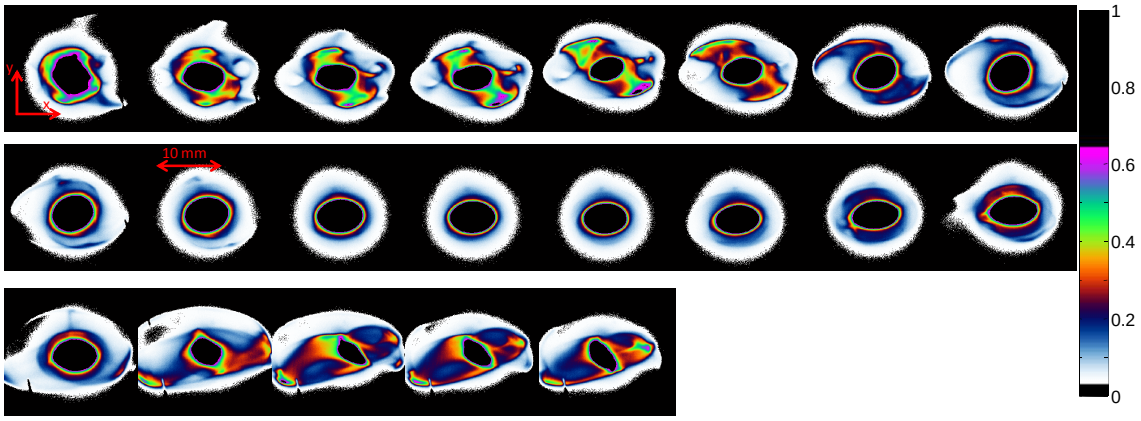

Figure 4.8: Images of 6 mA beam with injection quadrupole Q5 scan

4.3 Beam rotation and halo formation

Beam rotation is also a driving source for halo formation [15]. It is first discovered in simulation by Kishek, but has never been studied through experiment. In order to see the halo generated in first turn, I intentionally introduce a beam rotation by changing the skew quadrupole in the same location as Q6. The beam images of two typical cases compared with zero skew current case are shown in Fig. 7. For row (a), the skew current is set to be 0.4 A, or 144.4 G/m peak gradient. For row (c), the skew current is -0.5 A, or -180.5 G/m peak gradient.

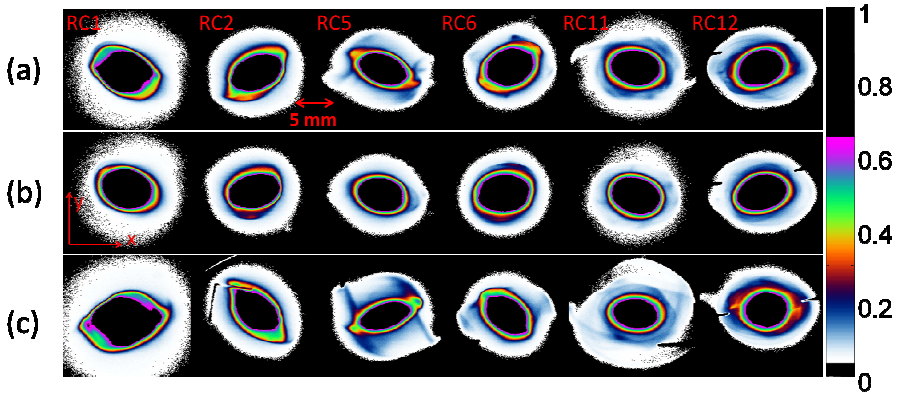

Figure 4.9: Images of 6mA beam with three different initial rotation

It is obvious from images in RC1 to RC5 that there is a wobbling mode related to beam rotation. Since we lack the data between screens, it is hard to say the frequency of the wobbling mode. Essentially, it is a coupled mismatch mode from both transverse directions. When the beam finally gets close to equilibrium state (see in RC11 and RC12), the wobbling energy will be transfer to particles to form halo. The beam rotation angles are calculated using Eqn. 4.1.

$$\alpha = \tan^{-1}\left(\frac{2\Delta xy}{\Delta x^2 + \Delta y^2}\right) \tag{4.1}$$

where α is the rotation angle, and $\Delta ab = \langle ab \rangle - \langle a \rangle \langle b \rangle$. Here operator < > means to average and *a (b*) could be *x* or *y*. The beam rotation angles are also listed in Table 4.1.

Table 4.1: Beam rotation angles at each screen for three ISkew6 settings (6mA)

Chamber	RC1	RC2	RC5	RC6	RC11	RC12
(a)	-11.3	44.5	-22.8	34.6	1.2	1.1
(b)	14.5	-17.9	12.7	-15.9	18.8	-20.8
(c)	22.3	-32.8	23.6	-26.6	7.7	-13.5

As before, I plot the beam profile from the centroid point in x axis and y axis for three cases. The profiles of x and y axis in RC1 are plotted in Fig. 4.10 and Fig. 4.11 and those in RC12 are plotted in Fig. 4.12 and Fig. 4.13. Notice in the beam edge in both x axis and y axis, it is similar to what I discussed in the mismatch section that the beam initially almost don't have any halo and the edge falls smoothly even in the logarithmic scale.

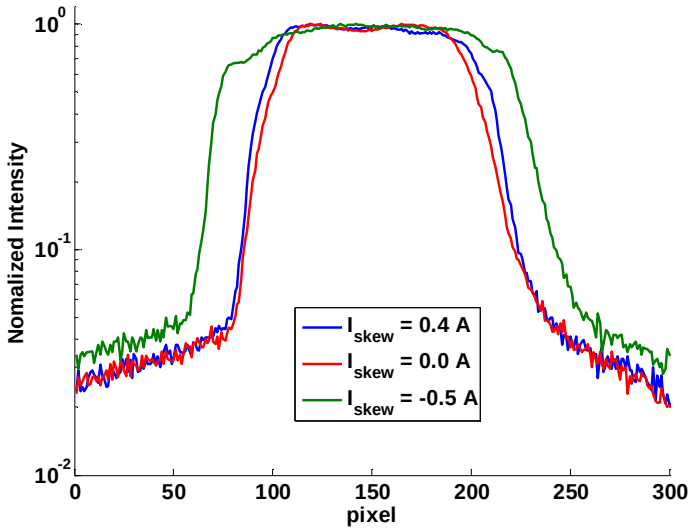

Figure 4.10: Normalized beam profiles in x axis with three setting of Iskew6 at RC1

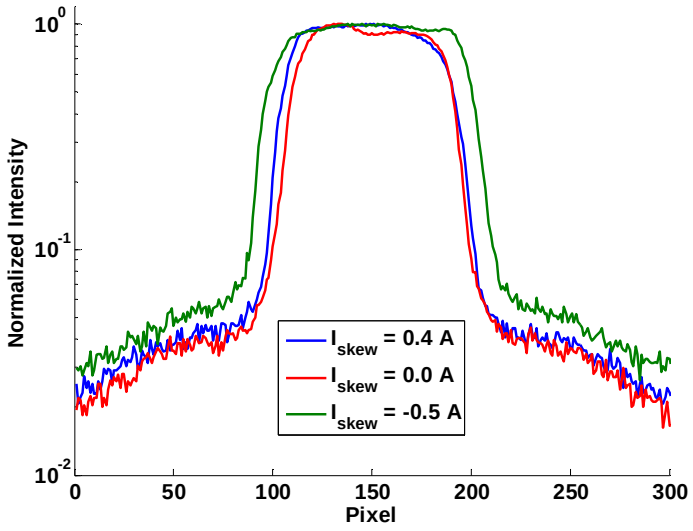

Figure 4.11: Normalized beam profiles in y axis with three setting of Iskew6 at RC1

However, when the beams propagate to RC12, there is halo formation for three cases. The zero skew current is not the optimal but close to it, so one can see a small amount of halo (red curve) generated in both x and y. For other two cases, since I

introduce large rotation amplitudes initially, the associate energy will transfer to beam particle to form halo as the blue and green curve shows especially in the x axis.

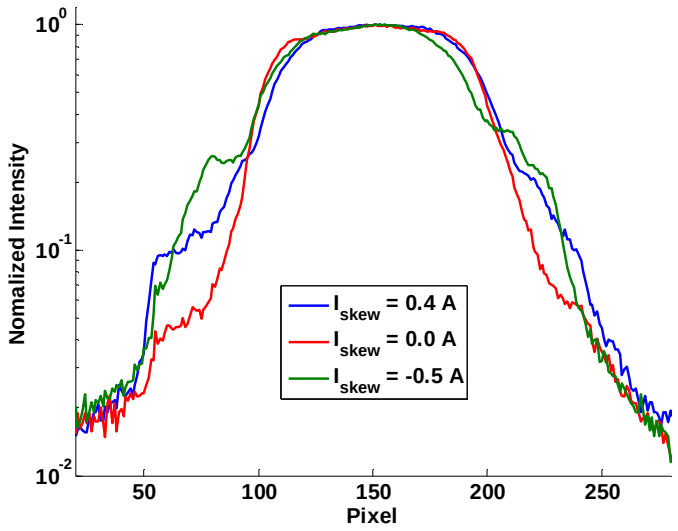

Figure 4.12: Normalized beam profiles in x axis with three setting of Iskew6 at RC12

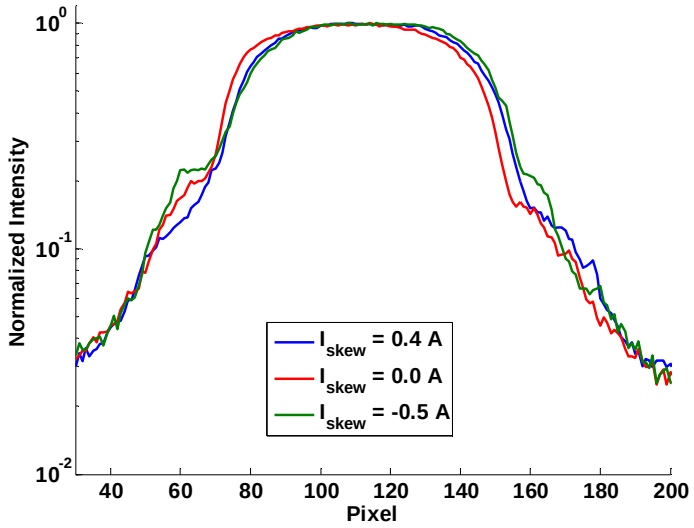

Figure 4.13: Normalized beam profiles in y axis with three setting of Iskew6 at RC12

4.4 Chapter conclusion

In this Chapter, I find out two major sources of halo formation for intense beam in UMER, envelope mismatch and beam rotation. By performing a quadrupole scan, large amount of halo particle can be driven out when the quadrupole strength is far from the one for the matched beam. For the beam rotation case, initial beam rotation will couple both the focus in x and y. I observe a wobbling of the beam rotation, and the energy of beam wobbling will finally relax to the formation of halo. This is the first time in experiment to find out the skewness is also a driving source for halo formation.

Chapter 5: Halo formation in mismatch modes

In the particle core model, mismatch is the key factor to cause halo. To systematic study the halo formation from mismatch, one needs to quantify the mismatch strength by specific envelope mismatch mode and mismatch parameters. In this chapter, I will discuss the basic envelope mismatch mode, particle core model for halo formation and the free energy model for emittance growth. Simulation and experiment are used latter to testify the theories.

5.1 Envelope Mismatch and Mismatch modes

5.1.1 Envelope mismatch mode

In a quadrupole focus channel, the system will have two planes of symmetry as well as the beam. Thus, one needs two equations to describe the beam envelopes and the particle trajectories in each plane. The trajectory equation will be:

$$x'' + \kappa_{x0} x - \frac{2K}{X(X+Y)} x = 0 \tag{5.1}$$

$$y'' + \kappa_{y0} y - \frac{2K}{Y(X+Y)} y = 0 \tag{5.2}$$

Where x, y is the single particle trajectory and $\kappa_{x0}(z)$, $\kappa_{y0}(z)$ are the external focusing functions, and K is the generalized perveance as before, and X, Y is the beam envelope. The beam envelope can be determined as

$$X'' + \kappa_{x0} X - \frac{2K}{X+Y} - \frac{\varepsilon_x^2}{X^3} = 0 \tag{5.3}$$

$$X''+\kappa_{y0}X-\frac{2K}{X+Y}-\frac{\varepsilon_x^2}{X^3}=0 \tag{5.4}$$

From the envelope equations, in a quadrupole channel, even the beam is perfect matched, there will be an envelope oscillation, and the oscillations are transversely coupled. Here, one can assume that $\varepsilon_x = \varepsilon_y = \varepsilon$ and take a mean value of the envelope equation over a period, which is

$$\overline{A}=\frac{1}{S}\int_s^{s+S}A(s)ds \tag{5.5}$$

In this way, the mean value of an matched envelope will be $\overline{X} = \overline{Y} = \overline{R}$, where the mean radius satisfy

$$k_0^2\overline{R}-\frac{K}{\overline{R}}-\frac{\varepsilon^2}{\overline{R}^3}=0 \tag{5.6}$$

Where k_0 is the wave number of the lattice, and k_0^2 replaces the κ_{x0} and κ_{y0} in smooth approximation assumption. Here a space-charge depressed wave number k will also be used, which is defined as

$$k^2=k_0^2-\frac{K}{\overline{R}^2} \tag{5.7}$$

Usually, the ratio between the space charge depressed wave number and the lattice wave number is called tune depression ratio, which is a very important parameter in high intensity beam to describe how much space charge forces are involved in the beam dynamics.

When the mismatch is small, the mean value of envelopes $\overline{X}$ and $\overline{Y}$ will slightly away from the mean radius $\overline{R}$ with perturbations ξ(s) and η(s) separately.

The perturbations in envelopes will result a set of coupled equations as

$$\xi''+\frac{3k_0^2+5k^2}{2}\xi+\frac{k_0^2-k^2}{2}\eta=0 \tag{5.8}$$

$$\eta''+\frac{3k_0^2+5k^2}{2}\eta+\frac{k_0^2-k^2}{2}\xi=0$$

(5.9)

To solve this equation one can get two basic modes. Each mode associate with a wave number k_1 and k_2.

$$k_1^2 = 2k_0^2 + 2k^2 \tag{5.10}$$

$$k_1^2 = k_0^2 + 3k^2 \tag{5.11}$$

Where k_1 is the in phase mode or breathing mode and k_2 is the out of phase mode or quadrupole mode.

5.1.2 Particle core model

From [13, 14], the particle core model depicts the interaction of a simple central charge distribution, or beam core and a single test particle. The core could have an initial mismatch and then introduce an envelope oscillation. The simplest case will be a round continuous beam propagating in a uniform beam transport system with azimuthal symmetry and a linear radial focusing force. As discussed in [7], this could also describe the smoothed or average behavior of a beam in a quadrupole focusing channel. In this case, the envelope equation will be

$$\frac{d^2X}{ds^2} + k_0^2 X - \frac{\varepsilon^2}{R^3} - \frac{K}{R} = 0 \tag{5.12}$$

For a test particle, the trajectory function will be

$$\frac{d^2x}{ds^2} + k_0^2 x - F_{sc} = 0 \tag{5.13}$$

where F_{sc} is the force due to space charge. The particle will face linear space charge force inside the beam envelope while nonlinear space charge force outside as in Eqn. 5.14.

$$F_{sc} = \begin{cases} KX / R^2, |X| < R \\ K / X, |X| \geq R \end{cases} \tag{5.14}$$

If a test particle transit from the edge of the core and pass away, it will be decelerated by the space charge force. Otherwise, it will be accelerated. The net energy gain or loss depends on the contributions from entering core and exiting core process. Usually, for a match beam here, the core radius does not change, so there will be no energy gain or loss. However, with envelope mismatch, there will be an envelope oscillation. Thus, when the test particle enters core with larger radius than the matched beam size and exits core with smaller radius, there will be an energy gain to that particle. This motion is described by Gluckstern as a nonlinear parametric resonance. The resonance occurs when the particle wave number ν is less than half of the wave number of the core mismatch oscillation k_m. Notice that $\nu = k$ (space charge depressed wave number) for particles inside the beam core. When the particles are outside the core, the wave number ν increases as the space charge force decreased. If $\nu > 0.5\, k_c$, the resonant condition cannot be maintained, which will limit further growth of the amplitude. One description of this maximum particle amplitude can be obtained from the Poincaré surface of section plot. Each curve of the plot is taken by following a random picked test particle in phase space trajectory when the beam core radius reaches its minimum. For example, for beam with mismatch parameter $\mu = 6.2$, and tune depression ratio $\eta = 0.5$, the Poincaré surface of section plot is shown as Fig. 5.1. There are three different regions in this plot including a central core in the center, two islands symmetrically located on the x axis representing the parametric resonance trajectories, and a group of quasi-elliptical trajectories outside the core and islands, which hardly play any role with beam core. The

maximum halo radius can be obtained by examining the maximum radius of the particle which is located on the separatrix of the 2:1 resonance island. Wangler describes this maximum particle amplitude by an approximate empirical formula [14] as

$$X_{\max} / a = A + B\left|\ln \mu\right| \tag{5.15}$$

where a is matched core RMS size, A and B are weak functions of the tune depression ratio, and approximated by $A = B = 4$ and μ is the mismatch parameter, which is the ratio of initial mismatch beam size and matched beam size.

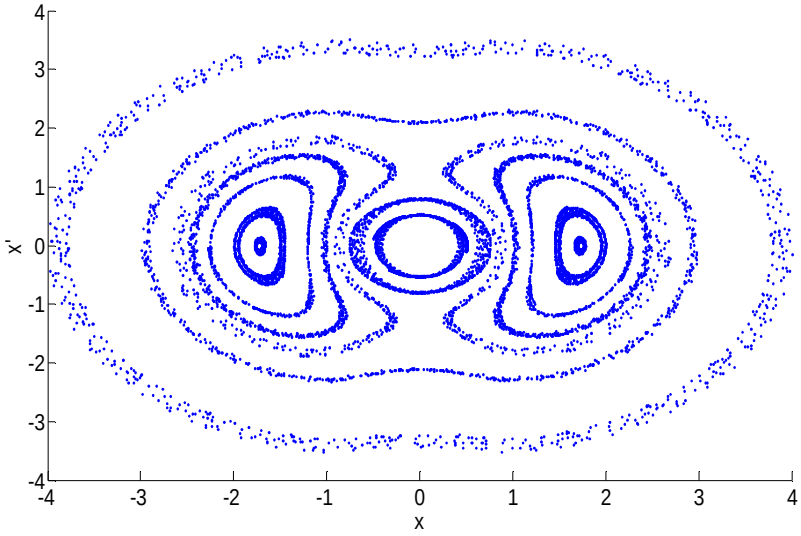

Figure 5.1: Poincaré plot of mismatched beam ($\mu = 0.62,\ \eta = 0.5$)

5.1.3 Free energy model

In [17], the equilibrium state of a continuous beam in a linear periodic focusing system is best described by a transverse Maxwell-Boltzmann distribution with the smooth approximation. Its profile will tend to be uniform in the space-charge dominated regime. Linked to UMER beams, when they are injected into the ring, but not satisfy the stationary state requirement (non-stationary), they will have a higher energy per particle

than that of the corresponding stationary beams. A free energy model is used to describe the result that the energy difference ΔE (free energy) between the non-stationary and the stationary beams can be thermalized to cause beams relax to a stationary state with higher energy per particle. This process will cause emittance growth and it can be analytically calculated.

In this chapter I focus on the case of non-stationary initial beam due to mismatch. The free energy will be in the form

$$\Delta E = \frac{1}{2}\gamma m v^2 k_0^2 a_i^2 h \tag{5.16}$$

where h is the dimensionless free-energy parameter. In the case of mismatch, it can be calculated by

$$h = \frac{1}{2}\frac{k_i^2}{k_0^2}\left(\frac{a_i^2}{a_0^2}-1\right) - \frac{1}{2}\left(1-\frac{a_0^2}{a_i^2}\right) + \left(1-\frac{k_i^2}{k_0^2}\right)\ln\frac{a_i}{a_0} \tag{5.17}$$

where i denotes the initial stationary state, a_i is the initial beam envelope in stationary state or matched beam size, a_0 is the initial mismatched beam envelope and k_i is initial (or matched beam) space charge depressed wave number.

Then the final beam envelope in final stationary state a_f can be calculated using

$$\left(\frac{a_f}{a_i}\right) - 1 - \left(1-\frac{k_i^2}{k_0^2}\right)\ln\frac{a_f}{a_i} = h \tag{5.18}$$

where f denotes the final stationary state. Later, the emittance in final stationary state can be calculated using

$$\frac{\varepsilon_f}{\varepsilon_i} = \frac{a_f}{a_i}\left\{1+\frac{k_0^2}{k_i^2}\left[\left(\frac{a_f}{a_i}\right)^2 - 1\right]\right\}^{1/2} \tag{5.19}$$

5.2 Procedure for generating the pure-mode mismatch[42]

I start from the matched quadrupole setting discussed in previous chapter. I assume that the setting results in a good envelope match at screens in Chamber RC1, RC2,

RC5, RC6, so that the four $X_{\rm rms}$ values are nearly equal and the four $Y_{\rm rms}$ values are nearly equal. Using these values, I obtain the averages of $X_{\rm rms}$ and $Y_{\rm rms}$, as $<X_{\rm rms}>$ and $<Y_{\rm rms}>$. These two values can be a good estimation of the matched RMS sizes at these screens.

Then, I use the Match Type 1 procedure in Trace3D to find the matched x and y alphas and betas at the screen position that give a envelope match over the period from screen in RC1 to that in RC2. Note the emittance I use initially is the value used in Chapter 3, which is from the Solenoid tomography. In this step, the matched sizes from Trace3D will not in general be equal to the measured average values $<X_{\rm rms}>$ and $<Y_{\rm rms}>$. I will use the matched beta values from Trace3D with Eqn. 5.20 to recalculate the transverse emittance $\varepsilon_{x,\rm rms}$ and $\varepsilon_{y,\rm rms}$,

$$\begin{aligned} \varepsilon_{x,rms} &= < X_{rms} >^2 / \beta_x \\ \varepsilon_{y,rms} &= < Y_{rms} >^2 / \beta_y \end{aligned} \tag{5.20}$$

With this new emittance, I can rematch the beam with the Match Type 1 procedure in Trace3D to get advanced beta values. After several iterations, I can get a self-consistent solution with the right average RMS beam size in the screen in RC1 and RC2 while obtaining a match.

The next step is to find the self-consistent initial conditions in aperture with the assumption of no emittance growth. From the self-consistent match solution from previous step, I must run the Trace3D backwards from RC1 to Aperture to get the initial size and slope values. The quadrupoles I used for matching should be set to the match values in Chapter 3 after empirical method. Although the RMS size and slope values in aperture from this procedure in general are different from the ones from solenoid tomography (which is used as the initial condition for matching in Chapter 3), we expect

that the differences are small. The new RMS size and slope values will be used to generate the quadrupole solution for mismatch.

To generate quadrupole solutions that produce a pure-mode mismatch beam, I need to go back to the matched ellipse parameters at a little downstream of the screen in RC1, where *beta functions* (or beam size in the case of same emittance in both transverse axis) are equal. A breathing mode mismatch solution is obtained by scaling α_x, β_x, α_y and β_y at that point by a common factor μ^2, which is the mismatch parameter mentioned previous. From previous aperture condition and lattice settings in Trace3D, I change the setting of the final condition as the parameters modified by mismatch parameter. By using a Type 8 matching procedure, I can find the settings of quadrupole Q2, Q3, Q4, and Q5. In this process, sometimes if I cannot find a setting of this group of quadrupoles with mismatch parameter μ^2 both less than (smaller beam than matched at the screen in RC1) or greater than (lager beam than matched) one, I switch to another group of quadrupoles Q3, Q4, Q5, and Q6. To get the quadrupole mode solutions I must scale α_x and β_x with the mismatch parameter μ^2, and scale α_y and β_y with a different parameter μ_1^2 given by the approximate formula in Eqn. 5.21. The scaling should be performed in the same location as the breathing mode. The quadrupole setting is also found by Trace3D using Type 8 match procedure.

$$\mu_1^2=3.29067 - 4.27792\,\mu^2+2.83012\,\mu^4-1.01391\,\mu^6+0.18356\,\mu^8-0.0130688\,\mu^{10} \qquad (5.21)$$

5.3 Verification of pure mismatch mode using simulation

In order to test the procedure for generating pure mismatch mode, I first use WAPR code to focus on the envelope mismatch mode. To make the case simple, I only use the ring lattice (see Chapter 3). The currents and emittance are the same as measured

by experiment in previous section (5.96 mA, 12.9 mm mrad for 6mA beam and 20.56 mA, 29.5 mm mrad for 21mA beam). In this way, I can avoid the problematic injection and Y-section, and directly obtain a match beam by using a match module called 'Rami_match' embedded in WARP. The idea here is to test if we generate a pure mode envelope mismatch using the scaling procedure at the point when the beta functions of both transverse directions are equal. From the matched solution, this point is located at 284 mm ahead of the first screen for 6 mA beam and 282 mm for 21 mA beam. The matched beam parameters here are shown in Table 5.1. Later I will start our simulation from this point.

Table 5.1 Initial condition for the matched beam (6mA and 21mA) for Warp simulation

Parameter	6 mA	21 mA
$2*X_{\mathrm{rms}}$ (m)	0.002976	0.5261
$2*Y_{\mathrm{rms}}$ (m)	0.02982	0.5263
$2*X'_{\mathrm{rms}}$ (rad)	-0.011369	-0.019859
$2*Y'_{\mathrm{rms}}$ (rad)	0.011400	0.019810

Since the initial mismatch procedure is applied to the twiss parameters, one needs to use Eqn. 5.22 to transform the beam sizes and slopes to twiss parameters. After multiplying the twiss parameters by the according mismatch parameters as indicated in section 5.2, I then transform them back to the sizes and slopes. The initial beam sizes and slopes associated with according mismatch parameters are list in Table 5.2 (5.4) for breathing mode and Table 5.3 (5.5) for quadrupole mode for 6 mA (21 mA) .

$$\begin{aligned} Xrms &= \sqrt{\beta_x * \varepsilon_x} \\ X'rms &= \sqrt{\gamma_x * \varepsilon_x} \\ \beta_x * \gamma_x &= 1 + \alpha_x \end{aligned} \tag{5.22}$$

Table 5.2: Initial conditions for Warp input of the breathing mode (6 mA)

μ	$2*X_{rms}$ (m)	$2*Y_{rms}$ (m)	$2*X'_{rms}$ (m)	$2*Y'_{rms}$ (m)
0.6	0.0017856	0.0017892	-0.00958004	0.009583811
0.7	0.0020832	0.0020874	-0.00961021	0.009622128
0.8	0.0023808	0.0023856	-0.00999931	0.010018405
0.9	0.0026784	0.0026838	-0.01061325	0.010638652
1	0.002976	0.002982	-0.011369	0.0114
1.1	0.0032736	0.0032802	-0.01221556	0.012251642
1.2	0.0035712	0.0035784	-0.0131215	0.013162307
1.3	0.0038688	0.0038766	-0.01406721	0.014112477
1.4	0.0041664	0.0041748	-0.01504018	0.015089716

Table 5.3: Initial conditions for Warp input of the quadrupole mode (6 mA)

μ	μ_1	$2*X_{rms}$ (m)	$2*Y_{rms}$ (m)	$2*X'_{rms}$ (m)	$2*Y'_{rms}$ (m)
0.6	1.439827	0.0017856	0.004293564	-0.00958004	0.015484552
0.7	1.328506	0.0020832	0.003961605	-0.00961021	0.014388707
0.8	1.214751	0.0023808	0.003622389	-0.00999931	0.013300348
0.9	1.103641	0.0026784	0.003291057	-0.01061325	0.012283908
1	0.999726	0.002976	0.002981182	-0.011369	0.011397769
1.1	0.906279	0.0032736	0.002702525	-0.01221556	0.010682967
1.2	0.824523	0.0035712	0.002458729	-0.0131215	0.010153658
1.3	0.753214	0.0038688	0.002246085	-0.01406721	0.009798427
1.4	0.689058	0.0041664	0.002054772	-0.01504018	0.009597448

Table 5.4: Initial conditions for Warp input of the breathing mode (21 mA)

μ	$2*X_{rms}$ (m)	$2*Y_{rms}$ (m)	$2*X'_{rms}$ (m)	$2*Y'_{rms}$ (m)
0.6	0.0031566	0.0031578	-0.01476469	0.014739014
0.7	0.0036827	0.0036841	-0.01555656	0.015524725
0.8	0.0042088	0.0042104	-0.01677523	0.016737447
0.9	0.0047349	0.0047367	-0.01824272	0.018199238
1	0.005261	0.005263	-0.019859	0.01981
1.1	0.0057871	0.0057893	-0.02156711	0.021512722
1.2	0.0063132	0.0063156	-0.02333378	0.02327411
1.3	0.0068393	0.0068419	-0.02513901	0.025074115
1.4	0.0073654	0.0073682	-0.02697036	0.026900282

Table 5.5: Initial conditions for Warp input of the quadrupole mode (21 mA)

μ	μ_1	$2*X_{rms}$ (m)	$2*Y_{rms}$ (m)	$2*X'_{rms}$ (m)	$2*Y'_{rms}$ (m)
0.6	1.439827	0.0031566	0.007577809	-0.01476469	0.027632994
0.7	1.328506	0.0036827	0.006991927	-0.01555656	0.025592429
0.8	1.214751	0.0042088	0.006393237	-0.01677523	0.023537572
0.9	1.103641	0.0047349	0.005808461	-0.01824272	0.021575973
1	0.999726	0.005261	0.005261556	-0.019859	0.019805434
1.1	0.906279	0.0057871	0.004769748	-0.02156711	0.018296758
1.2	0.824523	0.0063132	0.004339467	-0.02333378	0.017077703
1.3	0.753214	0.0068393	0.003964167	-0.02513901	0.016130576
1.4	0.689058	0.0073654	0.003626513	-0.02697036	0.015413713

In the simulation, I use a 256×256 grid for the Poisson solver, a step size of 4 mm along z, and 5,000 particles. The initial distribution is semi-Gaussian based on RMS value mention above. The reason for using fewer particles and large step size here is to quickly access the envelope mismatch while including the nonlinear space charge force, image charge force and emittance growth. Running a large number of test simulations with more particles or higher resolution resulted in no perceptible difference in the final result of envelope oscillations. In order to get enough sampling point for FFT analysis, I run the particles through 400 lattice period. To get the FFT analysis of the mismatch mode and avoid the interference from the dominated oscillation from FODO lattice, I choose the sampling frequency as one sample per lattice period. The final results of FFT analysis plots for each case of 6 mA beam are shown in Fig. 5.2 (breathing mode) and Fig. 5.3 (quadrupole mode).

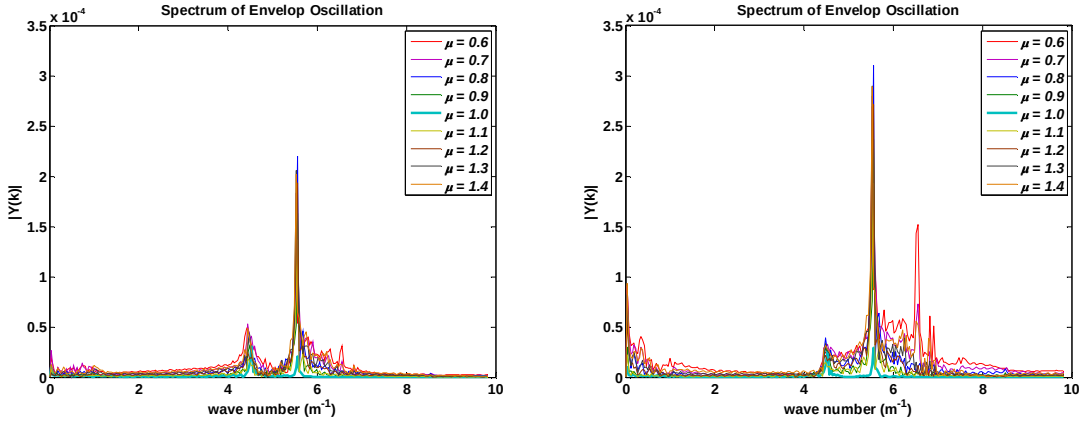

(a) (b)

Figure 5.2: FFT analysis of envelope from the breathing mode for 6 mA (left: x-axis; right: y-axis).

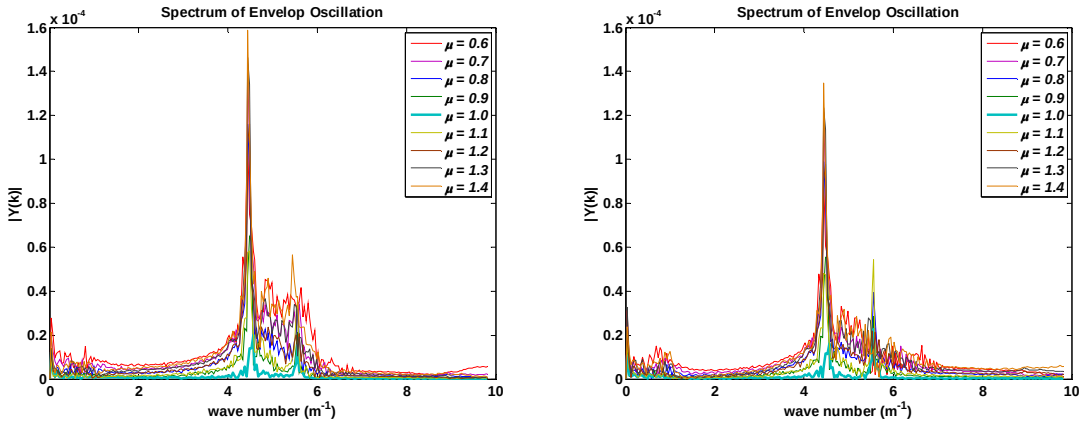

(a) (b)

Figure 5.3: FFT analysis of envelope from the quadrupole mode for 6 mA (left: x-axis; right: y-axis).

From Fig. 5.2, there is a strong indication of a dominated breathing mode both in x or y direction because of the high peaks shown in the figure. The wave number of the high peak is 5.522 m^{-1}, which is close to the calculation value 5.649 m^{-1} using analysis discussed in section 5.1.1. Note that, although there is another peak with smaller wave number shown in the plots, the amplitude is small and did not vary much among different mismatch parameters. Later, the wave number is found close to the calculated value of quadrupole mismatch mode, which means that the mode I generate is not that pure and the mismatch have a small portion of quadrupole mismatch. Meanwhile in the quadrupole mismatch case (see Fig. 5.3), the peaks indicate the mismatch wave number is 4.449 m^{-1} (estimated 4.605 by calculation), also testify the much lower frequency of the quadrupole mode than breathing mode. Note that a small portion of breathing mismatch is also presented here. I plot the amplitudes of breathing mode peak from the breathing mode case and that of the quadrupole mode peak in Fig. 5.4. From the figure, the curve shape is similar to the maximum radius of the halo particles shown in [8], which indicate that the

amplitudes of the peaks are associated with the potential energy in that mismatch mode which could be given to particles to form halos. With the same mismatch parameter, the amplitude of the quadrupole mismatch is smaller than that of the breathing mode, which points out that the breathing mode has larger potential energy which can be transfer to halo particles.

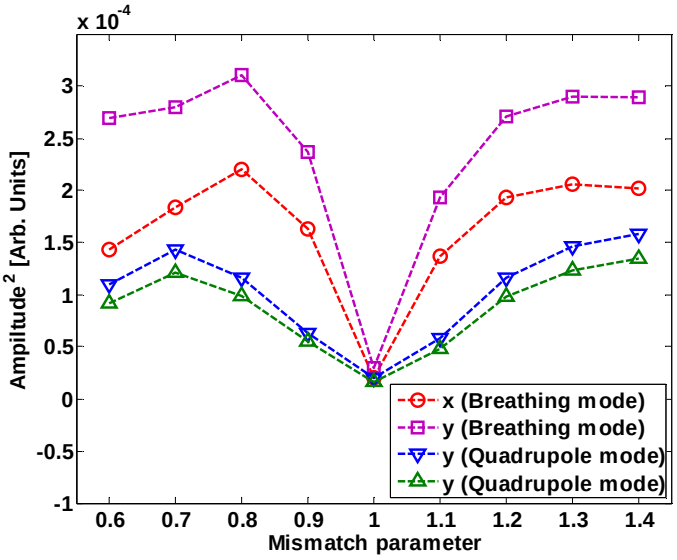

Figure 5.4: Simulated amplitude of the mismatch oscillation versus mismatch parameters for 6mA

For higher current like 21 mA beam, I do the similar PIC simulation with higher beam current and use the same sampling method and FFT analysis to the mismatched envelope for different mismatch parameters and mismatch modes. The plots of the FFT analysis are shown in Fig. 5.5 (breathing mode) and Fig. 5.6 (quadrupole mode). I plot the amplitudes of breathing mode peak from the breathing mode case and that of the quadrupole mode peak in Fig. 5.7.

In the breathing mode case, one can see that the dominated peak with obvious higher amplitude than the 6 mA beam case, but with a peak wave number at 5.369 m^{-1} close to calculated value 5.434 m^{-1}, smaller than that of 6 mA case. This is because that higher beam current has a higher tune depression ratio and the wave number of the mismatch mode is monotone increasing with tune depression ratio. This can be also seen in the case of quadrupole mode mismatch where the peak wave number is 4.180 m^{-1} (estimated 4.199 by calculation). Note that there is also another small peak in the breathing mode case indicating a small portion of quadrupole mode while another small peak in the quadrupole mode case indicating a small portion of breathing mode. Comparing with 6 mA cases, the amplitudes of the secondary peaks in 21 mA cases are much smaller than the dominated mismatch mode. Another point is when the mismatch parameter is as small as 0.6, there is a peak in Fig. 5.3 (b) and Fig. 5.5 (b) at the wave number bigger than characteristic wave number of the breathing mode. It is either due to the strong mismatch, or some numerical artifact which is not been investigated further.

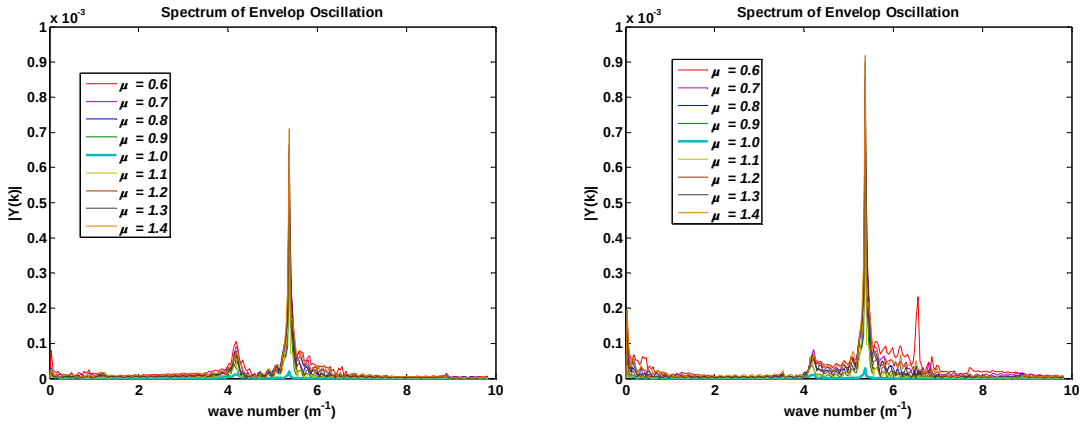

(a) (b)

Figure 5.5: FFT analysis of envelope from the breathing mode for 21 mA (left: x-axis; right: y-axis).

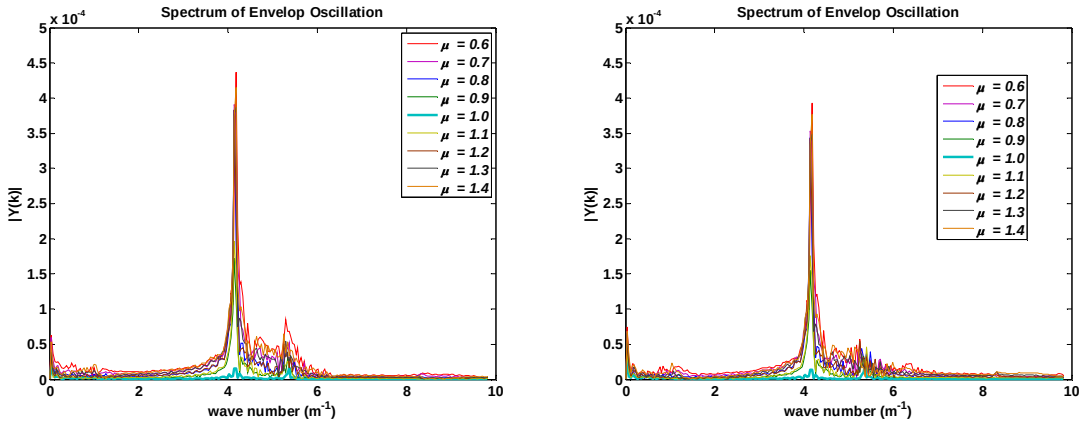

Figure 5.6: FFT analysis of envelope from the quadrupole mode for 21 mA (left: x-axis; right: y-axis).

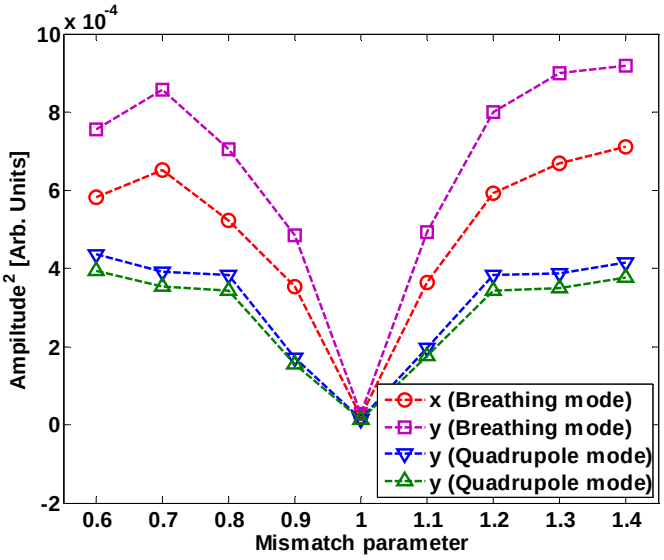

Figure 5.7: Simulated amplitude of the mismatch oscillation versus mismatch parameters for 21 mA

5.4 Maximum extent of halo radius and Emittance growth in simulation

In a real accelerator with large current or intensity, each particle will carry large amount of kinetic energy, especially for ion machine. The loss of beam particle will hit

the pipe and cause the machine to be radio-active. In this section, I will focus on the maximum extent of halo radius, which will help us to better guide the geometric design of future high intensity accelerators to reduce the beam loss due to pipe-particle interaction.

In order to study the maximum extent of halo radius, one must run similar simulation as studying the mismatch mode but with large number of particle to access faint halo. In the simulation, considering the computing power, I use one million particles to best address the halo issue. Further increasing the particle number may improve the accuracy, but the improvement is not so obvious. We showed the comparison of maximum particle radius in x direction with different simulation macro particle number in the Fig. 5.8. This beam is under breathing mode mismatch with mismatch parameter 1.3. There is no difference between the blue (1 million simulation particle) and green curve (4 million), while the purple curve (100 k) is not far away, but the red curve (10 k) is way off.

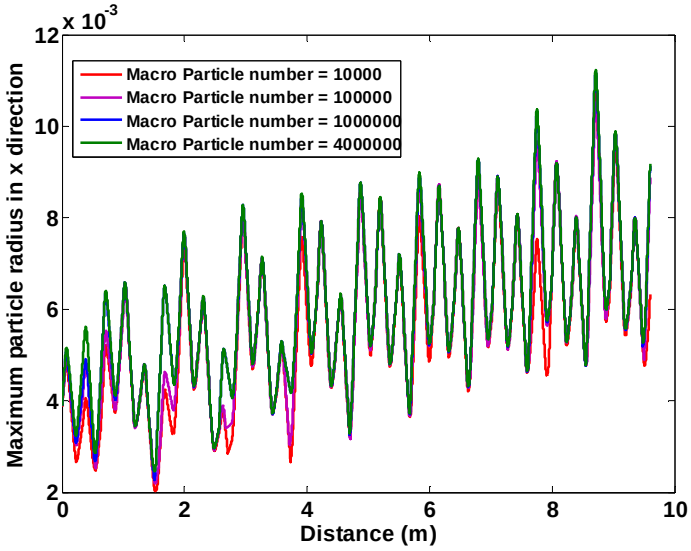

Figure 5.8: Comparison of simulations using different number of macro particles (6 mA).

I also increase the number of grid to 512×512 for field solver and use 0.001 m as the time step. This gives us more accuracy when dealing with the field halo particles face and their trajectories. In each time step, I record the number outside the ellipse with its major and minor radius equal to 2, 3 or 4 time of the RMS beam sizes. This will allow us to estimate the halo particle number in specific range. I am also interested in the maximum radius of a particle can reach, so I trace the boundary of individual particle trajectory and record the largest radius in each step. The beam image in the start, RC1 and RC2 is shown in Fig. 5.9 for breathing mode and Fig. 5.10 for quadrupole mode. It is clear that the beam sizes increase equally with radial symmetry with mismatch parameter increased for the breathing mode in the start while for the quadrupole mode, the beam sizes increase in x axis and decrease in y axis. This behavior is not obvious in the screen location, since the screens are not in the periodic location of the mismatch oscillation.

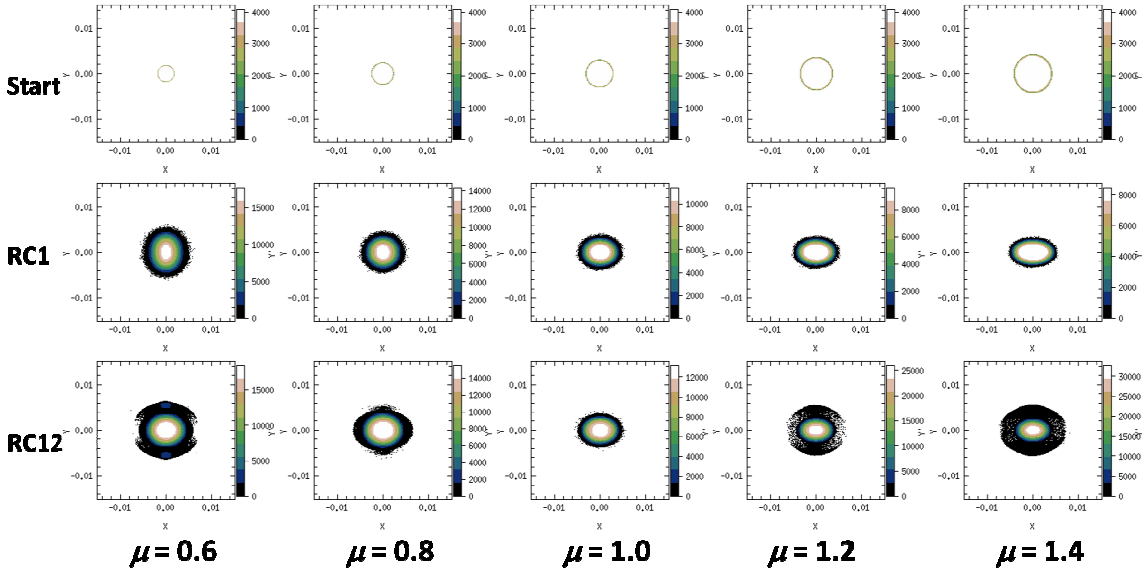

Figure 5.9: Simulated 6mA beam images at start (upper row), RC1 (middle row) and RC12 (lower row) with mismatch parameter from 0.6-1.4 for breathing mode.

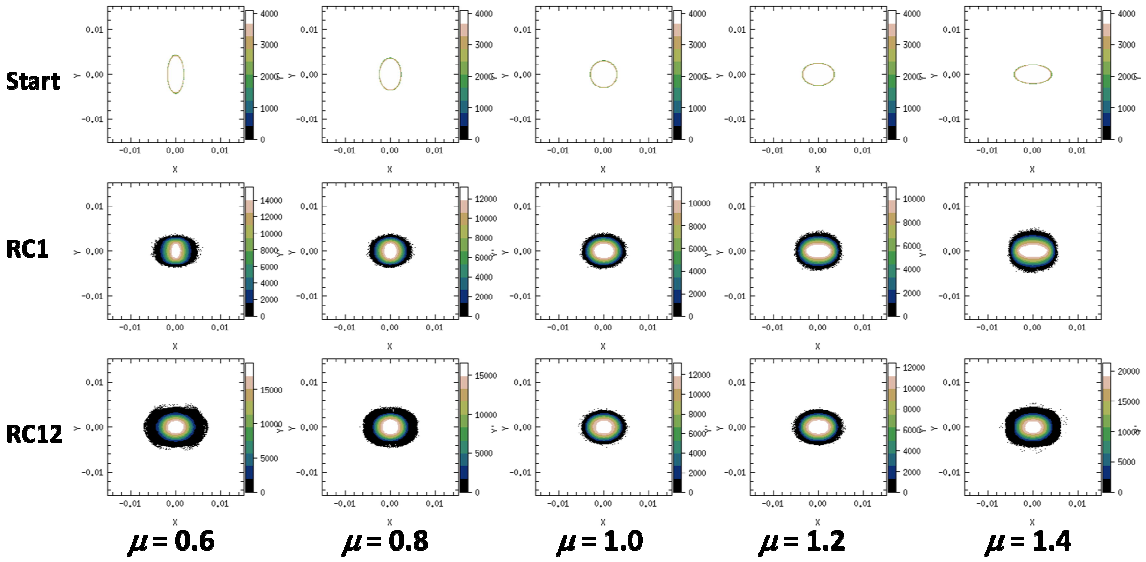

Figure 5.10: Simulated 6mA beam images at start (upper row), RC1 (middle row) and RC12 (lower row) with mismatch parameter from 0.6-1.4 for quadrupole mode.

In fig. 5.11, I illustrate a typical case of halo formation. The mismatch parameter is 0.6, and it plots the ratio of particles outside the 3*RMS beam ellipse. Initially, since I start from a semi-Gaussian distribution. There will be no particle reach beyond the 3*RMS ellipse. But as the beam size continues decrease in x axis, a small portion of halo particles are first driven out. This process continues every time when the beam core reaches its minimum. As one can see in the plot, there is a periodicity for the halo particle driven out, which is close to the mismatch wave period. Since particles feel nonlinear space charge force outside the beam core, they will have different frequency with the particle inside. As the beam propagate through several mismatch period, although halo particles can still oscillate back to core region, but there are more newly formed halo will come out of the beam core. The net number of particles outside 3*RMS ellipse region will stay above zero.

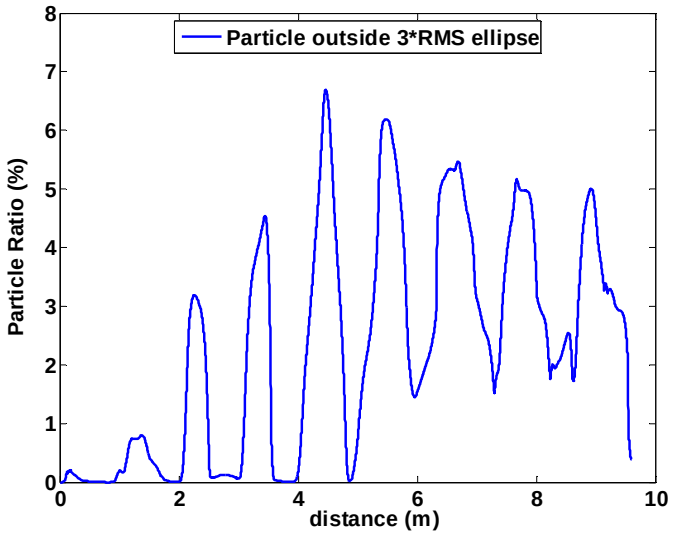

Figure 5.11: Simulated number ratio of particles outside 3*RMS region of 6 mA beam with mismatch parameter μ=0.6 in breathing mode

In Fig. 5.12, I plot the number ratio of particles outside 3*RMS region at screen location of RC12 with different mismatch mode and mismatch parameters. The red solid curve is for the breathing mode and blue dashed curve is for quadrupole mode. For both mode, the minimum of number ration outside the 3*RMS region occurs when the mismatch parameter is unity. When we increase or decrease the mismatch parameter, there is always an increase of particle number in the region outside 3*RMS size. In large value of mismatch parameter, there is more particles outside the 3*RMS region in breathing mode than in quadrupole mode. When close to unity, the difference is not so obvious.

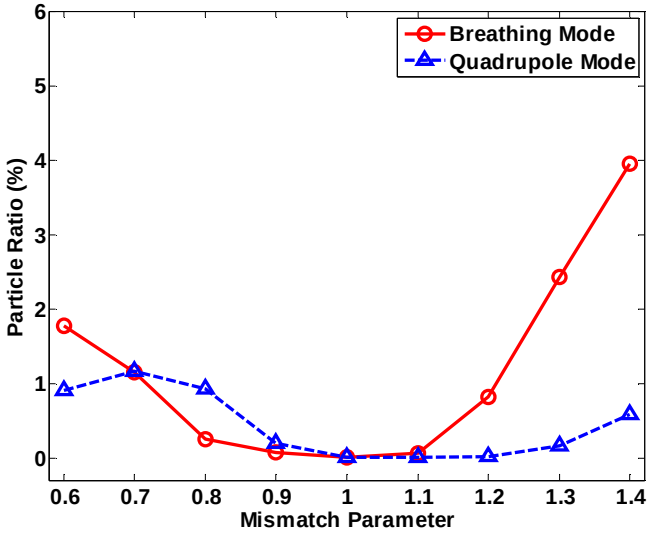

Figure 5.12: Simulated number ratio of particles outside the 3*RMS region of 6 mA beam with different mismatch parameter and different mismatch mode at screen in RC12

In Fig. 5.13, I plot the maximum particle radius divided by the matched RMS size with mismatch parameters from 0.6 to 1.4 in two mismatch mode. The blue solid line is for breathing mode, and the red dashed line is for quadrupole mode. The maximum particle radius is the largest size of individual particles along the way when beam propagate from the ring entrance to RC12, but averaged between x and y axis. In each axis, the largest size is the distance from maximum extent to the minimum extent divided by two. A theory prediction curve from Eqn. 5.15 of maximum particle radius divided by the matched RMS beam size with different mismatch parameter is plot as purple curve in Fig. 5.13. One can see that the shape of the simulation curve is consistent with the curve predicted by particle core model. We see the data for breathing mode mismatch is always larger than that of the quadrupole mode. This could be explained as previous discussion that for the same mismatch parameter, the beams in breathing mode mismatch carry more

free energy than the beams in quadrupole mode mismatch. From the figure, the points of the breathing mode lie below the theory prediction when mismatch is small (close to unity) while for the other large mismatch, points exceed the prediction from the core particle model for larger mismatch. The possible explanation is that, for the small mismatch the particles only go through the mismatch oscillation about 6 periods when reaching to RC12, so the halo particles are not being exited to maximum energy level in order to reach the maximum radius predicted by the theory. For the large mismatch case, there could be other mechanisms which fasten this process, for example, the free energy stored in the initial distribution.

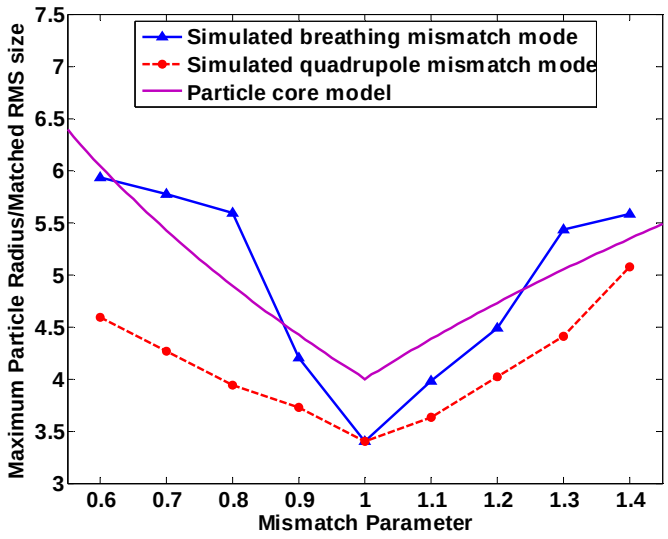

Figure 5.13: Simulated maximum particle radius along the way propagating to RC12 versus mismatch parameter compared with prediction from particle core model.

For a mismatched beam, the beam is not in an equilibrium state, and the associate free energy will cause emittance growth. In Fig. 5.14, the blue curve plot the ratio of the final (at RC12) and initial emittance versus mismatch parameter calculated from the free

energy model with the assumption that the ratio of final radius and initial radius is small (see Eqn. 5.17-5.19). The red, purple, green and light blue dashed curve represent the emittance growth versus the mismatch parameters in x axis, in y axis for breathing mode and for quadrupole mode separately. One can see that the emittance growth in y axis for breathing mode is close to the theory curve for most of the mismatch parameters while the emittance growth in x axis for quadrupole mode approaches the theory in mismatch parameter higher than 1.0. Otherwise, the curves are below the maximum emittance predicted by the theory. In the simulation, for the mismatched case, we always observe anisotropy (x-y differences) for emittance growth, especially for breathing mode, which can be seen also from Fig. 5.14. This result was also found out by Franchetti, Hofmann, and Jeon [43], and they think it is related to the initial x-y tune differences as small as 1%.

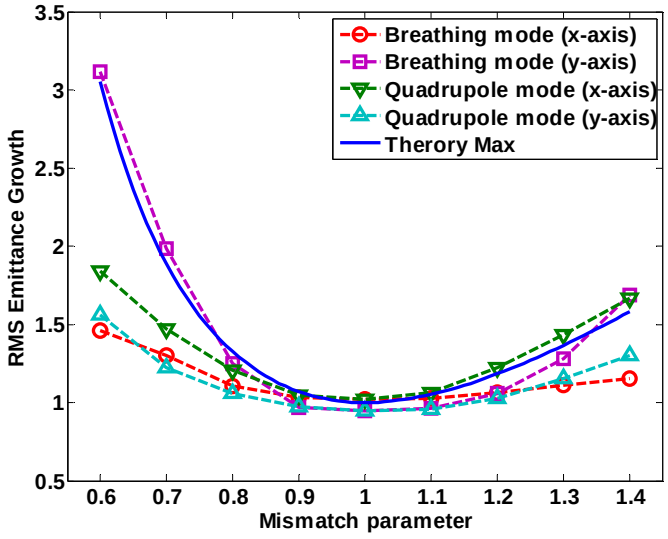

Figure 5.14: Emittance growth verses mismatch parameter at RC12 for 6mA beam. The solid curve shows maximum growth from the free energy model.

Later, I test the halo formation with higher current beam (21 mA) in simulation. The simulation setting is the same except the beam current, initial sizes, slopes and emittance increase accordingly. The beam images at the start, RC1 and RC12 are shown in Fig. 5.15 for breathing mode and Fig. 5.16 for quadrupole mode. With higher currents, the beam size is larger and then the halo from mismatch will oscillate to even bigger radius. Comparing with the curve predicted in particle core model in Fig. 5.17, which is not related to beam current (or tune depression ratio), one can see the similar behaviors as 6mA beam case that the maximum radius for quadrupole mode are smaller than the breathing mode. Most case of maximum radius lies below the prediction curve from particle core model. For larger mismatch (far away from unity), the maximum radius of breathing mode exceed the prediction from the particle core model, which indicate that when we apply this simplified model in design of high intensity accelerators, some margin should be taken into consideration. From the free energy model, the emittance growth is dependent on both the mismatch parameter and the tune depression ratio. With lower tune depression value (higher current), the theory prediction value is higher than the 6 mA case. There is still a large anisotropy for emittance growth. Since the simulated emittance growth is still below the theory curve, the free energy model is still valid in this range of mismatch parameter at least for such a length of beam propagation.

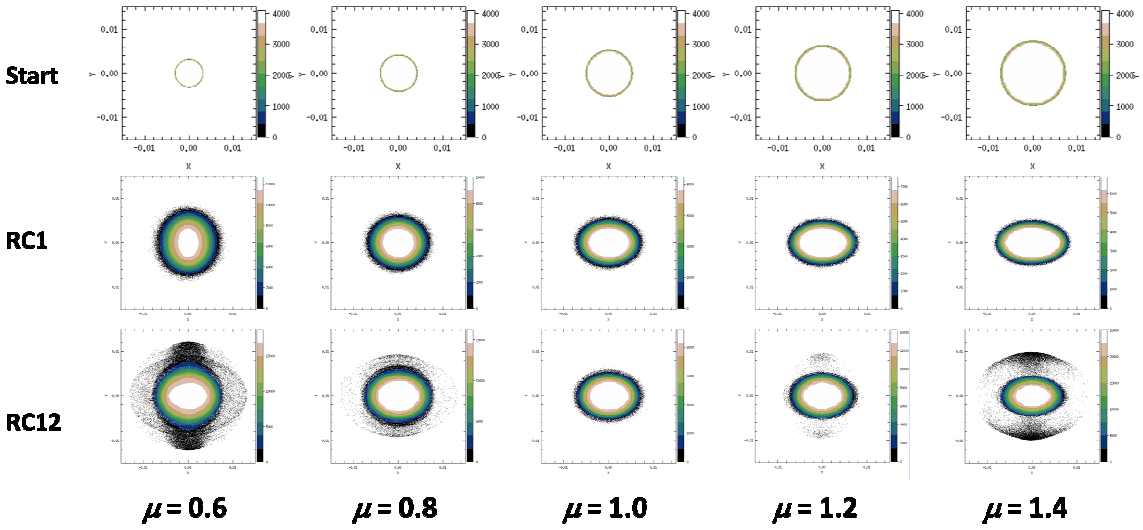

Figure 5.15: Simulated 21mA beam images at start (upper row), RC1 (middle row) and RC12 (lower row) with mismatch parameter from 0.6-1.4 for breathing mode.

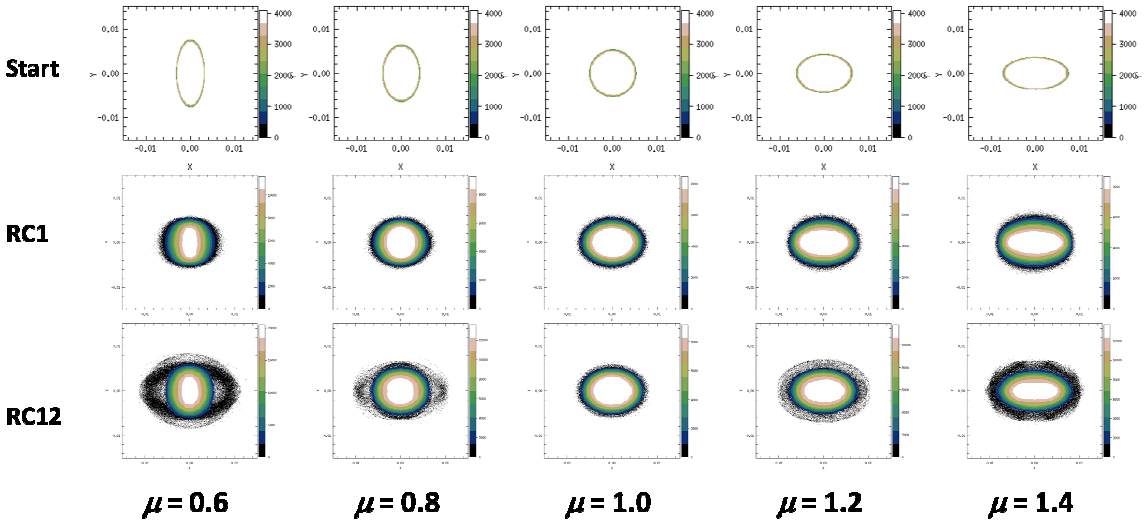

Figure 5.16: Simulated 21mA beam images at start (upper row), RC1 (middle row) and RC12 (lower row) with mismatch parameter from 0.6-1.4 for quadrupole mode.

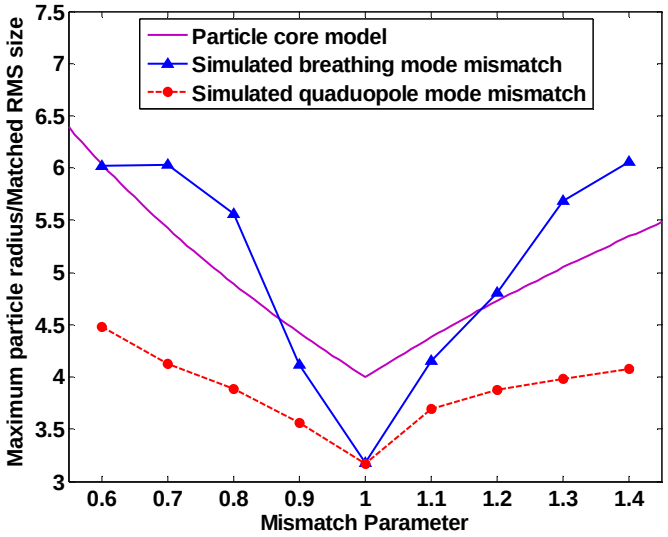

Figure 5.17: Simulated 21mA maximum particle radius along the way propagating to RC12 versus mismatch parameter

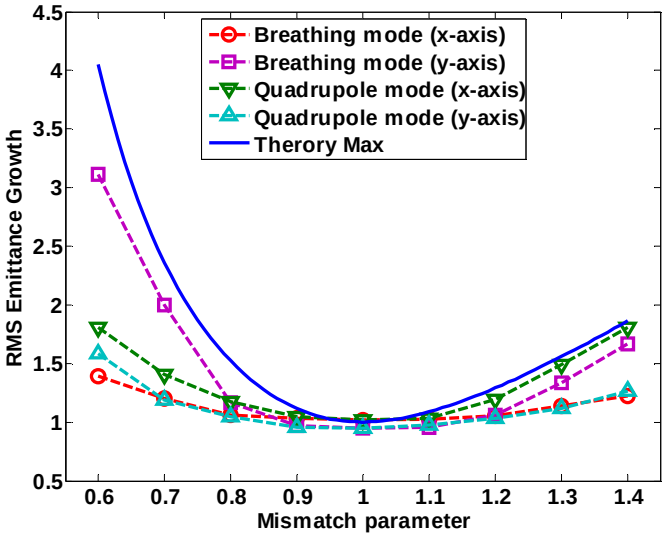

Figure 5.18: Emittance growth verses mismatch parameter at RC12 for 21mA beam. The solid curve shows maximum growth from the free energy model.

5.5 Experiment study of the mismatch mode

In experiment, I follow the procedure in section 5.2 to generate the pure mode envelope mismatch. The settings of the injection quadrupoles Q2-Q5 for 6 mA beam are listed in Table 5.6 for breathing mode and in Table 5.7 for quadrupole mode.

Table 5.6: Setting of injection quadrupoles Q2-Q5 for breathing mode mismatch (6mA)

μ	Q2(A)	Q3(A)	Q4(A)	Q5(A)
0.6	1.819	1.265	1.128	1.794
0.7	1.875	1.427	1.302	1.832
0.8	1.922	1.562	1.475	1.865
0.9	1.961	1.681	1.660	1.900
1	1.992	1.785	1.858	1.940
1.1	2.015	1.876	2.059	1.983
1.2	2.028	1.952	2.243	2.029
1.3	2.030	2.013	2.391	2.076
1.4	2.023	2.062	2.493	2.128

Table 5.7: Setting of injection quadrupoles Q2-Q5 for quadrupole mode mismatch (6mA)

μ	μ_1	Q2(A)	Q3(A)	Q4(A)	Q5(A)
0.6	1.439827	1.930	1.858	1.526	1.561
0.7	1.328506	1.938	1.837	1.622	1.682
0.8	1.214751	1.952	1.816	1.694	1.781
0.9	1.103641	1.970	1.797	1.766	1.865
1	0.999726	1.992	1.785	1.858	1.940
1.1	0.906279	2.015	1.783	1.989	2.012
1.2	0.824523	2.037	1.792	2.170	2.083
1.3	0.753214	2.054	1.806	2.382	2.149
1.4	0.689058	2.212	1.966	3.340	2.315

The beam images are shown in Fig. 5.19 for breathing mode and in Fig. 5.20 for quadrupole mode. For the breathing mode, one can observe a large beam rotation in RC1 when the mismatch parameter is small. As discussed before, the rotation will contribute to the halo formation and cause more halo generation. For the cases that mismatch parameter close to 1.0 (0.9-1.1), the halo formation is relatively slow, which shows the intense beam have certain allowance for envelope mismatch. I compare the envelopes of three typical cases each mode with simulation and plot them in Fig. 5.21 – Fig. 5.25. Note that the red color is for x axis and blue is for y axis. The dashed curves are from the simulation and the markers represent the experiment result. The error comes from the resolution of one pixel. Except few experimental data points are not on the simulation curve, most agree with simulation quite well. Since I already showed the simulation curve is a pure mode mismatch and here I have the agreement, I can claim a close situation of pure mode mismatch in the experiment, which is of course not perfect, but give us a frame to discuss the halo formation in experiment quantitatively.

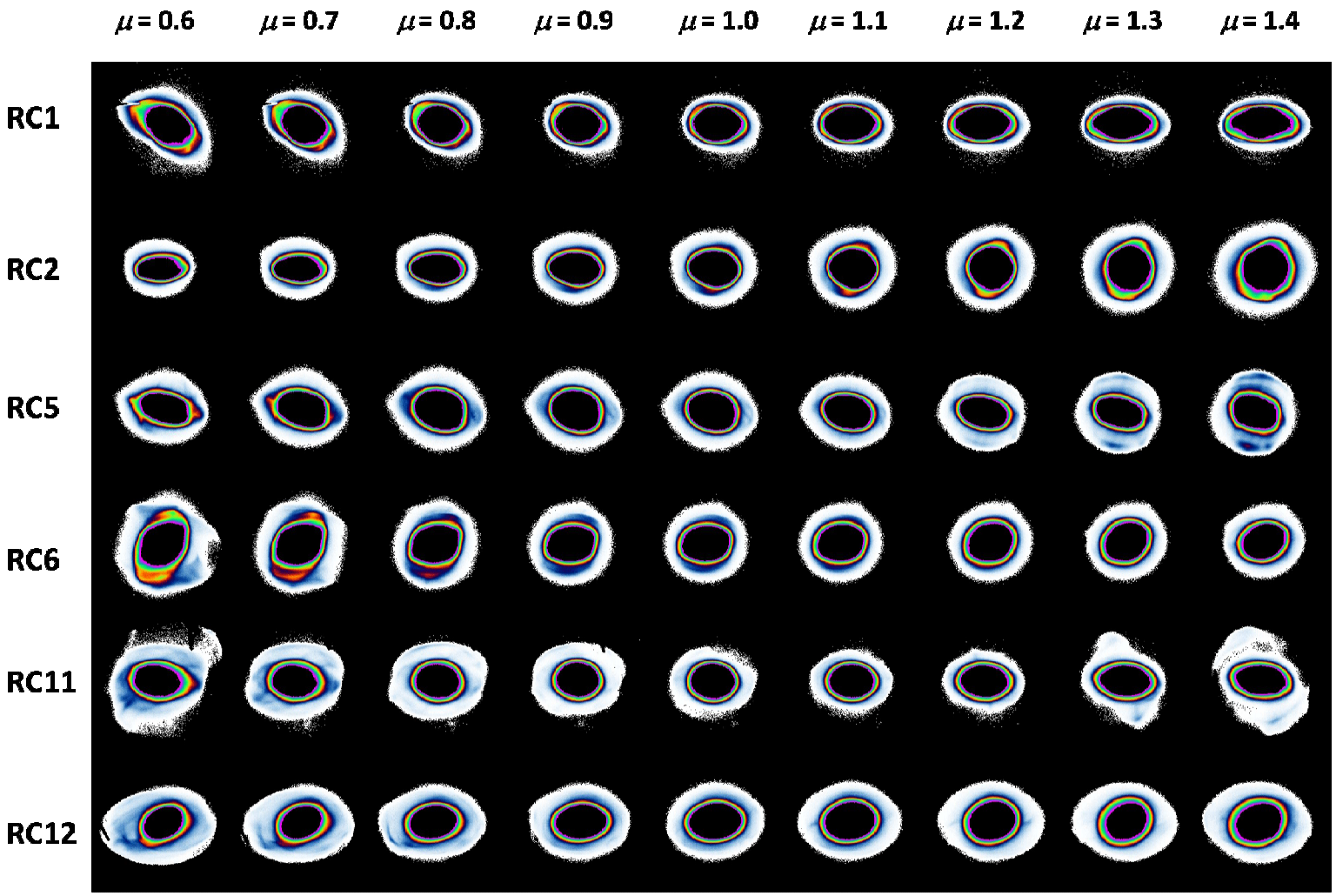

Figure 5.19: Images of 6 mA beam at RC1, 2, 5, 6, 11, 12 with mismatch parameter from 0.6 to 1.4 of breathing mode

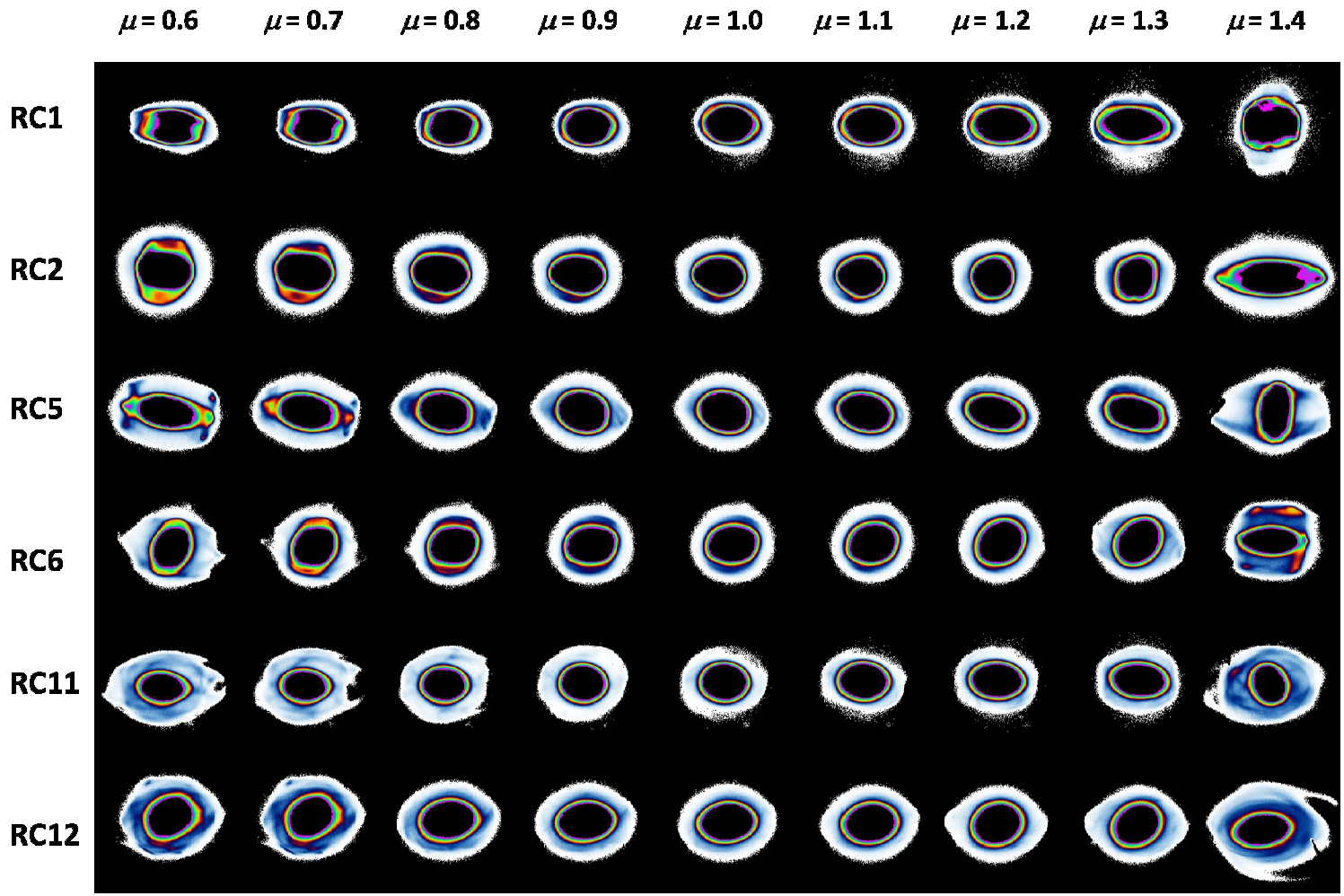

Figure 5.20: Images of 6 mA beam at RC1, 2, 5, 6, 11, 12 with mismatch parameter from 0.6 to 1.4 of quadrupole mode

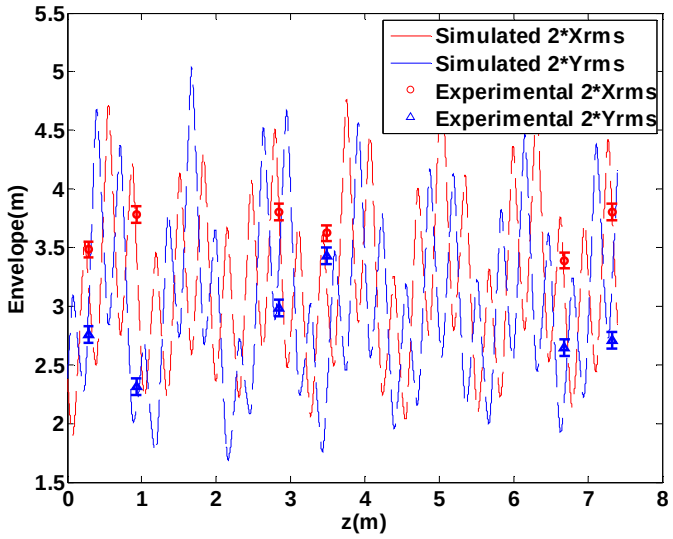

Figure 5.21: Comparison of Envelope between simulation and experimental data for 6mA beam in breathing mode (mismatch parameter μ = 0.8)

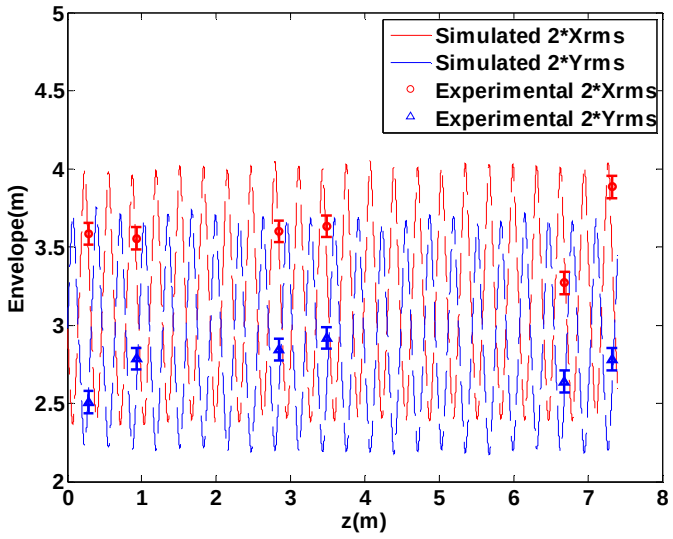

Figure 5.22: Comparison of Envelope between simulation and experimental data for 6mA matched beam (mismatch parameter μ = 1.0)

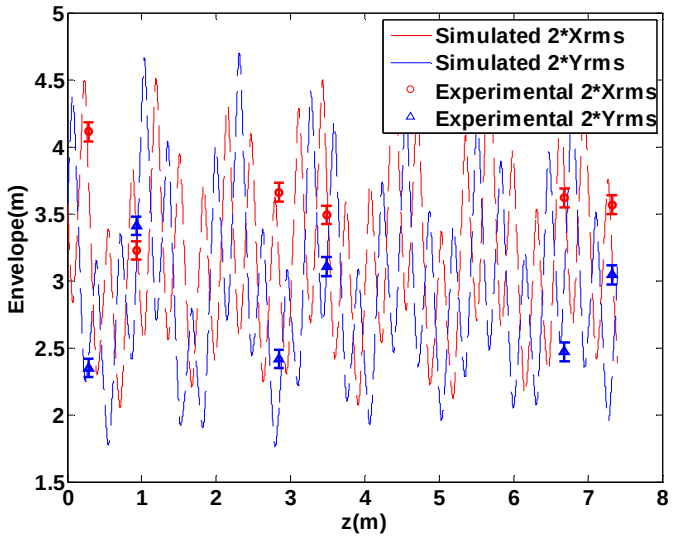

Figure 5.23: Comparison of Envelope between simulation and experimental data for 6mA beam in breathing mode (mismatch parameter μ = 1.2)

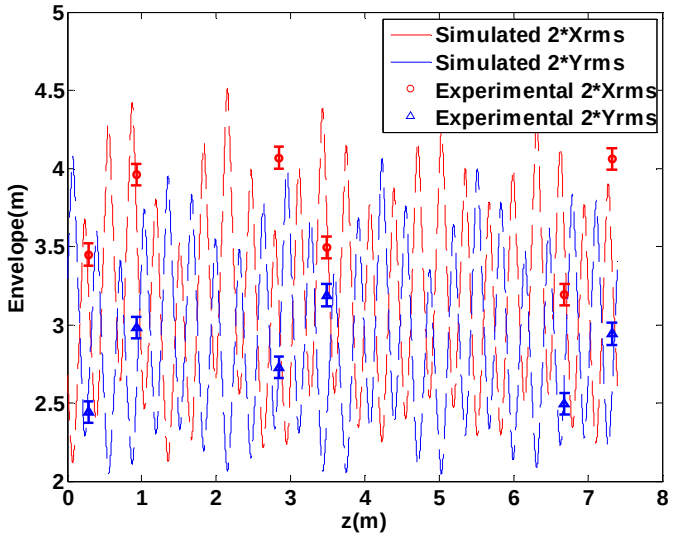

Figure 5.24: Comparison of Envelope between simulation and experimental data for 6mA beam in quadrupole mode (mismatch parameter μ = 0.8)

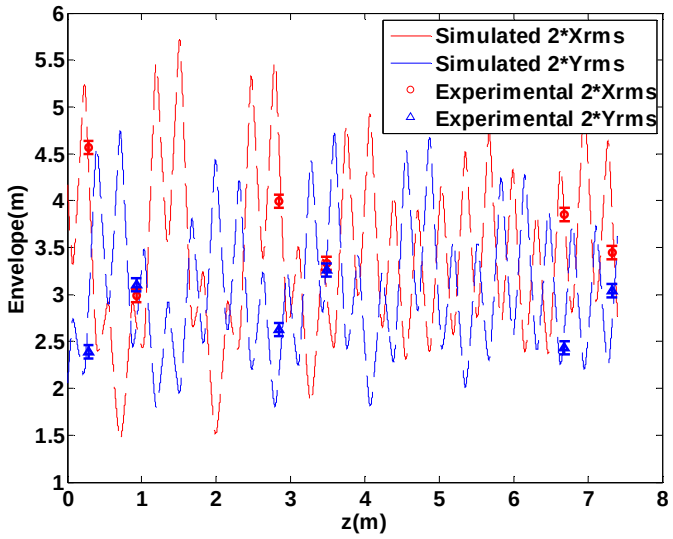

Figure 5.25: Comparison of Envelope between simulation and experimental data for 6mA beam in quadrupole mode (mismatch parameter μ = 1.3)

In order to measure the maximum halo radius and compare with the core particle theory and previous simulation, I have to use the optical mask method as discussed in section 2.5. Here, I use a PIMAX camera [44], which features a gated intensifier CCD with 1000*1000 pixels. The optics design is based on Fig. 2.4 and the whole setup is shown in Fig. 5.26. Before I take any image, two calibrations are made as shown in Fig. 5.27 and Fig. 5.28. For the first calibration, I apply a checker board mask on the DMD and use a flash light to illuminate the DMD. It checks the focus of the second focus channel and identifies the DMD edges in the CCD coordinates, which allows us to generate the mask because in the mask generation process, I need to calculate distances of the points I want to mask out to the four edge of DMD in camera coordinate, and then I can transform them to the DMD coordinate. The second calibration gives the real resolution of each pixel for size calculation.

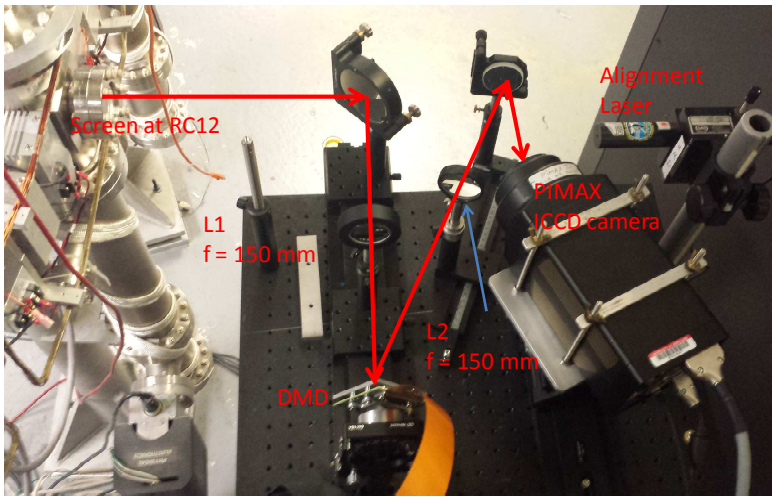

Figure 5.26: Setup of the optical mask method for halo measurement

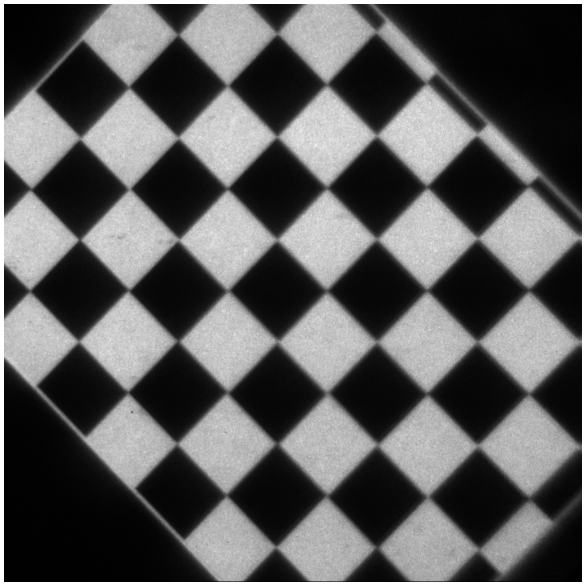

Figure 5.27: Calibration image of DMD indicating the edges of the DMD in CCD coordinate. The DMD is illuminated by a flush light. Camera is in shutter mode with 5 μs exposure time.

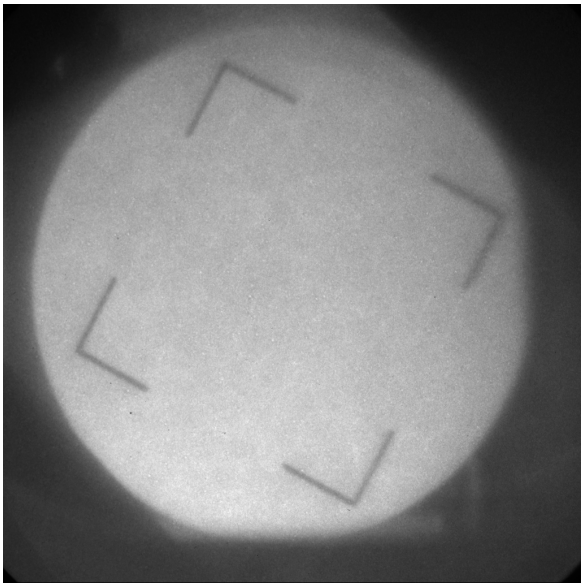

Figure 5.28: Calibration image of screen. The 80 mA beam is defocused to fill full of the screen for this calibration. There is straight light from background since we did not shut down all the light for the calibration. Camera is in gate mode with gate time 500 μs for 100 integration frames.

When taking data, I cover all the optics with black cloth and shut down all the lights to prevent the any straight light from outside of the system. I use the beam master trigger to trigger the camera externally and set the gate to 500 μs to further cut down the noise light level while keeping enough light for image acquisition. For acquiring the image, I first apply a black mask to the DMD which let all the images go to the camera. To take the beam image, I set the integration frame to 20 to collect 20 pulses of the beam in order to let the image close to camera saturation to fully use the camera dynamic range. The peak intensity is about 25000. Based on the beam image, I generate a threshold mask with a 5000 threshold. I apply this mask on the DMD to block out the unwanted central beam core and retake another image with increased integration frame to 200. Note here, the UMER beams are quite stable and the difference between pulses is very small. The

images of the full beam and the halos are shown in Fig. 5.29 for breathing mode and Fig. 5.30 for quadrupole mode.

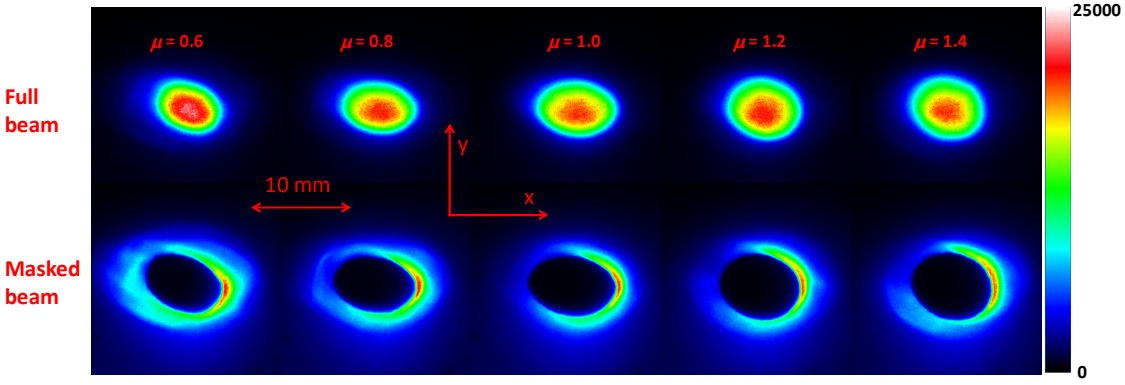

Figure 5.29: Beam images of full beam (upper row) and after core being masked out (lower row) for breathing mode (6mA beam).

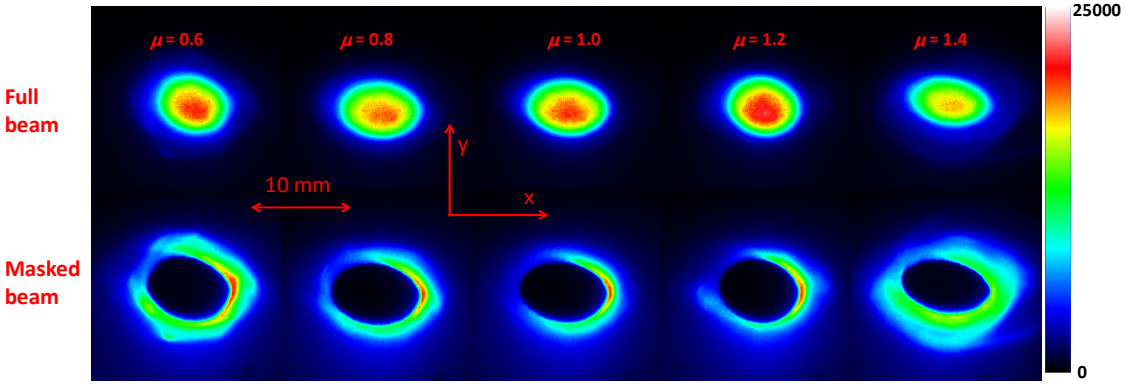

Figure 5.30: Beam images of full beam (upper row) and after core being masked out (lower row) for quadrupole mode (6mA beam).

In the particle core model, it predicts the maximum radius of halo particles as a function of mismatch parameter as indicated by Eqn. 5.15. There are limitations in the experiment to determine the maximum radius for very faint halo due to the dynamic range of the measuring method. (Previously in my master thesis, I showed a dynamic

range about 10^4 of the optical mask method in UMER. The limitation is due to the screen size and the dynamic range and efficiency of the phosphor screen.) Instead, I plot the measured radius (x-y averaged half-width of the beam) at 1% of peak intensity versus the mismatch parameter. The radiuses are determined in this way. From the full beam images, I obtain the peak intensity and according point for each mismatch case. From the peak intensity, I can calculate the 1% intensity level. This level should be then multiplied by factor of 10 for the difference of the integration frames. In the halo images, I do a horizontal or vertical scan from the peak point and determine the pixels at this level. The final radius is determined by half width each direction and then averaged by both directions. The error comes from the similar value of the adjacent point. I generally apply a ±15 pixels (about 0.53 mm) error, which implies a background noise. A plot of the half width of 1% of maximum intensity over matched rms size versus mismatch parameter is shown in Fig. 5.31 at RC12 for both mismatch modes. We compared the experimental results with simulation in same condition with Fig. 5.13 (In Fig. 5.13, the maximum radius is along the whole propagating channel, but here it is the local maximum at location of RC12). Here, we choose to plot the 1% of the maximum intensity averaged between x and y direction from the maximum point instead of the maximum extent. The experimental points lie on the simulation curve within the error bar except the largest mismatch case when μ =0.6, which is below the simulation curve. If compared with prediction curve from particle core model in Fig. 5.13, both experimental and simulation curves in Fig. 5.31 lies way below the theory curve (that is why it does not plotted here). Thus we can claim that the particle core model gives us an reasonable upper bound for maximum radius of halo particles.

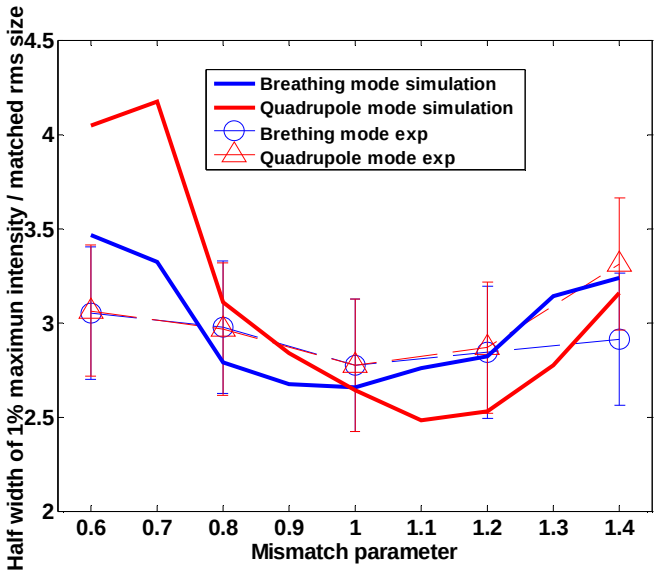

Figure 5.31: Beam half widths at 1% level of the maximum intensity versus mismatch parameter for both breathing and quadrupole mode mismatch. The comparison is between measured beam widths and simulated widths at RC12 (6 mA beam).

I also use the Tomography method to measure the emittance of the mismatched beam in x axis in RC12. The experimental data are plotted in Fig. 5.32 as brown square marker for breathing mode and pink triangle marker for quadrupole mode. The blue solid curve, red and green dashed curves are from Fig. 5.14 for comparison. The experimental data agree with the simulation curve well for breathing mode, but all lies below the simulation curve for quadrupole mode. All the data lies below curve predicted by the theory, which states that either at RC12 there is still free energy stored in the beam or other mechanism could absorb the free energy. As said in previous section, the emittance could increase anisotropically. Thus the average emittance of x and y will be more effective to compare with the theory but we lack of the emittance in y axis due to tight experiment schedule, which could be a future work.

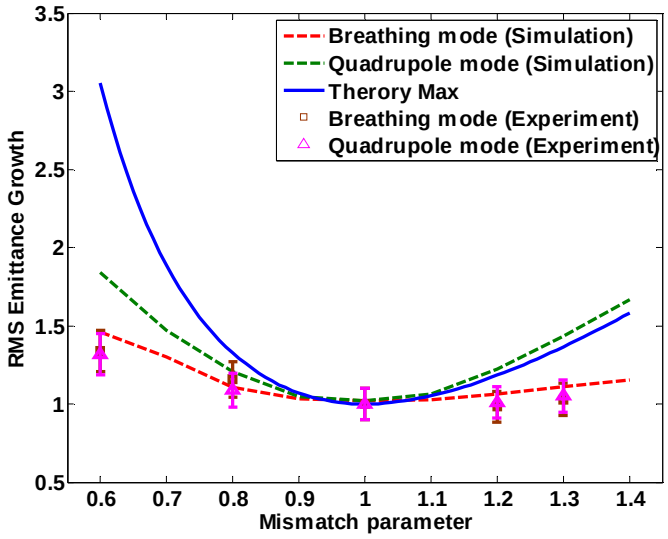

Figure 5.32: Measured RMS emittance growth for 6mA at RC12 for both breathing and quadrupole mode mismatch. The solid curve show maximum growth from the free energy model and the dashed curve is from simulation

5.6 Chapter conclusion

In this Chapter, I discuss the halo formation systematically with the mismatch parameter range from 0.6 to 1.4 in two envelope mismatch modes both in simulation and experiment. The agreement between the experiment and simulation is mostly satisfactory. The results support the prediction from free energy model as an upper limit for emittance growth with mismatch parameter in range of 0.6-1.4. The simulation results show the halo radius prediction from the particle core model is valid for mismatch parameter close to unity. For larger mismatch, when we apply this theory, especially for large intensity, it may be wise to consider a margin of a range about 20% to estimate the mismatch allowance and aperture requirement in the design of new high current, high intensity accelerators.

Chapter 6: DMD based application in accelerators

In chapter 2, I introduce an adaptive masking method for halo measurement. Later on, we found this diagnostic is quite useful in most of accelerators, not only to measure the beam halo using synchrotron radiation (in JLab FEL facility), but also to detect injected beam with high intensity stored beam presented in storage ring (in SLAC SPEAR3). In this chapter, I will discuss the application of this diagnostic.

6.1 Halo Experiments at Jefferson National Lab FEL Facility

6.1.1 Experiment Setup

The energy of the electron beam at the JLAB FEL accelerator [44] is 135 MeV. Various experiments such as the recently proposed Dark Light Project [45] require high current (10 mA) and high beam quality. Thus, it is important to know the spatial distribution of the beam with a high dynamic range. To fulfil the experimental need to measure the halo non-interceptively under high current operation of the FEL, we have developed a halo imaging system using optics similar to those described above, which images the beam in optical synchrotron radiation (OSR) as it passes through a bending magnet.

The differences in the optical system used for JLAB are as follows. First, slits are used to restrict the horizontal extent of the synchrotron light. Second, we need to transport the OSR beam image from downstairs in the shielded accelerator vault to an upstairs gallery, which houses the DMD and secondary optics. To do this we use an extra lens with a long focal length (1.5 m) to form an intermediate image in the transport path.

There are also two pico-motor controlled mirrors in the path to steer the synchrotron light through the optics and two flipper controlled screens with associated cameras to monitor the OSR transport. Third, a separate target set at the same distance as the source is used in order to measure the magnification and to achieve the best focus of the source at the DMD. The total magnification measured by using this target is 0.71.

6.1.2 Mask generation

The mask we applied to DMD is a 1024*768 pixels bitmap image with only 0 or 1 value indicating whether the pixel is reflecting the partial image toward camera or not. We apply this bitmap image and load it onto the DMD by the Texas instrument software called Discovery 4100 Explorer. To generate the bitmap mask image, a special Matlab GUI is developed as shown in Fig. 6.1.

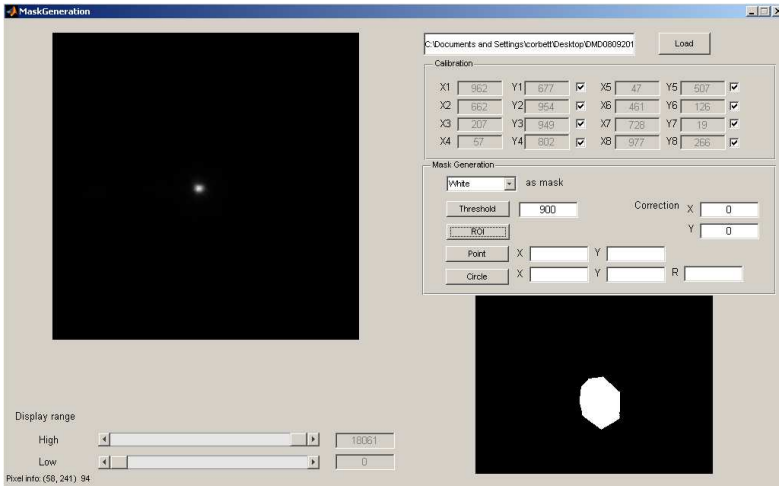

Figure 6.1: Mask generation GUI interface.

We first apply a check board mask (software included) onto DMD and take a calibration of the DMD. The image shown in Fig. 6.2 is the DMD with the check board

mask. Since the DMD is rotated, we need 8 points (as indicated in the image) to define the DMD edges in camera coordinate. For generating a single point mask, we calculate its distance to each of the DMD edge in the camera coordinate in that image and then scale up to the 1024×768 DMD coordinate. A general mask is a set of these single points. In the realistic operation, we first apply an all black mask (value 0 for all pixels) to obtain a full beam image. Based the full beam image, we have two methods to generate the mask. One is to choose a certain threshold value and mask out all the points higher than that value. This is applied in the point spread function measurement with gradually increased mask sizes (or decreased threshold) using certain turn of the stored beam which will be discussed later. Another one is to choose a region of interest (ROI) either by a polygon or a circle. For injected beam imaging, we choose a smaller threshold to generate a large mask, or choose a large ROI mask in order to prevent the leakage of the intense synchrotron radiation from the stored beam caused by jittering. A small correction is applied by shifting the mask in x or y axis in case that the mask is not perfect aligned with the region we want to mask out.

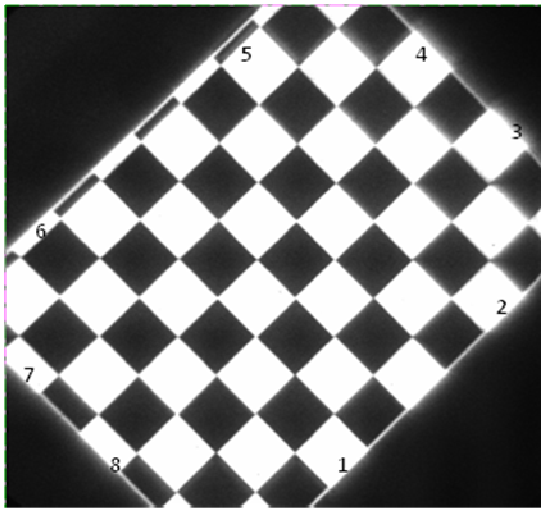

Figure 6.2: Image of illuminated DMD with a check board mask for calibration

6.1.3 Preliminary Results from JLAB

We used an electron beam with 1 ms macro pulse width, 60 Hz repetitive rate and 4.68 MHz micro-pulse repetition rate. Each micro-pulse contains a charge of 60 pc. We generated several masks based on threshold level. For each mask, we selected the appropriate integration time to bring the peak intensity of the image close to the saturation level of the camera. To obtain a background image for each mask setting, we covered the PVC tube which connected downstairs and upstairs, and integrated for the same time period used to obtain the corresponding masked beam image. Background-subtracted images are shown in Fig. 6.3, where the number in the lower left indicates the integration time used to obtain the particular image and the number in the lower right gives the threshold level for the generated mask. As shown in Fig. 6.3, the core masking method reveals an irregular spatial distribution of the beam halo.

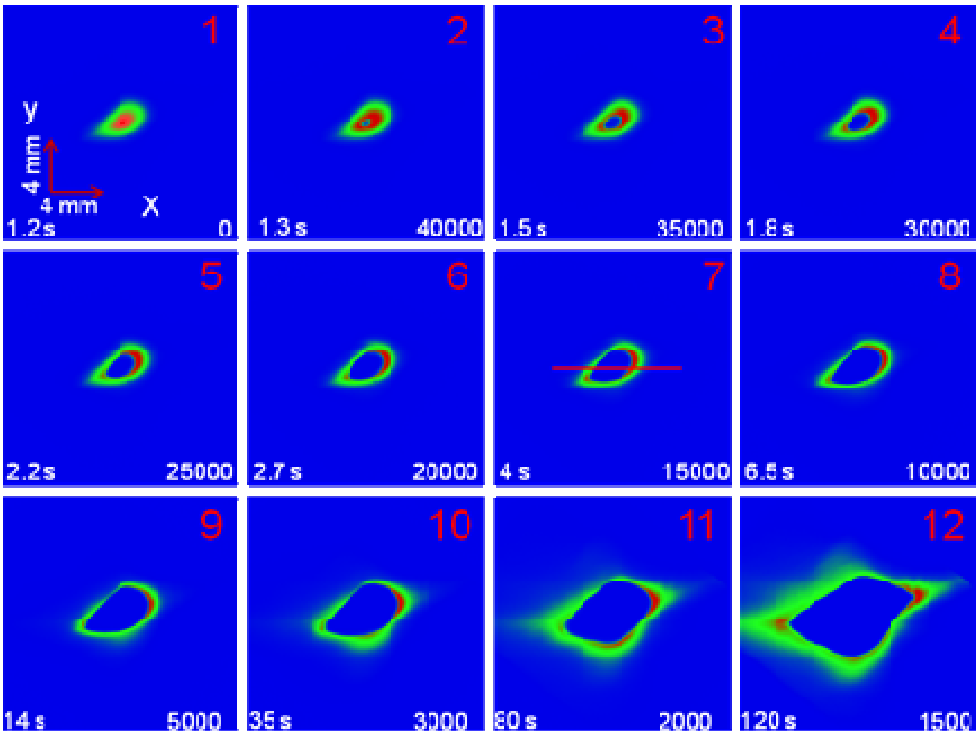

Figure 6.3: Unmasked and masked OSR images of the JLAB FEL beam.

When analyzing line scans across images 1, 3, 5, 7, 9, and 11 (note for reference the horizontal red line in Fig. 6.3), we normalized them by the integration time taken for each image. The normalized line scans are plotted in Fig. 6.4. As is observed in the tails of the line scans, the longer the integration time is, the smaller the intensity fluctuations are. In addition, the noise level is decreased to below 10^{-4}, which indicates a good dynamic range for the measurements obtained so far. This is expected to improve as we develop the optical system and focus the beam to a smaller spot size.

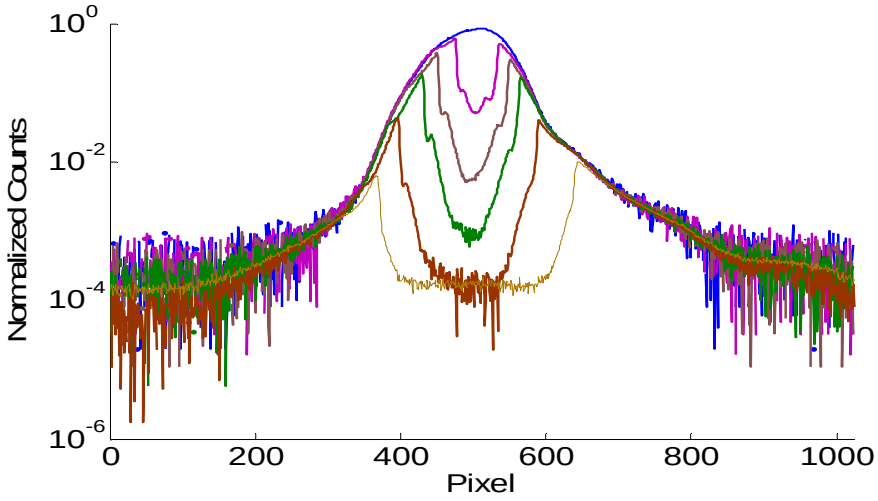

Figure 6.4: Normalized horizontal scans of beam profiles

6.2 Injected beam measurement in SLAC SPEAR3

6.2.1 Experiment Setup

The visible diagnostic beam line at SPEAR3 [47, 48] contains a rectangular aperture mask about 7 m from the OSR source point with an angular acceptance of 3.5 × 6 $mrad^2$. As showed as black dot in the right of Fig. 6.5, a ±0.47 mrad, horizontally extended 'cold figure' is located right after the primary aperture in order to absorb the

intense x-ray component of the light. This complex compound aperture creates a window-like shape at the first beam line lens and diffraction from the edges of the aperture contributes significantly to the overall shape of the point spread function (PSF) of the optics that is discussed later.

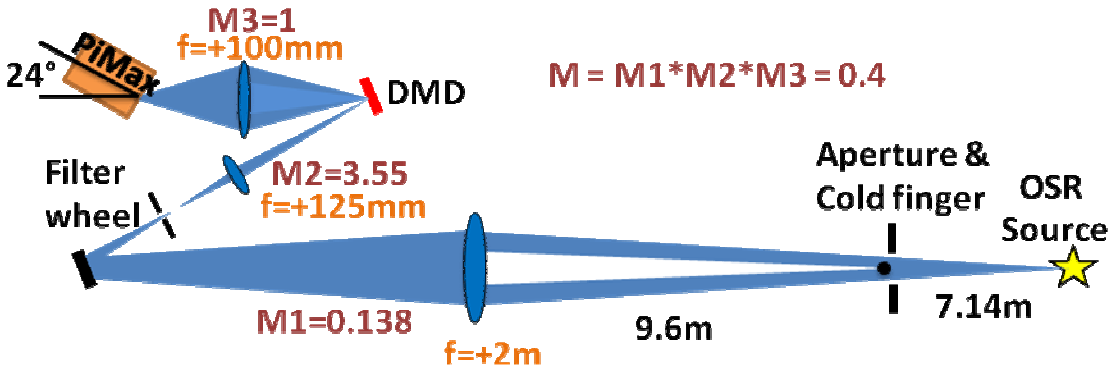

Figure 6.5: Layout of the optical system in the first synchrotron beam line of SPEAR3

A schematic of the beam line optics including the 2-channel DMD system is shown in Fig. 6.5. The image from the source is first imaged to a plane by f = 2 m objective lens and then re-imaged onto the DMD surface by a single acromat, f = 125 mm. At rest the micro-mirrors on the DMD surface are perpendicular to the incident light. The net magnification between the OSR source and the DMD camera is $M1*M2$=0.49. This allows us to easily image the ±8 mm betatron oscillations of the injected beam onto the 1 cm^2 surface of the DMD. When all the DMD micro-mirrors flip 12° toward the PiMax camera, the incident light will be reflected into the second optical channel which contains a third f = 100 mm achromat creating a 1:1 image relay system. Note that the camera is rotated 24° about the vertical axis to compensate for the Scheimplug effect [reference].

6.2.2 Point spread function Measurement

Point spread function (PSF) is the image of a point source through the whole optics. The image of any source can be considered as a convolution of the source distribution and the PSF. In our measurement of the PSF, we make the beam as small as possible to replace the point source. We use this PSF to test to which order our high dynamic range image is valid. It means that after normalization of both the PSF and the high dynamic image we measure later and lay them together in one plot, anything above the PSF is true; otherwise, it is un-trusted.

For the previous PSF measurement in UMER, we use a similar optics system with an actual line thread illuminated by a red laser as a point source. By progressively shifting the source away from the active area of CCD sensor of camera, and applying the well-calibrated neutral density filter to attenuate the light to avoid saturating the CCD, we achieved a dynamic range of 10^7 for halo measurement. In SPEAR3, however, it is not easy to find such a point source. Moreover, since our interest right now is the injected beam other than beam halos, and the injected beam is, in first several turns, away from the bright central stored beam, we want to prove the stored beam would not affect the measurement of the injected beam in this optics system. Therefore, the stored beam is sufficient approximation to simulate the point source. Strictly, the PSF mentioned here is a convolution of real PSF and the stored beam distribution.

To estimate the PSF, we were taking high dynamic ranges images of the stored beam alone. The stored beam was first imaged with an ND=2 filter and low MCP gain. Then we applied successive threshold level masks to the DMD in order to observe ‘halo’ or tails of the PSF with increasing detail. For each intensity mask we increased the

integration time (shutter mode of this camera was used [refer to camera]) to bring the peak intensity up to near the saturation level of the CCD sensor. To use long integration, we assumed that the visible light generated by the stored beam did not change during that time. Then by obtaining a number of images, each of which examined a segment of the total intensity profile, we were able to reconstruct a high dynamic range (~ 10^6) picture of the PSF. Figures 6.6 (a) and (b) show the first 3 and last 4 decades of the PSF, respectively. The inserted image on the top right corner of (b) is the light distribution incident on the objective lens, i.e. the aperture function (AF) of the optical system that is produced as the OSR passes through the rectangular beam line aperture and the horizontal extended cold finger. The cross like structure observed in (b) is the Fourier transform of the AF that is visible in the image plane. It is due to the horizontal and vertical structures of the AF. Note the additional slanted ray seen on the upper right quadrant of (b), which is caused by the tilted edge seen in the upper left side of the AF.

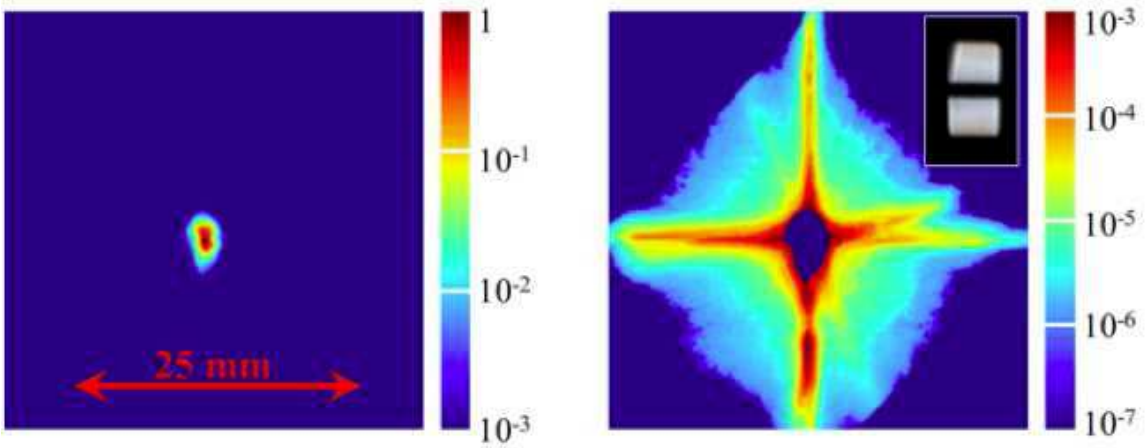

(a) (b)

Figure 6.6: Log normalized intensity profile of the SPEAR3 stored beam; (a) first 3 decades; (b) last 4 decades and insert showing aperture function of the visible beam line.

6.2.3 Injected beam imaging in off-duty test

In SPEAR, the design of the injection is to inject 3 GeV electron beams with certain intensity to fill SPEAR to several hundred mini-amperes with-in 5 minutes [49]. The electron beam starts from a 2.5 MeV rf-gun and is accelerated to 120 MeV in a linear accelerator. Then, it is injected into a booster synchrotron to reach the SPEAR injection energy, before being kicked into a beam transport line (BTS) to SPAER. A final orbit correction and envelope matching are performed inside the BTS to minimize beam loss due to injection. Since our diagnostic is located beside the first SPEAR synchrotron beam line, we can use it to record ordinary synchrotron radiation (OSR) of newer injected beam and determine how effective of the injection with certain magnet setting.

The OSR intensity from the injected beam is not strong enough, even with full MCP gain on the PiMax camera to image on a single pass with only one exposure. Thus, we utilized the synchronously-triggered gate mode of the PiMax to integrate several images per exposure (typically 15, which is the number of beams when each injection in a time interval of 5 mins during normal operation) prior to image readout. With stored beam present, the problem of rejecting the stored beam light intensity is therefore compounded 15 folds. Two methods are used to reject the intense light in the core of the stored beam: (1) masking the image of the stored beam using the DMD and (2) gating in time on the injected charge. In order to image the injected beam in the presence of the stored beam, an intensity threshold mask or a fixed sized mask is applied on the DMD. To generate the threshold mask we integrated the stored beam intensity over a long-exposure time, i.e. during the injection kicker bump excitation, and then numerically calculated the intensity threshold from the resulting image to define the mask. By doing

so, we can prevent the damage of the camera from the bright stored beam due to its transverse oscillation.

The main storage ring of SPEAR3 can be divide into 372 (not sure about this number) time buckets, with each bucket filled with 1mA to its saturation. For the beam advance one term with 781 ns, each bucket is roughly 2.1 ns. For the first set of injected-beam measurements we first filled 15 target buckets with the same amount of stored-beam charge (~1nC), and then progressively injected a single ~50pC shot into each of them advancing from bucket to bucket each shot. Simultaneously, the camera gate was synchronized with the injected beam pulse and automatically advanced from bucket to bucket. We call this process "clock mode" imaging. This has the advantage that the current of the stored beam in each bunch, which creates the background of each gated image, is kept nearly constant and the each bucket will not be saturated. In the alternative "stacking mode", in which injected pulses progressively increase the stored charge of a single bunch, we concerned that the increasing current of the stored beam might influence the injected beam dynamics. Moreover, the "clock mode" is the only way to make online measurements when machine is dedicated to synchrotron users. However, the disadvantage of clock mode is time-consuming, because it is necessary to dump the beam or advance to another group of target buckets after the charge in the target buckets becomes excessively high.

For synchronizing the beam with camera and cutting out the background light, we use four digital delay/pulse generators (or trigger box, Stanford research system, Inc) to give external trigger to the PIMAX camera and control a mechanical shutter. The mechanical shutter is used to further cut out the background light even when the camera

gate is closed or during the camera readout, because we see an effects of background light bleeding in these two events. The connections of all boxes are illustrated in Fig. 6.7 and the timing table is shown in Fig. 6.8.

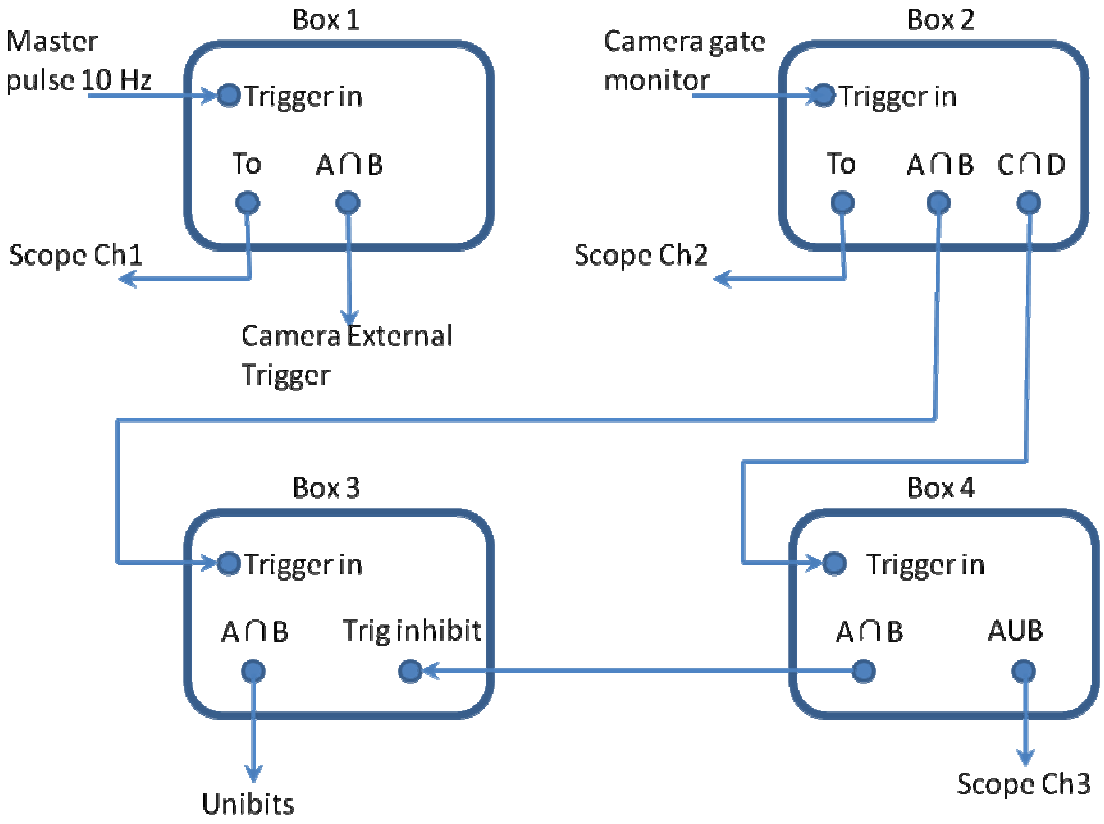

Figure 6.7: Schematic plot of the triggering system.

Box 1, triggered by the master trigger of SPEAR3, gives external trigger to the PIMAX camera. The master trigger is 0.1 s, indicating the injection rate is 10 Hz. The camera gate is delayed 320.232 ns (delay 1 in the timing table) to synchronize with the first turn. For nth turn, the delay time will be 320.232 + (n-1)*780 ns. Note that the beam circulates the SPEAR3 main ring by 780 ns. The gate opens 20 ns to cover the beam bucket. In the injection event, usually 15 new pulses are injected, so the number of gates is set to be 15. Box 2, triggered by the camera gate monitor signal, will trigger Box 3 and

Box 4. The signal generated by Box 3 controls the mechanical shutter open time with the positive trigger value. This signal is inhibited while an inhibited signal generated by Box 4 is zero. As shown in the timing table, the mechanical shutter inhibit signal is delayed by 25 ms compared with the camera first gate signal and its length is (pulse number -1) *100 ms. The mechanical shutter signal is delayed by 95 ms with a length of 4 ms. In this setting, the first beam pulse will not be collected as indicated by the dashed arrow, and the noise from readout will be reduced completely.

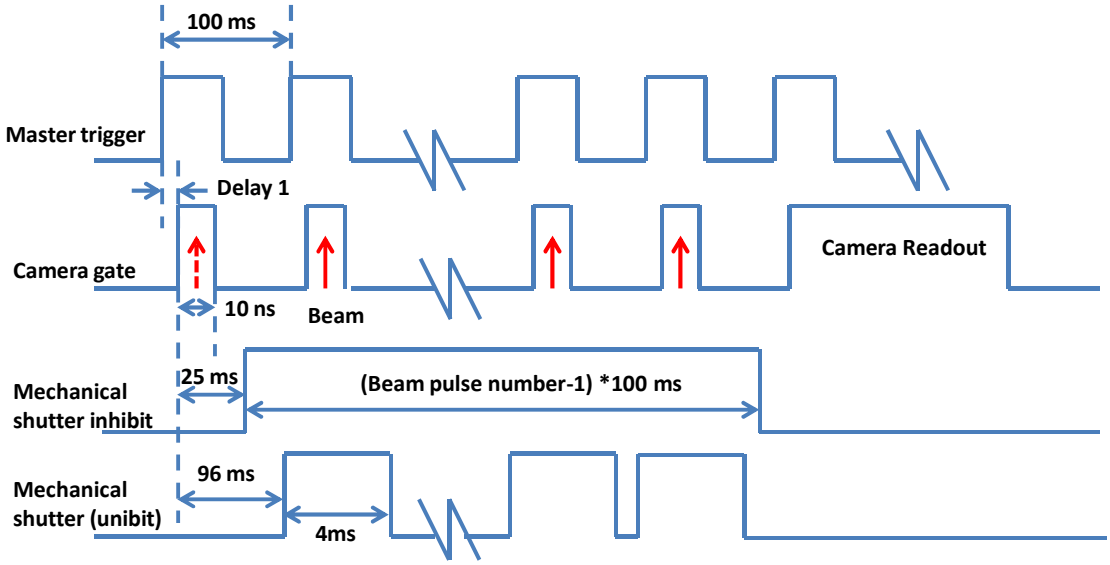

Figure 6.8: Timing table for injected beam imaging

We used the “clock mode” technique to image the injected beam shown at turn 6 for 15 shots with different single-bunch stored beam currents in Fig. 6.9. Here the outer crossing shape of the PSF clearly becomes more visible as the stored beam current is increased. Intensity profiles formed by integrating along the vertical axis are shown in Fig. 6.10 (a). The plots clearly show that with increasing stored beam current the illumination of the PSF (left peak) is enhanced while the intensity profile of the injected

beam (right peak) remains nearly constant. The constant profile of the injected beam also demonstrates that at these current levels the injected beam dynamics is not affected by space charge amplitude in the stored beam. This result is further confirmed by comparing the 2×rms x- and y- beam size profile plotted in Fig. 6.10 (b), which shows a nearly constant injected beam profile at turn 6, with values about x=2.6 mm and y=5.5 mm.

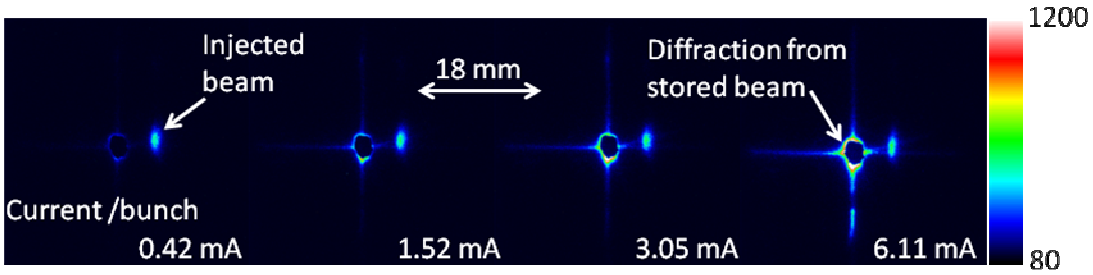

Figure 6.9: Masked with time-gated images of injected beam turn 6 with increasing single-bunch current.

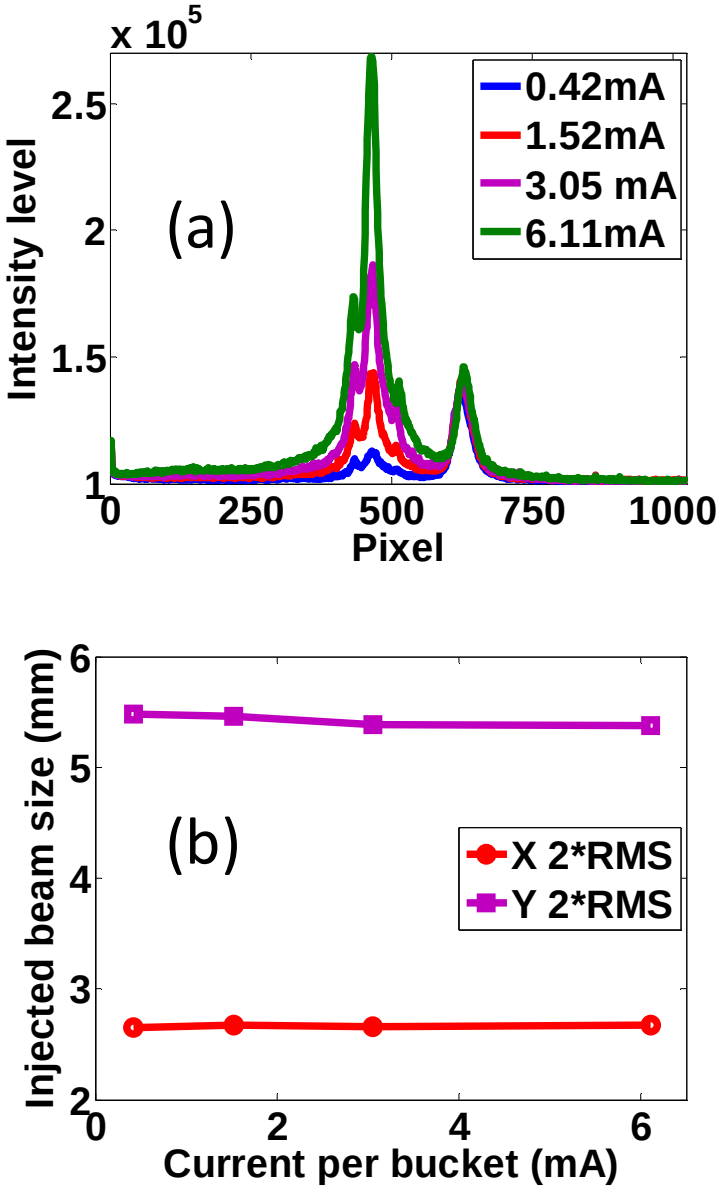

Figure 6.10: a) Horizontal intensity profile of the injected beam including PSF contribution from stored beam; b) 2×rms injected beam size vs. stored beam current.

6.2.4 Beam Mismatch Experiment

By altering the strength of the 9th defocusing quadrupole in the Booster-to-Storage ring (BTS) transport beam line, it is possible to change the phase-space matching of the injected beam with respect to the storage ring and impact charge capture efficiency.

For these tests, we used the same “clock mode” data acquisition process as before but generated a larger “rectangular” DMD mask instead of an intensity mask. The reason is when the injection kicker fires, it also give the stored beam a kick, which increase the amplitude of the betatron oscillation. Fig. 6.11 shows images of the 20 even turns of the injected beam for three different BTS matching conditions. For each condition, the plots are delineated by injection rate.

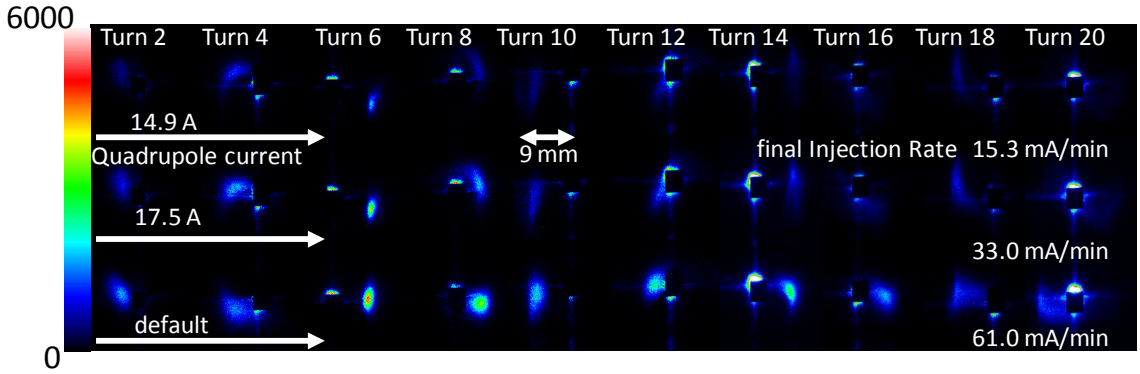

Figure 6.11: First 20 turns of the injected beam for three cases of matching condition.

Since the stored beam also has a small betatron oscillation, the cross-like PSF created by the stored beam moves picture to picture. It is not simple to take only one background to do background subtraction for all the beam images. In order to measure precisely the beam parameters, such as beam centroid and rms size, we need to take a background for each beam image using the same condition only without the injection. In reality, especially when the machine is dedicated for users, this measure will be tedious and even impossible. However, over the observation of the PSF, we found the shape of PSF almost does not change although jittering always. This allows us only taking one background and moves this background PSF to overlap with the PSF in each beam picture to do subtraction. The only drawback is that we still do not know the distribution

inside the mask where all the information is masked out by DMD. For this reason, we will not present the beam parameters for turn 12, 16 and 20.

The *x* and *y* centroid motions are plotted in Fig. 6.12. Comparing the oscillation in x and y direction, the amplitude is much larger in x (about 5 mm) than in y (about 2 mm), which consists with the fact that we inject the beam horizontally. Clearly the defocusing quadrupole strength has a limited effect on the horizontal betatron motion of the injected beam (dominated by the injection oscillation), but has a large impact in the vertical direction indicating a vertical beam offset in the 9thdefocusing BTS quadrupole.

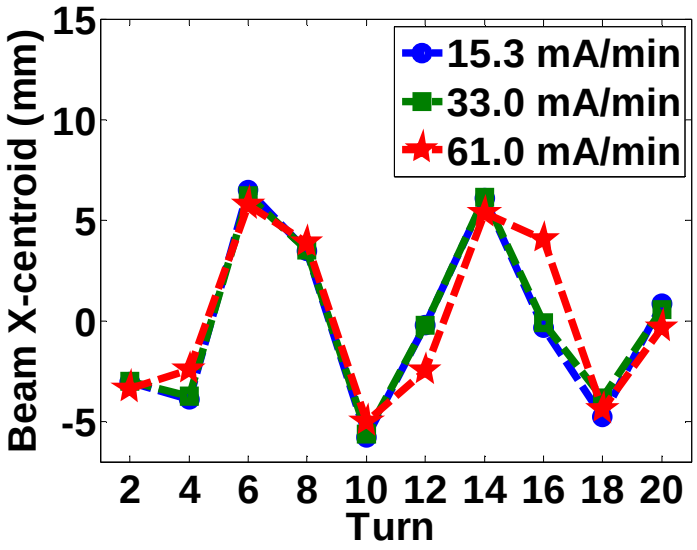

(a)

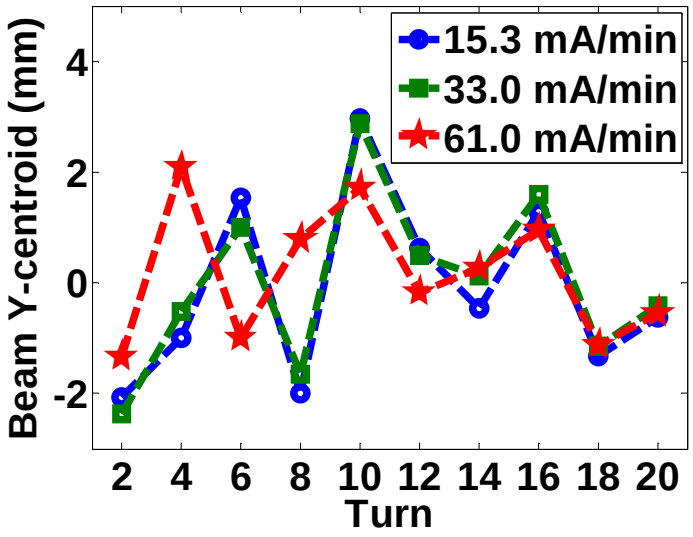

(b)

Figure 6.12: Beam centroid motion of the injected beam for the three different BTS matching condition. (a) x axis; (b) y axis.

We also plot the 2 × rms beam size for each turn in Fig. 6.13. For the *x* and *y* coordinates, the beam sizes are initially similar yet undergo different turn-by-turn evolutions due to different phase-space dynamics in each axis. The 2×rms size is not shown for turns 12, 16 and 20, since the images of the injected beam were partially blocked by the stored beam mask and light from the beam line PSF.

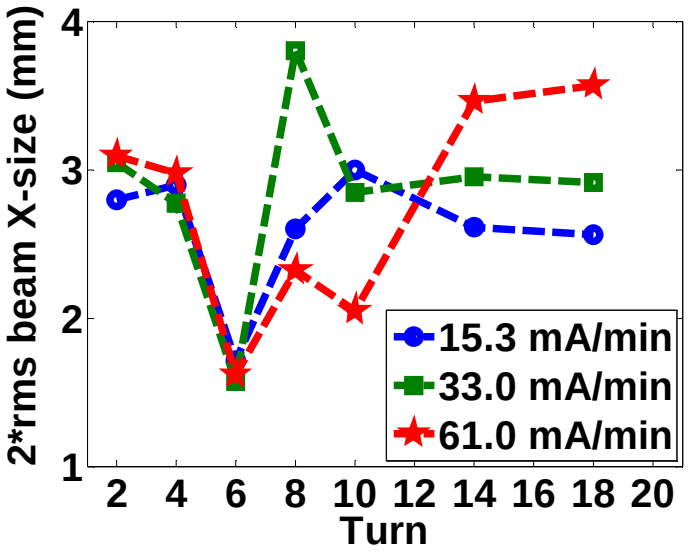

(a)

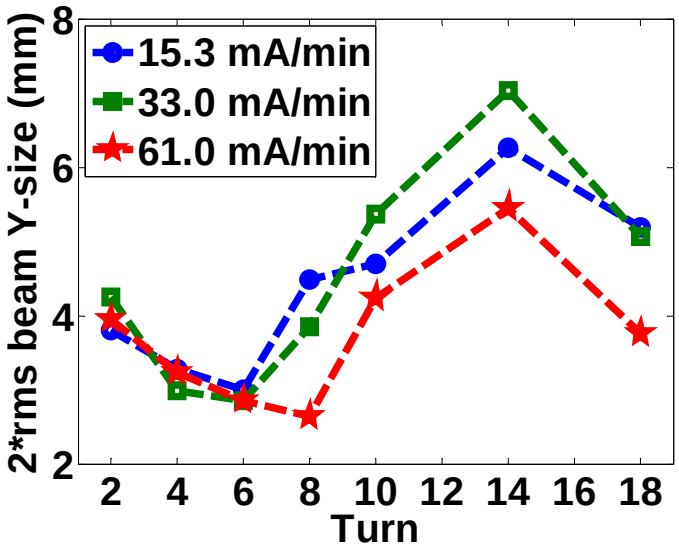

(b)

Figure 6.13: Beam size evolution of the injected beam with three different BTS quadrupole matching conditions. (a) x axis; (b) y axis.

For turns that can be clearly imaged, such as turns 6, 10 and 18, there is a linear relation between the integrated image intensity of the injected beam and the injection rate,

which is shown in Fig. 6.14. This indicates that most of the beam loss occurs in the BTS transport line or in the injection septum prior to entering the storage ring when we compare the two lower injection rate cases with the higher one.

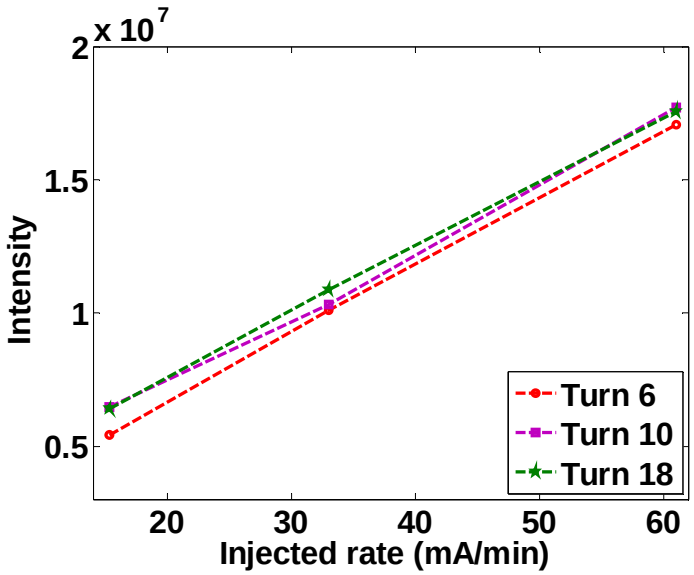

Figure 6.14: Total intensity of the injected beam versus injected rate for turn 6, 10 and 18.

6.3.5 Injected beam image in on-line test

Since the SPEAR3 is a user facility, most of its running time was dedicated to the user experiments. While it operate, the stored beam will get loss so that we need fill the ring with about 15 new beam pulses in a time interval of 5 minutes. The transportation of this injected beam pulses and their acceptance into the storage ring is very important, because it decides the capture efficiency and the filling frequency. To study the injection without perturbing the existing user experiments, the method discussed previously is right on the target.

In the experiment, we will still use the so-called “clock mode”. The filling time of this storage ring is about every 5 minutes, which means we can only get an injected beam image for a certain turn in that time interval. The gain is set as the maximum to increase

the visibility, and the gate width is set as 10 ns to avoid unnecessary noise as well. Figure 6.15 shows a series of turns of the injected beam while normal operation of SPEAR3. We can see the same structure of the stored beam is located in the center. Since the mask position is fixed according to the camera, it is obvious that the leakage of the cross-like shape indicates a jittering of the stored beam both in x and y direction. Thus in some case, the jittering is so big that we need make a larger mask (turn 22 and 26) to protect the camera from saturation. In order to show the injected beam in the same scale, the display range of these images is the same from 80 – 3000 as indicated by color bar.

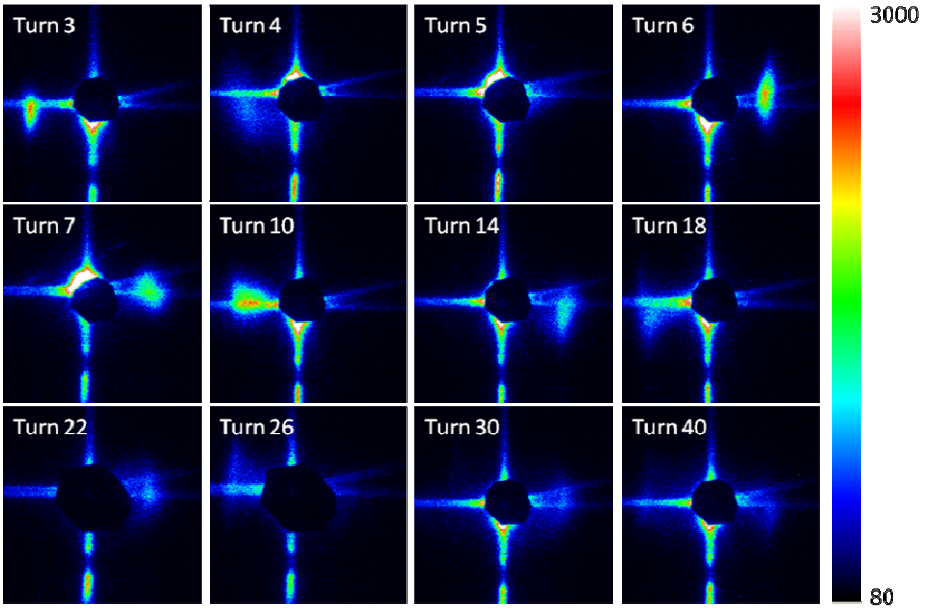

Figure 6.15: Beam images in different turns during normal operation.

After subtracting the background and the cross-like point spread function of the stored beam using the same method mentioned in previous section, we can analyse beam centroid and 2*RMS beam size from the injected beam image. (It is still hard to reconstruct the information hidden in the mask, so when the centroid of the injection beam is close to that of the stored beam, the analysis is not applicable. After the beam

smears, the measurement will have big error because we lack the information inside the mask). The beam centroid motions and beam sizes changes are plotted in Fig. 6.16.

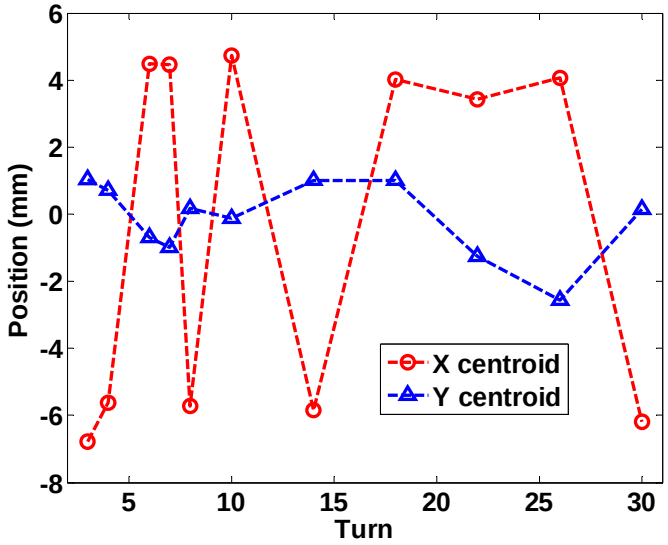

(a)

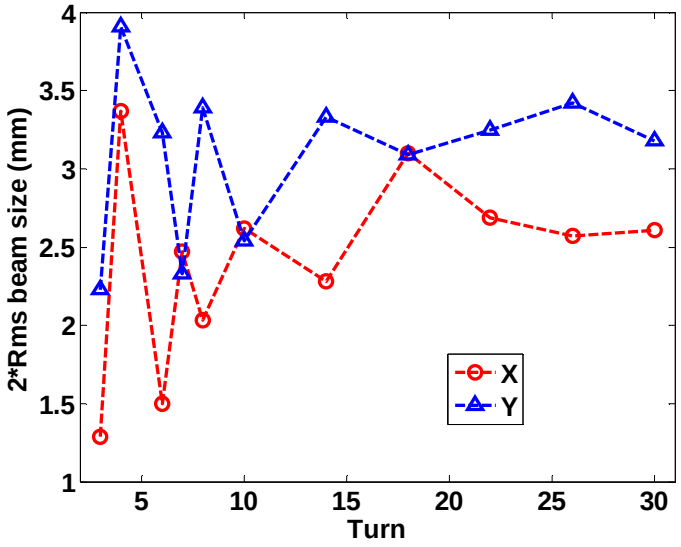

(b)

Figure 6.16: Turn by turn evolution of beam centroids and beam sizes during normal operation

Comparing with the off-line matched case, which has a largest injection rate of 61.0 mA/min, both the beams' centroid oscillation have a amplitude in the range of [-2,2] in y and [-5,5] in x. The different in oscillation detail could due to varied injection position and angle. For beam sizes and shapes, we can see some similarity in the sixth turn, but in general, the beams are even not close in shape for other turns. This could be a result of different injection phase and match condition are slightly off.

6.3 Chapter Conclusion

In this chapter, we discuss the application of the adaptive masking method used in halo diagnostic in JLab FEL facility and injected beam imaging in SLAC SPEAR3. We have succeeded in synchrotron radiation imaging and achieve a high dynamic range of 10^4 again in JLAB FEL facility. In SLAC SPEAR3, the novel diagnostic help solving the problem of the dynamic range issue when one images the synchrotron radiation from the injected beam with a strong intensity synchrotron radiation of stored beam existed.

Chapter 7: Conclusion

7.1 Summary

The goal of this dissertation is to better understand the halo formation in intense charged particle beams and figure out the dominated mechanism in beam dynamics for halo particles occurrence. As discussed in Chapter 1, the halo generation in accelerators can significantly degrade the beam quality and cause beam loss. The latter one might bring severe consequence for the maintenance of the accelerators and result in serious safety issues. The halo formation research gradually becomes an active research topic especially in high current and high intensity beams. The emphasis of this issue is very important and will give guidance for the design of the next generation of high intensity, high current accelerators.

As suggested by the particle core model, mismatch is major source for halo generation. I took a great effort to match the UMER beams in Chapter 3. First, I solved the magnet field error issue by studying the discrepancy between the experiments and simulations. This greatly reduces the beam loss for multi-turn operation and benefits not only my halo experiment but also other ongoing experiment in UMER. This is a more than important item to be checked before any sophisticated experiment. Moreover, I developed a matching procedure to do beam match by using tracking code as a coarse step and empirical method as a fine adjustment. Following by a rotation correction, I achieved an envelope match for three beams with increasing space charge intensities. The agreement of matched beam sizes for three cases is satisfactory between experiments and

Trace3D code prediction. For extreme space charge case, since the beam sizes are large, the beam shape is not regular due to image force from beam pipe. This could be improved by a better steering, which could be address further in the future. This procedure is quite general that it can be used to other beams in alternate lattice in UMER or even other accelerators with space charge.

I found out in Chapter 4 experimentally that the envelope mismatch is not the only source for halo generation, but also the beam rotation or skewness could contribute in the space charge dominated beam. The latter has been study in simulation before, but this is the first time we confirm it in experiment. From an initial beam rotation, I observed that the beam goes through a wobbling oscillation, and the associate energy from the oscillation will transfer to the beam particles to form halo. Either the envelope mismatch or beam rotation could result in a quick halo formation if the initial mismatch or rotation is large.

In Chapter 5, I systematically studied the halo formation with respect to different level of mismatch in the frame of pure mismatch modes. I developed a method for pure mode mismatch and testified it in warp code. The FFT analysis of the simulated envelope sampled with the lattice period shows a dominated peak of the wave number. The value of the peak is close to the mismatch wave number calculated from a smooth theory of periodic FODO lattice. I compare the maximum halo radius and emittance growth between theory, simulation and experiments. Both simulations and experiments agree well and confirm that free energy model gives an upper limit for maximum emittance growth and the particle core model is good approximation of the maximum halo radius. This suggests that both the models can be used to guide design of the high intensity and

high current accelerators. However, as said in the content, some margin should be taken into consideration.

I also include the application of the novel adaptive masking method in JLab FEL facility and SLAC SPEAR3. Followed from my master thesis, several properties are address in Chapter 2 to better understand the optics and compensations. In Chapter 6, I first applied the method for synchrotron radiation imaging and achieved a high dynamic range in JLab FEL facility. In SLAC SPEAR3, the implementation of the adaptive method helps to solve the injected beam imaging with present of the high intensity synchrotron radiation from stored beam.

7.2 Future work

As mention in Chapter 5, in the experiment, due to the limitation of screen size, I can only measure the halo particle to 1% level of the maximum intensity. One idea is to use the steering dipole to kick the beam centroid to the edge of the screen to full-use the screen size. Another one is to install wire scanner to measure the beam profile. Moreover, the emittance growth in y axis could be measured to further verify the free energy model.

Due to the geometry and design of current YQ section, although I solve the Eddy current problem, there is still misunderstanding of the fringe fields and image forces in this section. New design in UMER has been proposed for the extraction section [50], which could also be applied to the YQ section. I hope this will eventually help match the beam in multi-turn.

Meanwhile, the knock-out method [51] or the installation of an extraction section in the future will help with multi-turn diagnostic which means the halo study in this

dissertation could be extended to multi-turn and include infinity FODO lattice or mismatch periods if not consider the longitudinal erosion. The topic of halo formation rate could be studied for a long distance in the frame of small or large mismatch parameters or other possible parameter which could affect the halo formation process. Neither particle core model nor free energy model addresses this problem but it is of importance for new accelerator design and operation.

Appendices A: Sample matching code in Trace3D

```
&DATA
ER=  0.510999  Q= -1.  W=     0.01000  XI=  6.000000
EMITI =     17.856250       17.856250    0.1800000
BEAMI =     0.180800       0.053600      0.180800       0.053600
-1.15      250000.0
BEAMF =     -2.670300       0.710700      2.614600       0.667800
1.15      250000.0
BEAMCI=       0.00000       0.00000       0.00000       0.00000
0.00000       0.00000
FREQ=    5.000  ICHROM= 0  IBS= 0  XC=   0.0000
XM=  27.95  XPM=  50.0000  YM=  27.95  DPM=  30.00  DWM=  100.00  DPP=
30.00

N1=  1  N2= 37  SMAX=   0.1   NEL1=   1   NEL2=  37   NP1=   1   NP2=
37
MT=  8
MP = 1,11,1,13,1,7,1,9
CMT(001)='Gun-Sol '  NT(001)=  1  A(1,001)=  138.700000
CMT(002)='Sol-smoo'  NT(002)=  5  A(1,002)=  81.807703      65.200000
CMT(003)='Sol-Strt'  NT(003)=  1  A(1,003)=  116.100000
CMT(004)='Strt-Q1 '  NT(004)=  1  A(1,004)=  62.925000
CMT(005)='Q1-DeFoc'  NT(005)=  3  A(1,005)=  0.032860      44.750000
CMT(006)='Q1-Q2   '  NT(006)=  1  A(1,006)=  87.250000
CMT(007)='Q2-Focus'  NT(007)=  3  A(1,007)= -0.059070      44.750000
CMT(008)='Q2-Q3   '  NT(008)=  1  A(1,008)=  145.250000
CMT(009)='Q3-DeFoc'  NT(009)=  3  A(1,009)=  0.058410      44.750000
CMT(010)='Q3-Q4   '  NT(010)=  1  A(1,010)=  151.250000
CMT(011)='Q4-Focu '  NT(011)=  3  A(1,011)= -0.056370      44.750000
CMT(012)='Q4-Q5   '  NT(012)=  1  A(1,012)=  98.250000
CMT(013)='Q5-DeFoc'  NT(013)=  3  A(1,013)=  0.057520      44.750000
CMT(014)='Q5-Q6   '  NT(014)=  1  A(1,014)=  115.250000
CMT(015)='Q6-Focu '  NT(015)=  3  A(1,015)= -0.055740      44.750000
CMT(016)='Q6-YQ   '  NT(016)=  1  A(1,016)=  106.459939
CMT(017)='YQ-DeFo '  NT(017)=  3  A(1,017)=  0.044140      58.330123

CMT(018)='        '  NT(018)=  1  A(1,018)=  50.834939
CMT(019)='PD      '  NT(019)=  2  A(1,019)=  2754949.06      2754.95
CMT(020)='        '  NT(020)=  1  A(1,020)=  50.005000
CMT(021)='QR1-Foc '  NT(021)=  3  A(1,021)= -0.042870      59.990000
CMT(022)='        '  NT(022)=  1  A(1,022)=  107.630000
CMT(023)='QR2-DeFo'  NT(023)=  3  A(1,023)=  0.055840      44.750000
CMT(024)='        '  NT(024)=  1  A(1,024)=  57.625000
CMT(025)='Dipole  '  NT(025)=  2  A(1,025)=  15680.00      3500.00

CMT(026)='Drift   '  NT(026)=  1  A(1,026)=  57.625000
CMT(027)='Foc.Quad'  NT(027)=  3  A(1,027)= -0.055038      44.750000
CMT(028)='Drift   '  NT(028)=  1  A(1,028)=  115.250000
CMT(029)='Def Quad'  NT(029)=  3  A(1,029)=  0.055038      44.750000
CMT(030)='Drift   '  NT(030)=  1  A(1,030)=  57.625000
CMT(031)='Dipole  '  NT(031)=  2  A(1,031)=  15680.00      3500.00

CMT(032)='Drift   '  NT(032)=  1  A(1,032)=  57.625000
CMT(033)='Foc.Quad'  NT(033)=  3  A(1,033)= -0.055038      44.750000
CMT(034)='Drift   '  NT(034)=  1  A(1,034)=  115.250000
```

```
CMT(035)='Def Quad'  NT(035)=  3  A(1,035)=  0.055038      44.750000
CMT(036)='Drift   '  NT(036)=  1  A(1,036)=  57.625000
CMT(037)='Dipole  '  NT(037)=  2  A(1,037)=  15680.00      3500.00

COMENT='UMER Y-matching Step 3'
&END
```

Appendices B: Sample simulation code in python

```
from warp import *

sys.path.insert(1, "/ebte/pywarp/rscripts/scripts_a")
sys.path.insert(1, "/humer/shared/Universal")
sys.path.insert(1, "humer/shared/WARP/Warp32_2011-2-22/scripts")

if 'GISTPATH' in os.environ.keys(): os.environ["GISTPATH"] +=
":/ebte/pywarp/rscripts/scripts_a"
else:   os.environ["GISTPATH"] = "/ebte/pywarp/rscripts/scripts_a"
from rami_scripts import *
from UMERGeometry import *
from ParaKV import *
from rami_match import *

################ G L O B A L   P A R A M S ####################

ltest = 0
lmatch = 0
lscreen = 0
lquadcenter = 0
nperds = 30

pm_initial = 0.0 #degree
pm = pm_initial


if lmatch:
  nperds = 2

a0_initial       = 0.0038688
b0_initial      = 0.0038766
ap0_initial     = -0.014067214
bp0_initial     = 0.014112477
offset_hao = -0.945

I_initial          = -7.45*0.8e-3
emit_initial_x  = 12.874e-6
emit_initial_y  = 12.874e-6


if len(sys.argv) == 1:  # Running single simulation
   # quad current in Amps (positive: focus on x (horiz), de-focus on y (verical))
```

```
   runnum = 501
else:                # Running one of a sequence of simulations
   runnum = int(sys.argv[1])
   inputdata = sys.argv[2]
   f1 = open(inputdata, 'r')
   lines = f1.readlines()
   f1.close()
   data = lines[runnum]
   items = data.split()
   [a0_initial,b0_initial,ap0_initial,bp0_initial] = [float(i) for i in items]
   print "a0 = %-.3f, ap0 = %-.3f, b0 = %-.3f, bp0 = %-.3f,"
%(a0_initial,ap0_initial,b0_initial,bp0_initial)

file1_name = "halo_particle_MaxRadius"+str(runnum)+".txt"

if lscreen:
        a0_initial      = a0_initial
        ap0_initial     = ap0_initial
        b0_initial      = b0_initial
        bp0_initial     = bp0_initial
        offset_hao = -29.1425

if lquadcenter:
        a0_initial      = 0.003566#0.002435
        b0_initial      = 0.002731#0.003947
        ap0_initial     = -0.013296#-0.0001175
        bp0_initial     = 0.010747#0.000453
        offset_hao = -8.0

###############  Injector Quadrupole scan#############
# --- Set four-character run id, comment lines, user's name.

if runnum < 10:
  crun = "0"+str(runnum)          # Run number if more than one simu with same runid
else:
  crun = str(runnum)
runid += crun
top.runid[0] = runid


top.pline2 = "TRACE Matching - 6 mA, fixed POS, after SOL, BEarth, Dipole f from R-
MAT"
# top.pline1 is automatically filled later
top.runmaker = "Hao Zhang"

# --- run control
```

```
ltest      = ltest          # set to 1 to speed up simulation for testing
if lmatch:
   ltest      = 1
lpicts     = 0          # Take density pictures?
lcalc_mom  = 1          # Calculate additional moments? (needed for quad rotation or
dispersion)
if lmatch:
   ltest = 1
# --- Comparison Plots against other simulation

lcompare = 0
dot1 = "FixedMatch_6mA_AS_BE_NewDip_exp"       # Runid of old simulation (to
compare against)
old_crun = "1"          # Run number of old simulation
cf_title = "Change Q1"


# --- Invoke setup routine (THIS IS MANDATORY)
setup()


############ B E A M   P A R A M E T E R S   1 ###############

# +++ energy [eV] and species (current and zion -ve for electrons)
top.ekin     = 10.0e03
top.aion     = top.emass/top.amu
top.zion     = -1.
top.lrelativ = yes                    # relativistic particle push

derivqty()  # calculate additional beam parameters, eg. top.vbeam from ekin.

# +++ For dispersion and chromaticity: add a longitudinal thermal velocity
e_spread     = 10.0                   #  Longitudinal energy spread in eV
top.vthz     = top.vbeam*e_spread/(2.*top.ekin)


#################### INITIAL DISTRIBUTION ######################

w3d.distrbtn = "semigaus"  # load  semi-Gaussian distribution
#w3d.distrbtn = "K-V"       # load KV distribution



#################### GEOMETRY & GRIDDING ######################

# +++ General
```

```
top.npmax = 1000000          # Number of simulation macro-particles (40,000 typical,
more if tracking
stepsize  = 0.001          # step size in m
ncells    = 512            # number of cells in each direction (power of 2)

if lpicts:  top.npmax = max(top.npmax, 320000)
if ltest:                  # DO NOT CHANGE THESE.  Use only for fast testing
   top.npmax = 5000
   ncells = 256
   stepsize = 0.004

# +++ Boundaries and Gridding
top.prwall = pr1 = 2.45e-2  # Remove particles outside of Pipe radius
boxrad = 2.5e-2                          # Box 1/2 side > pipe radius (pr1)

w3d.xmmin = w3d.ymmin = -boxrad
w3d.xmmax = w3d.ymmax =  boxrad
w3d.nx = w3d.ny = nint(ncells)


# +++ Particles
top.stickyxy = 1           # remove particles when they hit pipe.
top.ibpush   = 1           # set type of pusher to  vXB push without tan corrections

# +++ Stepsize
top.dt = stepsize/top.vbeam                # OK, 0 injection
#wxy.lvzchang = 1    # If 1, fancy algorithm is used to find top.dt

####################  SPECIFY LATTICE  ##########################

# --- do a doc() on each method to determine optional arguments
#ring = UMER('iyr', oppoint="83%", crun=crun, nturns=1, nperds=2, lEarth=1,
verbose=1, lpf=0, offset = offset_hao, diags='a',pdiags='s')
ring = UMER('r',oppoint="83%", crun=crun, nperds=nperds, nturns=4, lEarth=0,
verbose=1, lpf=0,stopatscreen=0, diags='a',pdiags='s', funcs=[pptrace],
pltype='density',offset = offset_hao )



############ B E A M   P A R A M E T E R S   2 ###############

# --- ring.select_beam(aperture, operting point) automatically loads a matched beam
# --- can override by commenting out and/or directly editing top.* parameters
#beam = ring.select_beam("6mA", "83%")

# +++ envelope and slope [m, rad], specific number for the starting point
```

```
top.a0       = a0_initial   #beam.a0
top.b0       = b0_initial   #beam.b0
top.ap0      = ap0_initial    #beam.ap0
top.bp0      = bp0_initial    #beam.bp0

# +++ centroid and angle [m, rad]
top.xcent_s  = 0.0#beam.xcent
top.xpcent_s = 0.0#beam.xpcent
top.ycent_s  = 0.0
top.ypcent_s = 0.0

# +++ current [A], unnormalized 4*rms emittance [m-rad]
top.ibeam    = I_initial#beam.ibeam
top.emitx    = emit_initial_x#beam.emitx
top.emity    = emit_initial_y#beam.emity
top.emit     = emit_initial_x#top.emitx

# --- Hollow or peaked initial distribution, if desired
w3d.hollow = 0          # 0 = flat; 2 = parabolic density
w3d.hollow_h = 0.5      # n(w3d.rho)  not  1 + ((1-h)/h)*w3d.rho**2
if (w3d.hollow == 2):  # WHY IS THIS COMMENTED OUT?
   # --- form factor for parabolic density profile
   Stf = sqrt( (2.*w3d.hollow_h+4.)/(3.*w3d.hollow_h+3.) )
   # --- scale loading parameters so the correct rms values are loaded
   top.a0 = top.a0*Stf
   top.b0 = top.b0*Stf
   top.ap0 = top.ap0*Stf
   top.bp0 = top.bp0*Stf
   top.emit = top.emit*Stf**2


# !!! 5-beamlet: create module with choices?
# !!! Hollow-vel: must load after generate()

if top.lrelativ: top.ibeam = top.ibeam/(top.gammabar**2)    # Correct field solve

top.pline1 = ring.calc_pline()


########### F I E L D    S O L V E R ####################

top.fstype = 1
#      -1       To Turn off field solver
#       1       FFT Solver w/ Capacity Matrix (inifinite)

# --- Set up Capacity Matrix for WARPxy
```

```
fxy.ncxy    = fxy.ncxymax = w3d.nx+w3d.ny   # set number of points
gallot("CapMatxy",0)                        # Allocate the arrays
# -- Coordinates of boundary points in meters
fxy.xcond[0:fxy.ncxy] = pr1*cos(2.0*pi*arange(fxy.ncxy)/fxy.ncxy)
fxy.ycond[0:fxy.ncxy] = pr1*sin(2.0*pi*arange(fxy.ncxy)/fxy.ncxy)
fxy.vcond[0:fxy.ncxy] = 0.e0                # Put pipe at ground

f3d.lcndbndy = true     # enable subgrid interpolation

################ D I A G N O S T I C S #################

top.nhist = 1       # at what frequency of steps to save moment histories
top.itmomnts[0:4] = [0,1000000,abs(top.nhist),0]

top.xpplmin = top.ypplmin = -0.015    # limits to use on particle plots
top.xpplmax = top.ypplmax = 0.015

top.verbosity = 1   # Turn off built-in oneliner output
top.npplot = [top.npmax/10, 5000, 2500]      # Number of particles to save
top.ncolor = 10
#palette("gray.gp")


################  G E N E R A T E   ###################

# --- Generate the PIC code (allocate storage, load ptcls, t=0 plots, etc.)
package("wxy"); generate()

w3d.zmmax = 0.1;
# +++ Hollow velocity here, if needed
# +++
file1 = open(file1_name,"w")

def check_halo():
        Ellipse_ratio = array([1,1.5,2])
        Length_ratio=len(Ellipse_ratio)
        num1 = array([0.0]*(3*Length_ratio+7))

        for iii in range(0,3):
                out =
where((top.pgroup.xp/2/top.xrms)**2+(top.pgroup.uxp/top.vbeam/2/top.xprms)**2>Elli
pse_ratio[iii]**2,1,0)
                out1 =
where((top.pgroup.yp/2/top.yrms)**2+(top.pgroup.uyp/top.vbeam/2/top.yprms)**2>Elli
pse_ratio[iii]**2,1,0)
```

```
                out2 =
where((top.pgroup.xp/2/top.xrms)**2+(top.pgroup.yp/2/top.yrms)**2>Ellipse_ratio[iii]*
*2,1,0)
                num1[iii]=sum(out)
                num1[3+iii]=sum(out1)
                num1[6+iii]=sum(out2)

        num1[3*Length_ratio] = max(top.pgroup.xp)
        num1[3*Length_ratio+1] = min(top.pgroup.xp)
        num1[3*Length_ratio+2] = max(top.pgroup.yp)
        num1[3*Length_ratio+3] = min(top.pgroup.yp)

        ix_cen = sum(where(w3d.xmesh < 0.,1,0))
        iy_cen = sum(where(w3d.ymesh < 0.,1,0))
        rho_x = getrho(iy=iy_cen)
        rho_y = getrho(ix=ix_cen)
        rho_min = max(minnd(rho_x),minnd(rho_y)) #electron, negative charge density

        xx = sum(where(rho_x/rho_min>=0.01,1,0))*(max(w3d.xmesh)-
min(w3d.xmesh))/(size(w3d.xmesh)-1)/2 #1% maximun intensity location
        yy = sum(where(rho_y/rho_min>=0.01,1,0))*(max(w3d.ymesh)-
min(w3d.ymesh))/(size(w3d.ymesh)-1)/2 #1% maximun intensity location
        xxyy = (xx+yy)/2;
        num1[3*Length_ratio+4] =xx
        num1[3*Length_ratio+5] =yy
        num1[3*Length_ratio+6] =xxyy

        output = str(top.it*stepsize)+"\t"
        for aaa in num1:
                output += str(aaa)+"\t"
        output += "\n"
        file1.write(output)


# +++ output parameters
if lpicts: installafterstep(ring.snapshot)
installafterstep(ring.oneliner)
installafterstep(ring.pplots)
installafterstep(check_halo)


##################hollow velocity#################
#para_temp(delta_hp=-0.3,delta_h=None)
#loadvels(func=dualgauss, vm=0.01, vs=0.008, cut=0.038, npts=1000)
```

```
################ Particle SIMULATION  ##################

pplot(0, [pptrace], "density")    # Plot at beginning
ring.oneliner()

stime = wtime()


# ===  PHASE III:  RING
top.zlatperi = ring.rperi
top.zlatstrt = ring.roffset

ring.initialize()
bgidq=ring.load_ring_quads()
bgidd=ring.load_ring_dipos()
ring.load_ring_steerers()
ring.load_B_Earth()

ring.finalize()



step(ring.nstr)

etime = wtime()
print "Time Running = ", etime-stime

pplot(0, [pptrace], "density")    # Plot at end

if lmatch:
   s = 0.32/stepsize
   match2(imtch=5,s=s)

#################### S A V E  D A T A ######################

top.lenhist = top.jhist     # get rid of the zeros at the end of moment history arrays
gchange('Hist')

if lcalc_mom:   # see rami_scripts.py for following functions
   calc_mom()             # calculates rotation and dispersion moments
   save_long(crun=crun)    # appends runid to selected moments and saves to pdb file
else:
   save_data(crun=crun)    # appends runid to selected moments and saves to pdb file

ring.dump_moments()        # generate text files of moment data at diagnostic locs
```

```
######################## P L O T S ########################

begin  = swhere(ring.nperds>48, ring.nsti+ring.nsty, 0)
strobe = swhere(ring.nperds>48, ring.nstpp, 1)

# see rami_scripts.py for following plotting routines
plot_cent(begin=0,strobe=1, width=4.0)
(xi,xf,yi,yf, dum)=limits(); xpd = ring.pd_loc+ring.yoffset
if ring.rperds == 33:
   rpd = ring.prd_loc+ring.roffset
   plg(array([yi,yf]), array([rpd,rpd]), color='red',marker='PD')
plg(array([yi,yf]), array([xpd,xpd]), color='red',marker='PD');   fma()

if ring.rperds == 33:   # This zooms in on the recirculation part (optional)
   plot_cent(begin=0,strobe=1, width=4.0)
   (xi,xf,yi,yf, dum)=limits(); xpd = ring.pd_loc+ring.yoffset
   rpd = ring.prd_loc+ring.roffset
   plg(array([yi,yf]), array([rpd,rpd]), color='red',marker='PD')
   limits(11.0,15.0,yi,yf); fma()

if ring.nperds>48:
   plot_env( begin=0,strobe=1, end=begin, width=4.0, ymin=0.0)
   plot_env( begin=begin,strobe=ring.nstpp, width=4.0, ymin=0.0, type="dot"); fma()
else: plot_env( begin=0,strobe=1, width=4.0, ymin=0.0); fma()

plot_emit(begin=0,strobe=1, width=4.0, ymin=10, ymax=40);   fma()
plot_np(ymin=0.0);     fma()

if lcalc_mom:
   plot_remit(begin=0,strobe=1, width=4.0, ymin=10, ymax=40);   fma()
   plot_rot(begin=begin+0.25*ring.nstpp,strobe=ring.nstpp, width=4.0, type="none",
marker='x', color='red')
   plot_rot(begin=begin+0.75*ring.nstpp,strobe=ring.nstpp, width=4.0, xmin=0.0,
type="none", marker='o', color='blue'); fma()
######################## TOMO: FINAL P L O T S ########################

#pplot(0, [ppxy, ppxxp, ppyyp], "cellarray", lphoto=1)    # Plot at end

###################### C O M P A R E ########################
file1.close()

if (lcompare):
   plot_comp(runs={dot1+old_crun: {'type': "dot"}}, crun=crun, titlet=cf_title,
               begin=begin, strobe=strobe)
```

Bibliography

[1] D. Jeon, et al., Formation and mitigation of halo particles in the Spallation Neutron Source linac. *Phys. Rev. ST Accel. Beams,* vol. 5, 094201 (2002).

[2] Y. Shimosaki and K. Takayama. Halo formation at early stage of injection in high-intensity hadron rings. *Phys. Rev. E,* vol. 68, 036503 (2003).

[3] T. Wangler, et al., Beam halo in proton linac beams, *Proceedings of 2000 Internation Linac Conference*, Monterey, CA, USA, TU202 (2000).

[4] C. Allen and T. Wangler, Beam halo definitions based upon moments of the particle distribution, *Phys. Rev. ST Accel. Beams*, vol. 5, 124202 (2002).

[5] M. Dorf, et al., A spectral method for halo particle definition in intense mismatched beams, *Physics of Plasmas*, vol. 18, 043109 (2011).

[6] P. Nghiem, et al., Beam halo definitions and its consequences, *Procedings of HB2012*, Beijing, China, THO3A04 (2012).

[7] M. Reiser. Theory and Design of Charged Particle Beams. Wiley-VCH, 2nd edition, 2008.

[8] C. K. Allen, et al. Beam-halo measurements in high-current proton beams. *Phys. Rev. Lett.,* 89(21):214802 (2002).

[9] A. V. Fedotov, et al. Halo and Space-charge Issues in the SNS Ring. Proceedings of EPAC 2000, Vienna, Austria, 2000.

[10] R. H. Cohen, et al. Electron-cloud simulation and theory for high-current heavy-ion beams. *Phys. Rev. ST Accel. Beams*, vol. 7, 2004.

[11] R. H. Cohen, et al. Simulating electron cloud effects in heavy-ion beams. *Nuclear Instruments and Methods in Physics Research Section A: Accelerators, Spectrometers, Detectors and Associated Equipment*, vol. 544, pp. 210 – 215, 2005.

[12] C. F. Papadopoulos. Beam halo creation and propagation in the University of Maryland Electron Ring. *Ph.D. Dissertation*, University of Maryland, College Park, 2009.

[13] R. L. Gluckstern. Analytic model for halo formation in high current ion linacs. *Phys. Rev. Lett.*, vol. 73(9), pp.1247-1250 (1994).

[14] T. Wangler, et al. Particle-core model for transverse dynamics of beam halo. *Phys. Rev. ST Accel. Beams*, 1(8):084201 (1998).

[15] R. Kishek, et al. Beam Halo from Quadrupole Rotation Errors. *AIP Conf. Proc.*, vol. 693, pp. 89–92 (2003).

[16] T. Shea and P. Cameron. Halo Diagnostics Overview. *AIP Conf. Proc.*, vol. 693, pp. 9-13 (2003).

[17] M. Reiser. Free energy and emittance growth in nonstationary charged particle beams. *Journal of Applied Physics*, AIP, 1991, 70, 1919-1923.

[18] J. Qiang, et al. Space-charge driven emittance growth in a 3d mismatched anisotropic beam. *Phys. Rev. Lett.*, 92(17):174801, Apr. 2004.

[19] M. Ikegami. Particle-core analysis of mismatched beams in a periodic focusing channel. *Phys. Rev. E*, 59(2):2330–2338, 1998.

[20] J. D. Gilpatrick. Wide Dynamic-Range Beam-Profile Instrumentation for a Beam-Halo Measurement: Description and Operation. Beam-Halo Dynamics, Diagnostics, and Collimation, vol. 693, pp. 122-125, 2003.

[21] H. Jiang, et al. Study of the low energy proton beam halo experiment. Procedings of NaPAC13, Pasadena, CA. pp. TUODB1, 2013.

[22] R.A. Kishek, et al. The University of Maryland Electron Ring Program, Nuclear Instruments and Methods in Physics Research Section A: Accelerators, Spectrometers, Detectors and Associated Equipment, vol. 733, 1 January 2014, pp. 233-237,

[23] UMER Beam Parameters, UMER report, 2010, also see http://www.umer.umd.edu

[24] B. Beaudoin, et al., Space-charge effects in bunched and debunched beams, *Proceedings of PAC2011*, New York, NY, USA, MOODS1(2011)

[25] See http://www.ptgrey.com/

[26] D. Stratakis, et al. Generalized Phase-Space Tomography for Intense Beams. *Physics of Plasmas*, vol. 17, pp. 056701 (2010).

[27] D. Stratakis. Tomographic measurement of the phase space distribution of a space-charge-dominated beam. *Ph. D. dissertation*. University of Maryland, 2008.

[28] H. D. Zhang. Development of an adaptive masking method to image beam halo. *M.S. thesis*. University of Maryland, 2011.

[29] R. Fiorito, et al., Beam halo imaging using an adaptive optical mask. *Proceedings of BIW10*, Santa Fe, NM, USA, WECNB03 (2010).

[30] H. Zhang, et al., Beam halo measurements at UMER and the JLab FEL using an adaptive masking method, *Procedings of PAC11*, New York, NY, USA, WEOCN5 (2011).

[31] R. Fiorito, et al., Optical synchrotron radiation beam imaging with a digital mask, *Proceedings of BIW2012*, Newport News, VA, USA, TUPG031 (2012).

[32] H. Zhang, et al., Injected beam imaging at SPEAR3 with a digital optical mask, Proceedings of IPAC2012, New Orleans, LA, USA, WEOAA01 (2012).

[33] H. Zhang, et al., Beam halo imaging with a digital optical mask, *Phys. Rev. ST Accel. Beams*, vol. 15, 072803 (2012)

[34] K. Crandall and D. Rusthoi, TRACE 3-D Documentation, Third Edition, LA-UR-97-886, pp 106 (1997).

[35] D.P. Grote, et al. New developments in WARP: Progress toward end-to-end simulation1, *Nucl. Instr. and Meth.* A, vol. 415 pp. 428 (1998).

[36] R.A. Kishek, et al., Simulations and experiments with space–chargedominated beams, *Physics of Plasmas* vol. 10, pp. 2016 (2003).

[37] R. Kishek, et al., Beam dynamics simulations of the University of Maryland Electron-Ring Project, *Nucl. Instrum. and Methods Phys. Res. A*, vol. 415, pp. 417 (1998).

[38] B. Beaudoin, et al., Longitudinal confinement and matching of an intense electron beam, *Phys. Plasmas*, vol. 18, 013104 (2011)

[39] UMER technical note 20130107.

[40] H. Li. Control and Transport of Intense Electron Beams, *Ph.D. Dissertation*, University of Maryland, 2004.

[41] UMER technical note 2010-0204-RAK

[42] Private conversation with T. Wangler

[43] G. Franchetti, et al., Anisotropic free-energy limit of halos in high-intensity accelerators, *Phys. Rev. Lett.*, vol. 88 (25), 254802 (2002).

[44] PIMAX camera, manufactured by Princeton Instrument.

[45] S. Benson, et.al., The 4th Generation Light Source at Jefferson Lab, *Nucl. Instrum. Methods A*, vol. 582, pp.14-17 (2007).

[46] https://dmtpc.mit.edu/twiki/bin/view/Projects/DarkLight

[47] SLAC-PUB-11757

[48] J. Corbett, et al., Visible light diagnostics at SPEAR3, AIP Conference Proceedings 1234, 637 (2010).

[49] H. Weidemann, et al., The 3 GeV synchrotron injector for SPEAR, Proceedings of PAC91. San Francisci, CA, USA, vol. 5, pp. 2688 (1991).

[50] K.J. Ruisard, et al., Design of an electrostatic extraction section for the University of Maryland Electron Ring, *Proceedings of the 2012 International Particle Accelerator Conference*, New Orleans, LA, USA, WEPPR014 (2012).

[51] William Stem, et al., Recovering measured dynamics from a DC circulating space-charge-dominated Storage Ring, *Proceedings of the 2012 International Particle Accelerator Conference*, New Orleans, LA, USA, WEPPR014 (2012).